

# Vector-Boson Fusion and Vector-Boson Scattering

Michael Rauch

*Institute for Theoretical Physics,  
Karlsruhe Institute of Technology (KIT), Germany*

## Abstract

Vector-boson fusion and vector-boson scattering are an important class of processes for the Large Hadron Collider at CERN. It is characterized by two high-energetic jets in the forward regions of the detector and reduced jet activity in the central region. The higher center-of-mass energy during the current and subsequent runs strongly boosts the sensitivity in these processes and allows to test the predictions of the Standard Model to a high precision.

In this review, we first present the main phenomenological features of vector-boson fusion and scattering processes. Then we discuss the effects of higher-order corrections, which are available at NLO QCD for all processes and up to N3LO QCD and NLO electro-weak for VBF-H production. An additional refinement is the addition of parton-shower effects, where recently a lot of progress has been made. The appearance of triple and quartic gauge vertices in the production processes enables us to probe anomalous gauge couplings. We introduce and compare the different parametrizations used in the literature and also discuss the issue of unitarity violation and common unitarization procedures. Finally, we give a short overview of current and possible future experimental searches.

## CONTENTS

I. Introduction	3
II. Characteristics of VBF Processes	4
A. Triboson and QCD-induced Production	10
B. QCD-induced–VBF Interference	11
III. Higher-order Corrections	14
A. NLO QCD Corrections	14
1. Initial-state Collinear Divergences	20
2. Phenomenological Impact	22
B. NLO Electroweak Corrections	28
C. QCD Corrections beyond NLO	30
IV. Parton Shower Effects	33
A. Parton Shower Overview	33
1. Parton Shower with Born Matrix Elements	33
2. Combining Parton Shower and NLO Calculations	35
B. Applying Parton Showers to LO VBF Processes	38
C. Parton Showers Matched to NLO VBF Processes	40
1. The POWHEG-BOX Approach	40
2. Shower Uncertainties	44
V. Anomalous Coupling Effects	48
A. Effective Field Theories	49
1. Non-linear Realization	55
2. Relations between Definitions	57
B. Unitarity	62
1. Unitarity Bounds	62
2. Unitarity Restoration	65
C. Cross Section Results	74
VI. Experimental Status	76
A. LHC Run-I Results	76
B. Future Prospects	79
VII. Summary	79
Acknowledgments	80
References	80

## I. INTRODUCTION

With the start of the Large Hadron Collider (LHC) at CERN, a new era in particle physics has opened. Its run-I phase with center-of-mass energies of 7 and 8 TeV has led to the discovery of the Higgs boson with a mass of 125 GeV [1, 2]. With this measurement, all particles predicted by the Standard Model (SM) have been observed and its parameters determined. In 2015, run II has started with an increased center-of-mass energy of 13 TeV. This and subsequent runs, approved for two further decades including a high-luminosity upgrade, will allow to test the predictions of the SM to high precision. With a projected final integrated luminosity of  $3 \text{ ab}^{-1}$ , its great success will be further strengthened, or deviations can lead us to a new theory of beyond-the-Standard-Model physics.

A class of processes which strongly benefits from the higher center-of-mass energy of the LHC is vector-boson fusion (VBF) and vector-boson scattering (VBS), which we will discuss in this report. In these processes, a quark or anti-quark scatters with another quark or anti-quark via a space-like exchange of an electroweak gauge boson, namely a  $W$  or  $Z$  boson or a photon. Off this  $t$ -channel exchange, a single Higgs or electroweak gauge boson can be emitted, which are VBF processes in the stricter sense. The emission of two electroweak bosons defines the VBS process class. For most of this article, the distinction between vector-boson fusion and scattering is not necessary, and so we will in general use the label VBF to refer to both and mark explicitly when this is not the case. Also, we will mainly focus on VBF production of electroweak gauge bosons. For VBF-Higgs production, we refer the reader to the yellow reports of the LHC Higgs cross section working group [3–6] for an overview of the current theoretical status.

This electroweak  $t$ -channel exchange is the defining feature of VBF processes, which we will first discuss in section II. Restricting ourselves to the leading-order (LO) Born approximation, important distributions for VBF processes are then presented. This includes a very characteristic feature, the two final-state (anti-)quarks which appear as jets in the forward regions of the detector. These also allow us to distinguish VBF processes from other production modes with the same final state. Possible backgrounds are on the one hand triboson production, where as in VBF no strong coupling constant enters at LO. There, the two jets originate from the decay of a gauge boson, i.e. instead of  $t$ -channel exchange an  $s$ -channel resonance occurs. On the other hand, the two quark lines can be connected by a gluon, giving rise to QCD-induced  $V(V)jj$  production. The appearance of two powers of the strong coupling constant and additional partonic subprocesses with two quarks and two gluons means that for total cross sections, QCD-induced production will dominate. We will discuss how to suppress these alternative production modes compared to VBF and also possible interference contributions in section II B.

In order to obtain precise predictions, the inclusion of higher-order corrections is necessary. Contributions at next-to-leading order (NLO) in the strong coupling constant (NLO QCD) are known for all VBF processes and have been studied in detail. In section III, we will first discuss the QCD corrections to the  $qqV$  vertex, as these are both ultraviolet and infrared divergent. Explicit expressions are derived, employing the Catani-Seymour subtraction scheme [7]. A discussion on the phenomenological impact of these corrections is given in section III A 2. Further higher-order corrections for VBF processes have been calculated so far only for VBF-Higgs production. There, both NLO electroweak and next-to-next-to-leading order (NNLO) QCD corrections are available for differential distributions, and even next-to-next-to-next-to-leading order (N3LO) QCD for inclusive cross sections. Their

impact is discussed in sections III B and III C, respectively.

A further possible refinement on the description of VBF processes is the inclusion of parton-shower effects. In section IV, first a short general introduction is given to present the main features of parton showers and the relevant formulae. Subsequently, we apply parton showers to VBF processes. Phenomenological results for the combination with LO cross sections are presented in section IV B. Great progress has been made in recent years for matching NLO QCD calculations and parton showers. A popular choice for VBF processes has been to use the POWHEG-BOX program [8–10]. Results obtained within this framework are discussed in section IV C 1. In parton showers, a further scale appears, the starting scale of the parton shower. This allows one to obtain error estimates on higher-order effects by varying this scale, similar to changing the factorization and renormalization scales in an NLO calculation. The impact of varying all three scales is shown in section IV C 2. There, we also discuss the agreement between the two popular matching schemes, POWHEG-type [8, 9] and MC@NLO-type [11]. These are equivalent to the accuracy required for combining with NLO QCD calculations, but differ in higher-order terms.

The appearance of triple and quartic gauge couplings in VBF processes makes them an ideal tool to study anomalous contributions to these vertices. A convenient parametrization of the effects, based on Lorentz and gauge invariance, are effective field theories. Two approaches exist, which differ in the expansion parameter and the power counting of the operators. One is based on the canonical dimension of the operators, the other on their chiral dimension. In section V, we introduce the two methods and denote the operators relevant for anomalous gauge couplings and relations between different parametrizations. The high-energy behavior of VBS processes is dominated by a delicate cancellation between different Feynman diagrams. Considering the equivalent  $2 \rightarrow 2$  process, individual Feynman diagrams for scattering of longitudinal gauge bosons show a leading behavior of  $E^4$ , where  $E$  denotes the center-of-mass energy of the process. Exact cancellations due to the gauge structure of the SM then guarantee that the total amplitude exhibits as leading term a constant dependence on energy. Anomalous couplings spoil this cancellation, and the corresponding rise of the amplitude with energy eventually leads to a violation of unitarity of the  $S$  matrix. In section V B, we first derive the (tree-level) unitarity bound through a partial-wave analysis. Then we present different methods to circumvent this bound and obtain a unitarity-conserving amplitude for all energies accessible at the LHC. Methods discussed are the application of form factors, or using the  $K$ -matrix method [12, 13], an inverse stereographic projection onto the unitarity circle. Finally, we show the impact of anomalous couplings and unitarization methods on differential cross sections in section V C.

Lastly, section VI presents an overview of the experimental status on VBF processes. We show the status of current measurements and observations obtained from run-I of the LHC, and discuss the prospects for subsequent runs.

## II. CHARACTERISTICS OF VBF PROCESSES

Typical Feynman diagrams contributing to VBF are depicted in Fig. 1. We will mostly use same-sign  $W$  pair production via VBF,

$$pp \rightarrow W^+W^+jj \rightarrow e^+\nu_e\mu^+\nu_\mu jj + X \quad (\text{“VBF-}W^+W^+”), \quad (1)$$

as an example in this chapter, pointing out differences or additional contributions appearing in other processes when necessary.

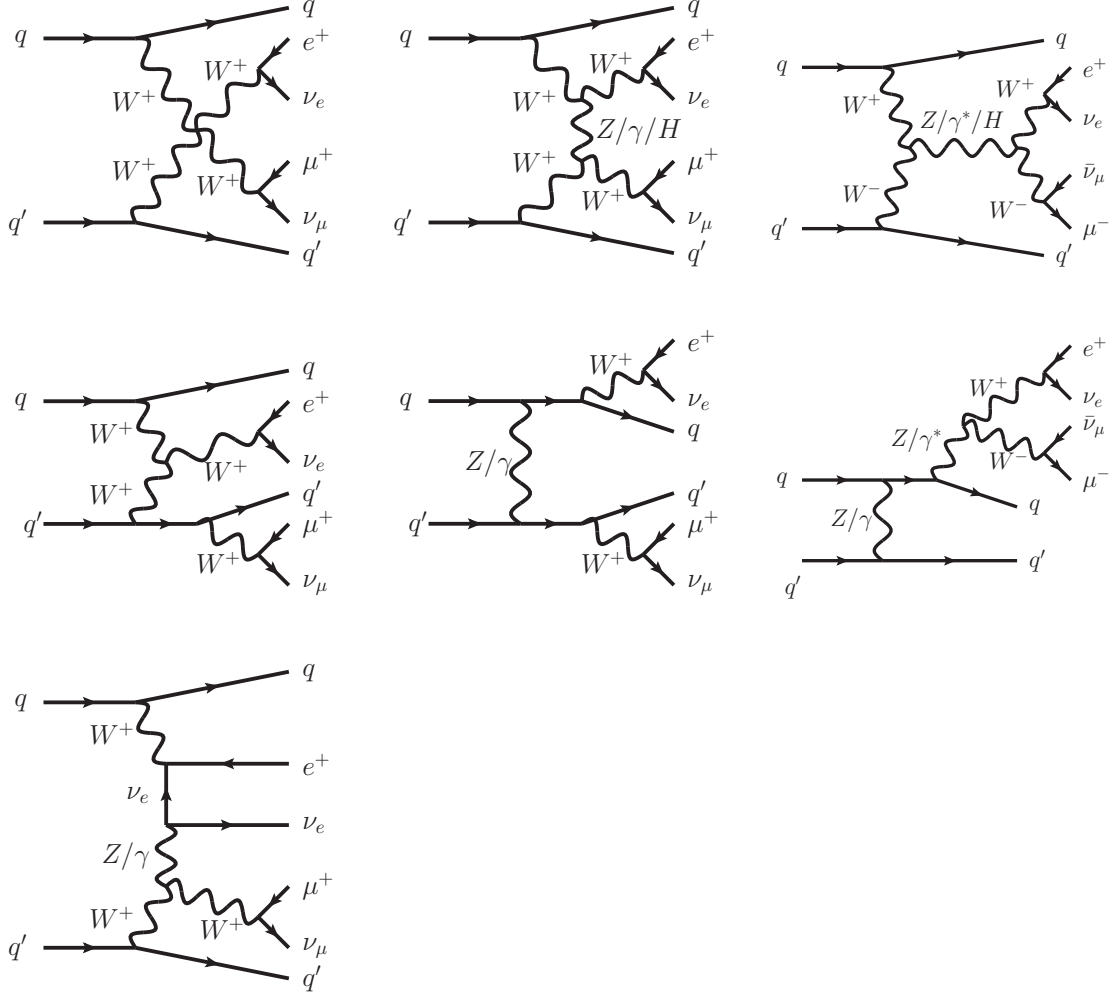


FIG. 1. Typical Feynman diagrams appearing in VBF production. Diagrams in the left and center columns are for the process  $pp \rightarrow e^+ \nu_e \mu^+ \nu_\mu jj$  (“VBF- $W^+W^+jj$ ”), while the right column shows additional contributions appearing for  $pp \rightarrow e^+ \nu_e \mu^- \bar{\nu}_\mu jj$  (“VBF- $W^+W^-jj$ ”). The upper row contains the signature diagrams giving rise to the name of the process class, while in the middle row there are additional diagrams needed to form a gauge-invariant set. The lower row shows an example for a non-resonant contribution.

The Feynman diagrams shown in the upper row of Fig. 1 are responsible for the name of this process class. Looking only at the inner part, the two virtual  $W$  bosons emitted off the quark or anti-quark lines and the two final-state  $W$  bosons describe a  $2 \rightarrow 2$  scattering process. The two incoming bosons are, however, space-like ( $q^2 < 0$ ) and not on-shell as in a real scattering process. The interaction part can either be direct via a quartic gauge coupling (upper left diagram), or via exchange of a space-like boson (upper center). In our example this could be a photon,  $Z$  boson or a Higgs boson. For other final states, also  $s$ -channel diagrams can appear (upper right).

To end up with a gauge-invariant set of Feynman diagrams, we need to add some other contributions as well which are shown in the middle row of Fig. 1. The final state  $W^+$  bosons can also be emitted directly off the quark lines, either only one of them (middle left)

or both (middle center). Also diagrams with one boson radiated off a quark line and then splitting into the two final-state quarks via a triple gauge coupling (middle right) can appear for other processes.

In general we will consider not only on-shell production of the final-state bosons, but also include their decays, as already alluded to by the process definition eq. (1). The vector bosons can either decay into a pair of leptons or a pair of quarks. The latter mode is usually called hadronic decays, as the particles observed in the detector are hadrons. In case of two final-state vector bosons, the nomenclature is as follows:

- leptonic: both vector bosons decaying into leptons,
- hadronic: both vector bosons decaying into quarks,
- semi-leptonic: one vector boson decaying into leptons, the other into quarks.

When considering leptons or quarks as final states, additional non-resonant diagrams appear. An example is depicted in the lower row of Fig. 1. The additional contribution of such diagrams is typically rather small, of the order of a few percent at maximum, as these diagrams lack at least one resonant contribution and carry a suppression factor of order  $\Gamma/M$ . Exceptions can however occur where phase-space cuts force one of the bosons off-shell. The same is true for the contribution of virtual photons, which appear in the diagrams instead of a  $Z$  boson.

The experimental tell-tale to distinguish this process class from QCD-induced production mechanisms and others are, however, the two quarks in the final state, which appear as hadronic jets in the detector, called tagging jets. On a historic side note, very early papers [14–17], targeted for the SSC, a planned but never finished proton-proton collider in the US with a target center-of-mass energy of 40 TeV, considered to not resolve these. Instead, one would define the gauge bosons as additional partons, similar to the recent inclusion of photons in parton distribution functions (PDFs), and compute a  $2 \rightarrow 2$  scattering process with on-shell incoming gauge bosons. Only later was it realized that an explicit inclusion of the tagging jets is needed [18–20].

The tagging jets are typically in the forward regions of the detector. One can see this from the following argument [21, 22]. Let us for simplicity take VBF-Higgs production, and assume a flavor combination of the external quarks that allows only for  $W$  exchange,  $q_1(p_1)q_2(p_2) \rightarrow q_3(p_3)q_4(p_4)H(p_5)$ . Then a short analytic calculation shows that the squared matrix element is proportional to [14, 23–26]

$$|\mathcal{M}_{fi}|^2 \propto \frac{p_1 \cdot p_2 p_3 \cdot p_4}{(q_1^2 - M_W^2)^2 (q_2^2 - M_W^2)^2}, \quad (2)$$

where  $q_1 = p_1 - p_3$  and  $q_2 = p_2 - p_4$  denote the momenta of the two virtual  $W$  bosons.

In order to maximize this expression for a fixed partonic center-of-mass energy  $\sqrt{\hat{s}} = \sqrt{2 p_1 \cdot p_2}$ , we have two possibilities. First, we can increase the numerator, i.e. require that  $p_3 \cdot p_4$  is large. This condition means that the invariant mass of the two tagging jets  $m_{jj} = \sqrt{2 p_3 \cdot p_4}$  should be fairly high. Second, we should make the denominator small. As all quarks are taken as massless, we can use

$$q_1^2 = -2 p_1 \cdot p_3 = -2E_1 E_3 (1 - \cos \theta_1) = -\frac{2}{1 + \cos \theta_1} \frac{E_1}{E_3} p_{T,3}^2, \quad (3)$$

where  $\theta_1$  describes the scattering angle between  $\vec{p}_1$  and  $\vec{p}_3$ , and the absolute value of the transverse component of  $\vec{p}_3$  is given by  $p_{T,3} = E_3 \sin \theta_1$ . The upper bound of  $q_1^2$  is at zero, so the inverse  $W$ -boson propagator becomes small for values of  $q_1^2$  close to zero, when the scattering angle becomes small. There, we can rewrite the inverse propagator as  $(q_1^2 - M_W^2) \simeq -(\frac{E_1}{E_3} p_{T,3}^2 + M_W^2)$ .

From this we see that the transverse momentum of the  $W$ , which is equal to the transverse momentum of the final-state quark, should not significantly exceed  $M_W$  in order to not incur an additional suppression factor. At the same time, the quark should have a large momentum component in the  $z$  direction to yield a small scattering angle. The  $W$  boson will typically carry only a fairly small portion of the momentum of the incoming parton, similar to photon radiation from an energetic electron. But it also needs to carry enough energy to produce the final-state Higgs boson, namely around  $\frac{M_H}{2}$ .

Hence, the two tagging jets are expected to have large energies with only moderate transverse momenta, putting them into detector regions with fairly small scattering angle or large pseudorapidity.

Several normalized differential distributions illustrating these features at leading order (LO) are shown in Fig. 2. This and the following figure have been generated with VBFNLO [27–29]. As processes, we use both VBF- $W^+W^+jj$  and VBF- $Hjj$  production. For the latter no cuts are applied on the final-state jets. This still gives a finite and well-defined cross section, as no singular regions appear for example when the jet transverse momentum approaches zero. To VBF- $W^+W^+jj$  production we instead apply standard jet cuts, namely  $p_{T,j} > 30$  GeV,  $|y_j| < 4.5$  and  $R_{jj} > 0.4$ .

In the upper left panel we plot the transverse momentum of the leading jet, i.e. the jet with the largest transverse momentum, and the transverse momentum of the second jet on the right. Consistent with our discussion before, both distributions peak at fairly small values of the transverse momentum. For  $Hjj$  the value is smaller and extends less to larger values, as less energy is required to produce the Higgs boson. Also in the Higgs case the exchange is dominated by longitudinal gauge bosons, while they are mostly transverse for same-sign  $W$  production. The different polarizations lead to a relative factor of  $\frac{p_T^2}{M^2}$  for transverse over longitudinal, thus processes with transverse polarizations prefer larger transverse momenta. The jet  $p_T$  of  $W^+W^+jj$  averaged over both jets however also exhibits a maximum at only 80 GeV, which corresponds to our previous estimate. In the middle left panel, where the rapidity of the leading jet is plotted, we see that central jets around  $y = 0$  are suppressed compared to forward jets, with the maximum around  $|y| = 2$ . Consequently, there is a fairly large rapidity gap between the two jets of about 4 on average. The jet cuts impose an upper limit of  $\Delta y_{jj} < 9$  for VBF- $W^+W^+jj$  production. The invariant mass of the two jets is plotted in the lower right panel. Again, this distribution extends to fairly large values as expected, with  $W^+W^+jj$  production generating more energetic events. Finally, the correlation plot between the invariant mass and the rapidity difference of the two jets for  $W^+W^+jj$  is shown on the bottom left of Fig. 2. These are the two variables which are typically used for cuts to enhance the VBF contribution over other processes. The correlation between the two variables can also be seen from the analytic formula

$$m_{jj}^2 \simeq 2p_{T,j_1}p_{T,j_2} (\cosh(\Delta y_{jj}) - \cos(\Delta\phi_{jj})) , \quad (4)$$

where  $\Delta\phi_{jj}$  denotes the azimuthal angle difference between the two jets. The formula becomes exact if the two jets are massless, which is the case for our LO discussion here.

A crucial question for experimental analyses is whether this central rapidity gap with

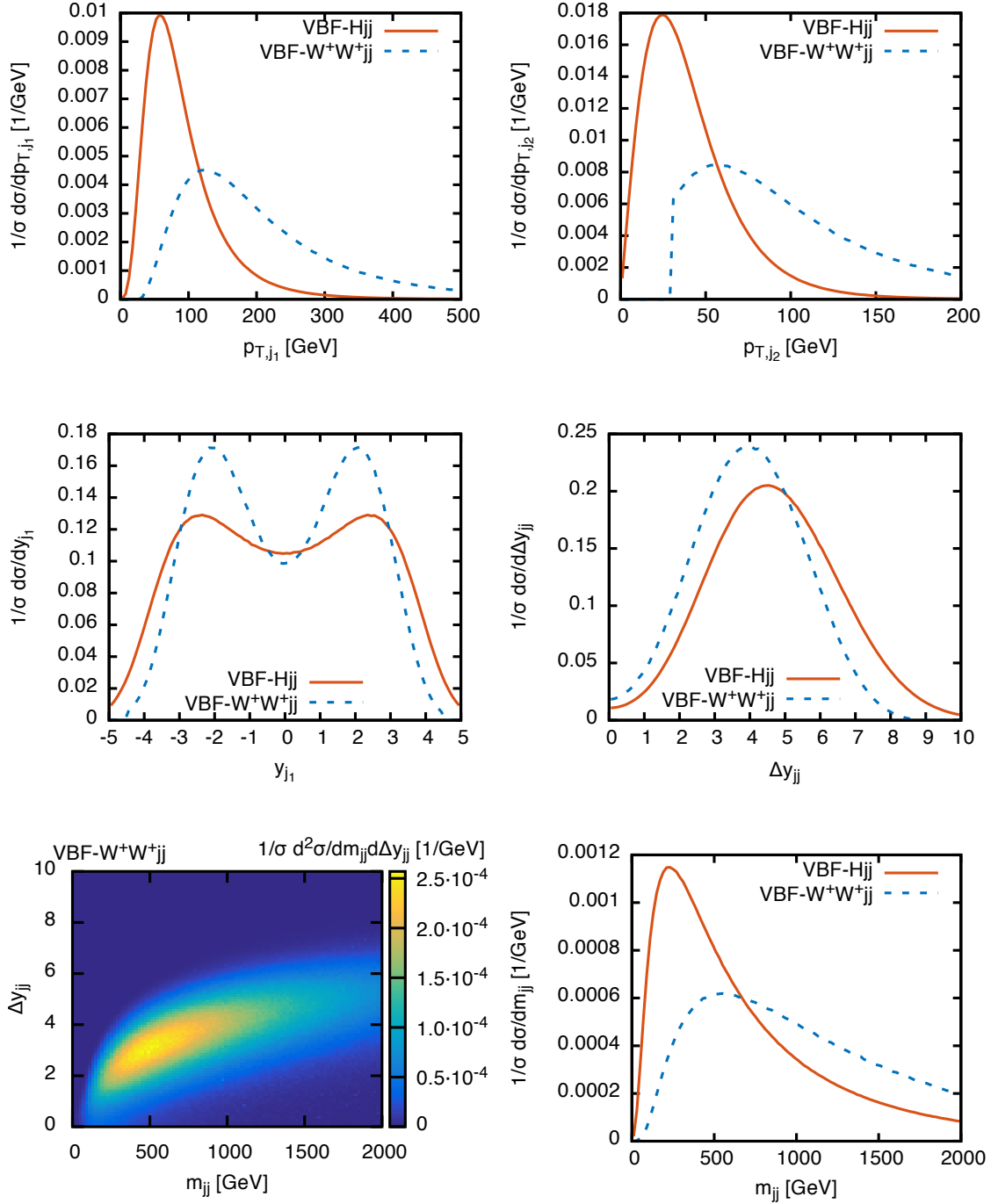


FIG. 2. Normalized LO differential distributions for VBF production of  $Hjj$  (solid red) and  $W^+W^+jj$  (dashed blue and bottom left) for the LHC at 13 TeV center-of-mass energy. Distributions presented are the transverse momentum of the leading and the second jet (top row), the rapidity of the leading jet (middle left), and the rapidity difference (middle right) and invariant mass (bottom right) of the two jets. The bottom left panel shows the correlation plot between invariant mass and rapidity difference of the two jets for  $VBF-W^+W^+jj$ .



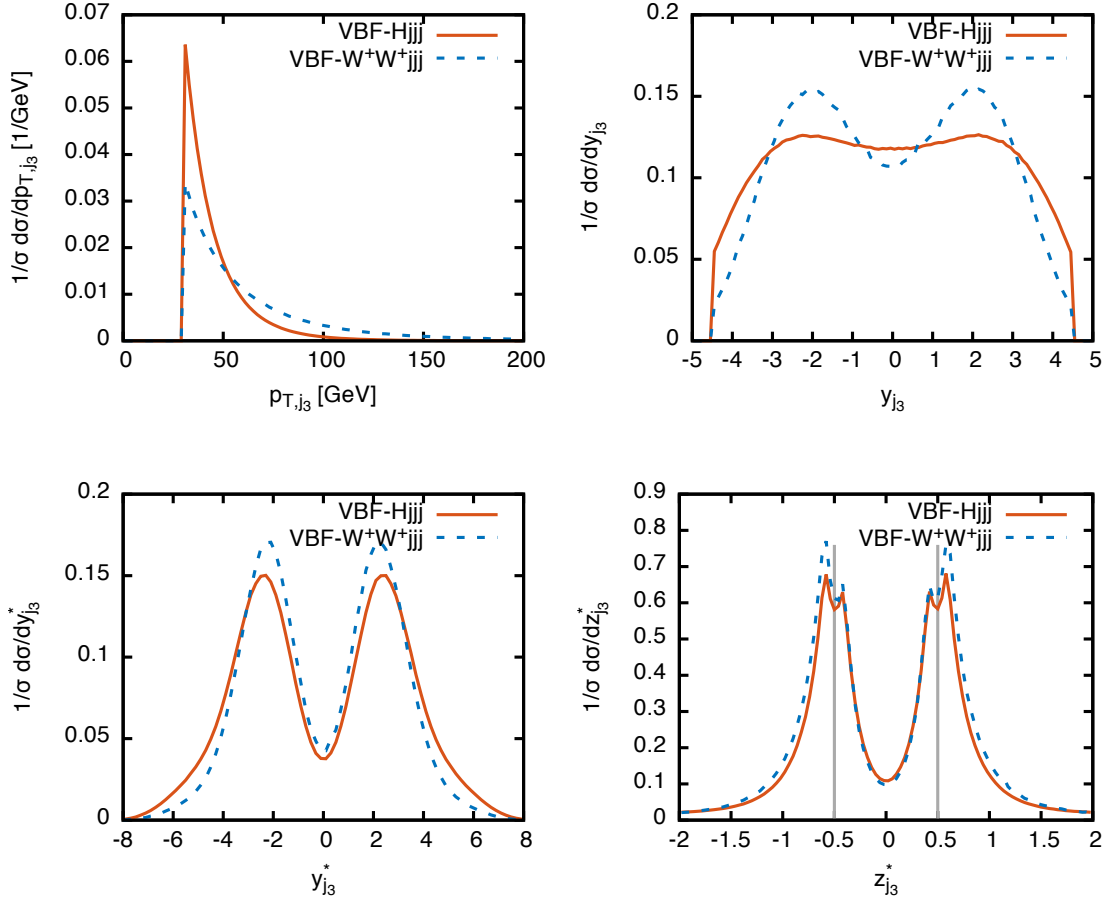


FIG. 3. Normalized differential distributions for VBF production plus extra jet of  $Hjjj$  (*solid red*) and  $W^+W^+jjj$  (*dashed blue*) for the LHC at 13 TeV center-of-mass energy. Distributions show the transverse momentum (*upper left*) and the rapidity of the third jet (*upper right*). In the lower panel the third-jet rapidity relative to the averaged rapidity of the two tagging jets (*lower left*) and additionally normalized to the position of the two tagging jets (*lower right*) is plotted.

reduced jet activity is only an artifact of performing a LO calculation, or stable also when adding extra jet radiation. For a first discussion of this issue, we show results for the two processes with an extra jet emission, i.e. electroweak  $Hjjj$  and  $W^+W^+jjj$  production. In terms of Feynman diagrams, we need to attach a gluon to the quark lines at all possible positions, keeping in mind that the interference of two diagrams, where the gluon is attached to different quark lines, vanishes due to the color structure. Additionally, processes with the gluon crossed into the initial state need to be taken into account. As these processes are no longer finite without jet cuts, we impose the aforementioned cuts now also to  $Hjjj$  production. In the upper left panel of Fig. 3, first the transverse momentum of the third jet, ordered by decreasing transverse momentum, is plotted. The extra jet is preferably close to the minimal cut value of 30 GeV. The upper right panel shows the rapidity of the third jet, ordered by decreasing transverse momentum. A dip in the central region is also visible for this distribution, similar in shape to the one for the two leading jets. There, we have seen that the difference in rapidity exhibits an even stronger dip at zero than the rapidities

themselves. Similarly, one can define a variable  $y^*$ , which gives the rapidity of the  $n$ -th jet relative to the two tagging jets [30],

$$y_{j_n}^* = y_{j_n} - \frac{y_{j_1} + y_{j_2}}{2}. \quad (5)$$

This is shown in the lower left panel of Fig. 3, which indeed exhibits a pronounced dip at zero. As we have seen in Fig. 2, the rapidities of the tagging jets have a maximum at about  $\pm 2.5$ , which is also the maximum for the  $y_{j_3}^*$  distribution. Hence, one can already conclude that the extra jet emission is preferably close to the position of one of the tagging jets. Alternatively, via an additional scaling factor one can make this even more obvious and fix the position of the two tagging jets by defining [31]

$$z_{j_n}^* = \frac{y_{j_n}^*}{|y_{j_1} - y_{j_2}|}, \quad (6)$$

where the two tagging jets are located at  $z^* = \pm \frac{1}{2}$ . This divides the phase space in the central rapidity gap,  $|z^*| < \frac{1}{2}$ , and the region between tagging jets and beam axis,  $|z^*| > \frac{1}{2}$ . This distribution, plotted in the lower right panel of Fig. 3, indeed has maxima around  $\pm 0.5$ . The small dip at exactly  $\pm 0.5$  is due to the jet separation cut  $R_{jj}$ , which removes events where the two jets are very close together.

### A. Triboson and QCD-induced Production

Looking at the process definition of VBF processes like eq. (1), one realizes that there are other possibilities to produce the same final state. One such option is crossing the quark lines between initial and final state such that the two incoming quarks are connected, and hence also the two outgoing ones. An example Feynman diagram is shown in Fig. 4 on the top left. The final-state quark–anti-quark pair originates from a gauge boson, so this process class can be seen as triboson production with one hadronic and two leptonic decays of the three bosons. From the diagram we can already guess that the characteristics of the jets will be quite different from those of VBF processes. The invariant mass of the two jets is expected to follow a Breit-Wigner distribution centered around the mass of the corresponding gauge boson and with its width, hence at much smaller values than in VBF processes. Also the rapidity distribution of the two jets should be much more central.

Another possibility is QCD-induced  $VV$  production in association with two jets [32–46]. In these processes a gluon instead of a vector boson gets exchanged between the two quark lines. Hence, the coupling order of the process has two powers of the strong coupling constant  $\alpha_s$ , and two orders of the electromagnetic coupling  $\alpha$  less than the corresponding VBF process, i.e.  $\mathcal{O}(\alpha_s^2 \alpha^4)$  instead of  $\mathcal{O}(\alpha^6)$ . The two diagrams on the right-hand side of Fig. 4 are examples for this process class. Except for same-sign  $W$  production, partonic subprocesses with two quarks and two gluons as external colored particles exist as well, shown on the bottom left of the figure. The exchange of a colored particle between the two quark lines again leads to a markedly different phase-space distribution of the jets. The jets are going to be much more central than for VBF processes.

Interference between these processes and the VBF one needs also to be taken into account. For partonic subprocesses where the external quark content is the same, this will in general be non-zero. The important question is, however, if these effects are large or possibly small enough to be neglected.

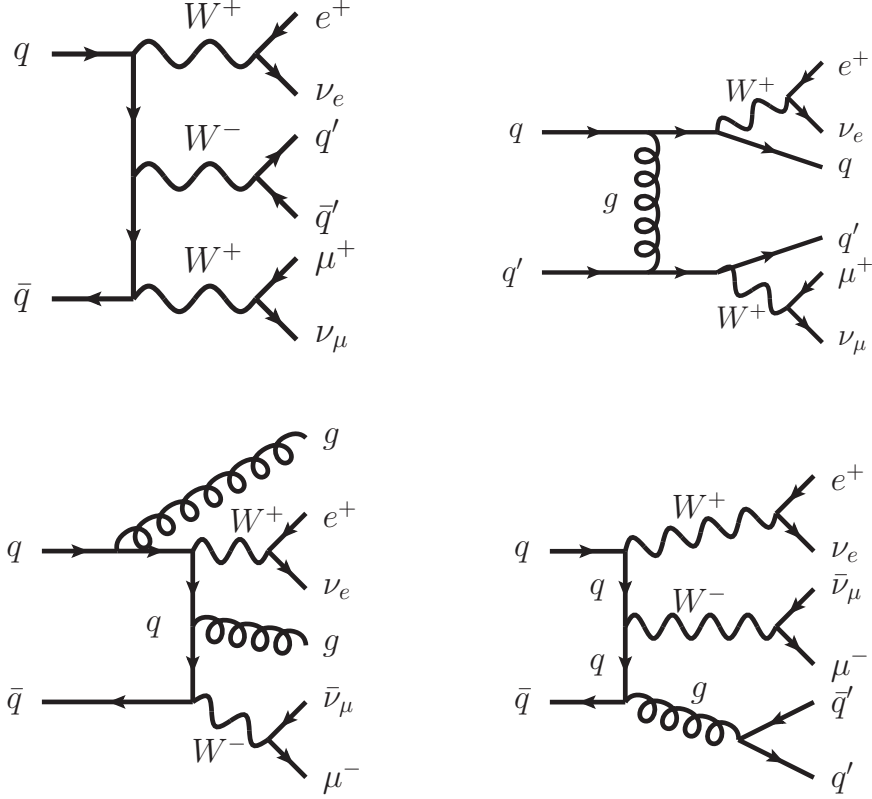


FIG. 4. Feynman diagrams of other processes contributing to the same final state as the VBF process. *Top left*: triboson production, *top right* and *bottom*: QCD-induced  $VVjj$  production.

## B. QCD-induced–VBF Interference

Let us first consider interference between the QCD-induced and VBF process, when the flavor of the two quark lines is different (upper row of Fig. 5). The color part of a quark-gluon vertex is  $T_{ij}^a$ , where  $T$  are the generators of  $SU(3)$ , and propagators are simply  $\delta$ -functions of the attached color charges. Hence, at the upper quark-gluon vertex we find  $T_{ii}^a = \text{Tr}[T^a] = 0$ . We can also argue in the following way: The color exchange between the two quark lines in VBF is always a color singlet. Hence, to have a non-vanishing interference, the exchange on the right-hand side must be a color singlet as well. The gluon is however a pure color octet, and so this contribution actually vanishes exactly. In case of identical quark flavors another diagram appears, where the quark lines are flipped (middle row). In this case we obtain for the color trace of the color-averaged matrix element squared  $\frac{1}{N^2} T_{ij}^a T_{ji}^a = \frac{N^2-1}{2N^2} = \frac{4}{9}$ , i.e. a finite contribution. The phase-space characteristics of the final-state jets is still quite different for the two processes. The preference for forward jets in VBF would mean for the interference to be maximal that the jets from the QCD-induced part should mostly go in the backward region, which is not the case.

Interference between VBF and triboson processes (lower row) can only happen for quark–anti-quark initial states. The color factor is  $\frac{1}{N} = \frac{1}{3}$  for this interference term, compared to 1 for the VBF color-averaged squared matrix element. The main reason that this interference term is also suppressed is the different behavior of the two-jet invariant mass. The triboson

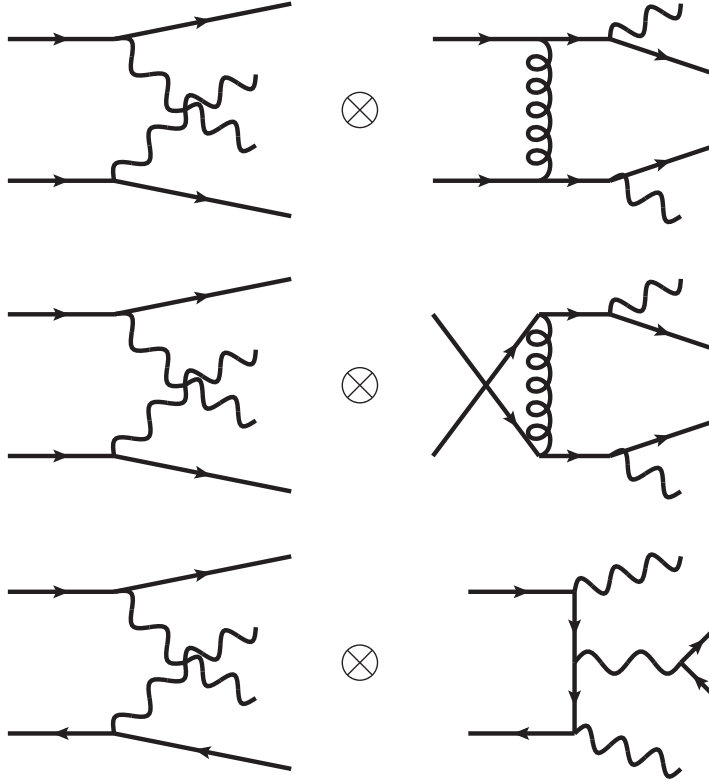


FIG. 5. Interference contributions between the VBF process and QCD-induced  $VV$  production for different quark flavors (*first row*), additional contribution for same quark flavors (*middle row*), and interference with triboson production (*lower row*). The decays of the vector bosons have been left out for clarity.

part is strongly peaked at the mass of the vector boson where the two jets originate from, while the VBF part again prefers much larger values.

A more quantitative picture is presented in Fig. 6, taken from Ref. [39]. There we plot, at leading order (LO) for the LHC running at 14 TeV center-of-mass energy, the size of the different contributions for four important differential distributions, namely the transverse momenta of the two tagging jets, the invariant mass of them, and their separation in rapidity. In the smaller panels below each distribution the relative contribution compared to the full LO result is shown. The individual curves in the plots denote the following contributions: the one labeled “QCD” contains the QCD-induced contribution of order  $\mathcal{O}(\alpha_s^2\alpha^4)$ , “EW” contains all contributions of order  $\mathcal{O}(\alpha^6)$ , i.e. both the VBF part ( $t$ - and  $u$ -channel) and the triboson part ( $s$ -channel) and their interferences. “QCD+EW” is the simple sum of these two, while “full” also includes their interference term of order  $\mathcal{O}(\alpha_s\alpha^5)$ , also shown separately as “Int”. Finally, the “VBF” curve shows the VBF contribution only. This part also neglects interference terms between  $t$ - and  $u$ -channel. In Ref. [47] it has been shown that these interference terms are negligible once VBF cuts are applied. This is also expected from a theory point of view, as in addition to a color factor of  $\frac{1}{3}$ , jets which are forward for one part are backward for the other one, and hence leads to a strongly suppression.

As already expected from the discussions above, the VBF contribution is relatively big

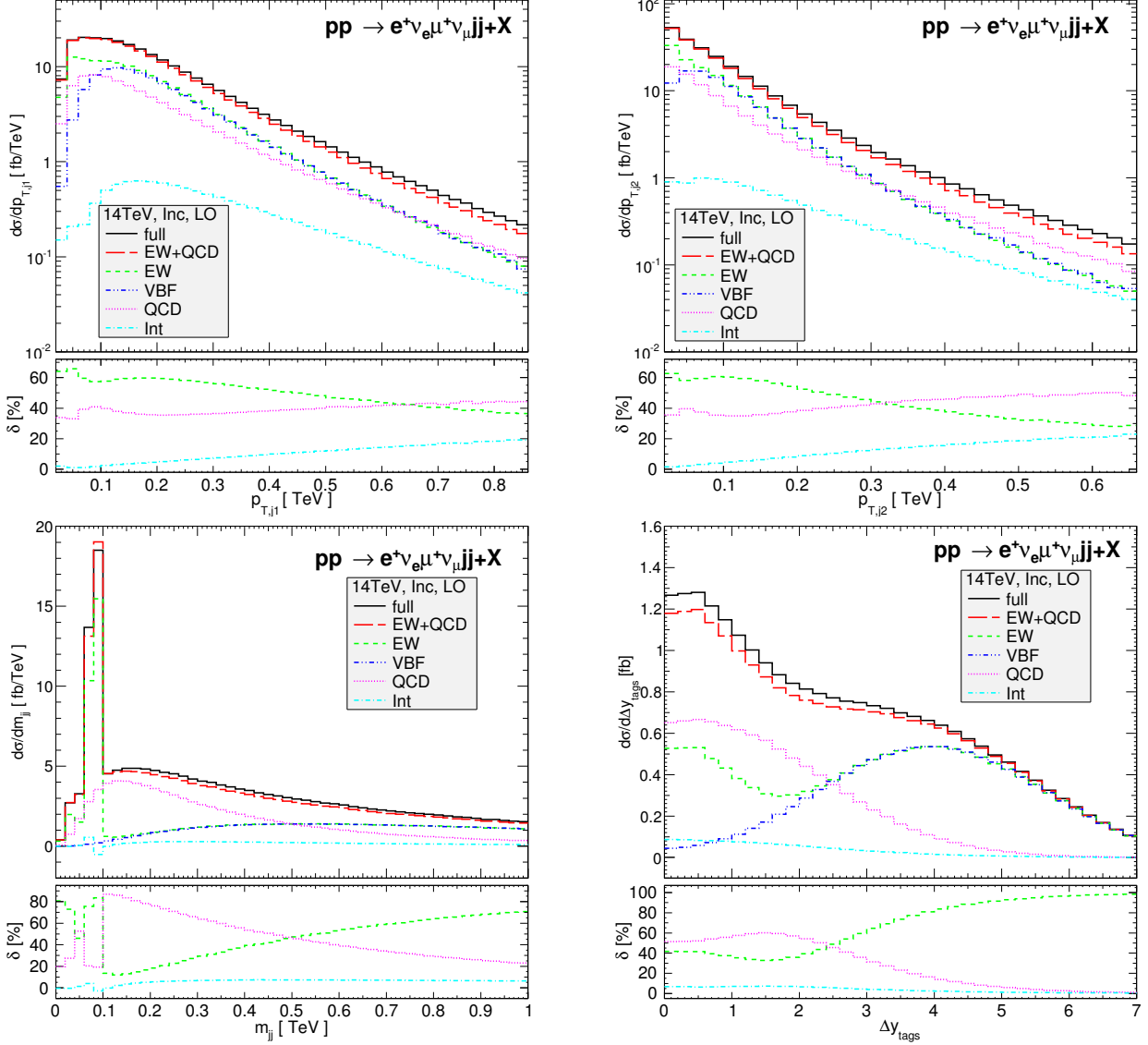


FIG. 6. Differential cross sections with inclusive cuts for the transverse momenta (top row) and the invariant mass (bottom left) of the two tagging jets ordered by  $p_T$ . The distributions of the rapidity separation between the two jets are in the bottom right panel. The relative EW, QCD and interference contributions compared to the full LO results are also plotted in the small panels. Figure taken from Ref. [39].

for large invariant masses of the two tagging jets, reaching up to 70% of the full cross section for an invariant mass of 1 TeV. The difference to the full EW contribution is large only at invariant masses around the  $W$  mass, where the Breit-Wigner peak is clearly visible. For larger invariant masses the effect is negligible. From the plots one can also see that QCD-EW interference effects are biggest when the transverse momenta of the tagging jets are large and the rapidity separation between them is small. The VBF curve on the other hand favors a large rapidity separation, where the interference drops below the 5% level. In Ref. [39]

two sets of VBF cuts have been defined

$$m_{jj} > 200 \text{ GeV}, \quad \Delta y_{jj} > 2.5, \quad (\text{loose}) \quad (7)$$

$$m_{jj} > 500 \text{ GeV}, \quad \Delta y_{jj} > 4, \quad y_{j_1} \cdot y_{j_2} < 0. \quad (\text{tight}) \quad (8)$$

For the loose cut set, the QCD contribution yields an additional 20.3% and the QCD-EW interference 3.3% on top of the VBF cross section of 1.784 fb. Using the tight VBF cuts, this reduces to 4.1% and 1.3%, respectively, with a VBF cross section of 0.971 fb. Additional effects due to EW non-VBF diagrams are at or below 1 per mill in both cases. Therefore, when comparing to experimental measurements, QCD-induced production is a relevant background process which needs to be taken into account, but any interference is small once we impose VBF cuts.

Finally, the question is how we can formally define the VBF contribution and separate them from the other processes with the same final state. For the distinction with the QCD process, we can simply count the order of the coupling constants, which should be  $\mathcal{O}(\alpha_s^0 \alpha^n)$ , where  $n$  is the number of particles in the final state. In our process we have used for most of the chapter, eq. (1),  $n$  would be 6. In order to separate triboson production, we assume that two copies of  $SU(3)_c$  exist, and the quark from the first proton carries the usual color charge from one  $SU(3)_c$ , but is neutral with respect to the other one, and vice versa for the quark from the second proton. Then connecting the two incoming quarks is not possible, as this would violate color charge conservation. Additionally,  $t$ -/ $u$ -channel interference becomes automatically absent. This scheme is also known as the structure-function approach, as the  $qqV$  vertex can be included in charged-current and neutral-current hadronic structure functions [48].

This picture will be particularly useful in the next chapter, where we discuss higher-order corrections, as it gives a clear prescription which terms to include and which are omitted due to the VBF approximation. Also, the sometimes used statement that VBF can be seen as a process of two-sided deep inelastic scattering becomes obvious in this picture.

### III. HIGHER-ORDER CORRECTIONS

In order to get a useful comparison between theoretical predictions and experimental results, the uncertainty of the former, for example due to the truncation of the perturbative series, should at least match the precision of the latter. At the LHC, we can expect a final accuracy of a few percent for VBF processes (see section VI for a more detailed discussion). Using just LO calculations is not sufficient to obtain the same level for predictions on cross sections and distributions.

In this chapter we will discuss the available higher-order corrections and show their impact on integrated cross sections and differential distributions.

#### A. NLO QCD Corrections

Next-to-leading order corrections in the strong coupling constant  $\alpha_s$ , NLO QCD for short, are available for all VBF processes considered here. They have been first calculated in Refs. [47, 49–55].

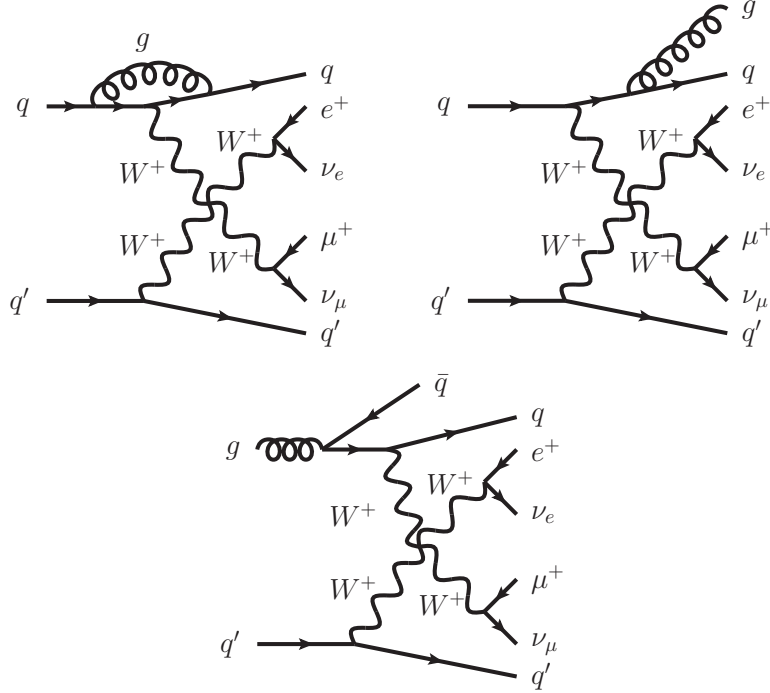


FIG. 7. Typical Feynman diagrams appearing in VBF production at NLO QCD. The diagram on the left-hand side shows a virtual correction to the upper quark line. The other two diagrams are examples for real emission processes, either with final-state gluon radiation (*center*) or gluon-initiated (*right*).

Fig. 7 shows examples of Feynman diagrams contributing. These can either be virtual corrections (left diagram), which contribute via an interference with the Born matrix element, or real-emission diagrams, where an additional gluon is radiated off the quark line (center diagram). Crossing of initial and final state then also leads to contributions where the gluon is in the initial state (right diagram). Diagrams for the lower quark line and where initial and final state of a quark line are exchanged are analogous. For the moment, we will restrict our discussion to the diagrams where no final-state  $W$  is radiated off the quark lines, and come back to these separately later. This corresponds for example to the case of VBF- $H$  production, where only such diagrams are present.

In this case the only virtual contributions are corrections to the  $qqV$  vertex as shown in Fig. 7. For definiteness, let us introduce momenta in the following way:  $q(p_1)q'(p_2) \rightarrow q(p_3)q'(p_4)e^+(k_1)\nu_e(k_2)\mu^+(k_3)\nu_\mu(k_4)$ . Additionally, we define  $q_1 = p_1 - p_3$  and  $q_2 = p_2 - p_4$  as well as  $Q_{1,2}^2 = |-q_{1,2}^2|$ . All quarks are taken as massless. Then the upper fermion line can be written as

$$\mathcal{M}^\mu = \mu^{4-D} \int \frac{d^D \ell}{(2\pi)^D} \bar{u}(p_2) i g_s \gamma^\nu \frac{i}{\not{\ell} + \not{p}_2} i g \gamma^\mu P_L \frac{i}{\not{\ell} + \not{p}_1} i g_s \gamma^\rho u(p_1) \frac{-i g_{\nu\rho}}{\ell^2} T_{jk}^a T_{ki}^a. \quad (9)$$

The last two factors are the SU(3) generators  $T$ . They yield  $T_{jk}^a T_{ki}^a = C_F \delta_{ij} = \frac{4}{3} \delta_{ij}$ , where  $i$  and  $j$  are the color indices of the incoming and outgoing quark, respectively. An explicit calculation, either by hand or using modern tools [56–64] shows that these corrections factorize against the Born matrix element  $\mathcal{M}_B$  and the whole amplitude in dimensional regularization

is given by

$$\begin{aligned} \mathcal{M}_V &= \mathcal{M}_B \frac{\alpha_s}{4\pi} C_F \\ &\cdot \left[ B_0(0) - 2Q_1^2 (C_1(-Q_1^2, 0, 0) + C_2(-Q_1^2, 0, 0)) - 4C_{00}(-Q_1^2, 0, 0) \right] \\ &\stackrel{PV}{=} \mathcal{M}_B \frac{\alpha_s}{4\pi} C_F (4B_0(0) - 3B_0(-Q_1^2) + 2Q_1^2 C_0(-Q_1^2, 0, 0) - 2) . \end{aligned} \quad (10)$$

All mass arguments of the loop functions are zero and have been left out. In the last step, we have converted all loop functions to the basic scalar integrals using the Passarino-Veltman (PV) reduction method [65]. Their explicit form is

$$B_0(0) = \frac{(4\pi)^{\epsilon_{UV}}}{\Gamma(1 - \epsilon_{UV})} \frac{1}{\epsilon_{UV}} - \frac{(4\pi)^{\epsilon_{IR}}}{\Gamma(1 - \epsilon_{IR})} \frac{1}{\epsilon_{IR}} \quad (11)$$

$$B_0(p^2) = \left( \frac{4\pi\mu^2}{-p^2} \right)^{\epsilon_{UV}} \frac{1}{\Gamma(1 - \epsilon_{UV})} \left[ \frac{1}{\epsilon_{UV}} + 2 \right] \quad (12)$$

$$C_0(p^2, 0, 0) = \left( \frac{4\pi\mu^2}{-p^2} \right)^{\epsilon_{IR}} \frac{1}{\Gamma(1 - \epsilon_{IR})} \frac{1}{p^2} \frac{1}{\epsilon_{IR}^2} . \quad (13)$$

For the poles in  $\epsilon$  we have indicated in each loop function whether this originates from the UV region, where the loop momentum  $\ell$  goes to infinity and we need to approach the limit from the positive side, i.e.  $\lim_{\epsilon_{UV} \rightarrow 0^+}$ , or they are from the IR region,  $|\ell| \rightarrow 0$ , with the limit  $\lim_{\epsilon_{IR} \rightarrow 0^-}$ .

The total expression is both UV- and IR-divergent. The UV-divergent part is given by

$$\mathcal{M}_V \Big|_{UV} = \mathcal{M}_B \frac{\alpha_s}{4\pi} C_F \Delta_{UV} \quad (14)$$

with

$$\Delta_{UV} = \frac{(4\pi)^{\epsilon_{UV}}}{\Gamma(1 - \epsilon_{UV})} \frac{1}{\epsilon_{UV}} = \frac{1}{\epsilon_{UV}} - \gamma_E + \ln(4\pi) , \quad (15)$$

which encompasses also some finite terms which are removed together with the pole in the  $\overline{\text{MS}}$  scheme. To get rid of this divergence, we need to perform renormalization on the  $qqW$ -vertex and add the corresponding counter term

$$\mathcal{M}_{CT} = - \left( \frac{Z_g}{\sqrt{Z_q^2 Z_W}} - 1 \right) \mathcal{M}_B \Big|_{\text{NLO}} = - \left( \delta Z_g - \delta Z_q - \frac{\delta Z_W}{2} \right) \mathcal{M}_B . \quad (16)$$

The renormalization constants for the weak coupling  $g$  and the  $W$  field do not receive any QCD contributions at one-loop order,

$$\delta Z_g = \delta Z_W = 0 , \quad (17)$$

while for  $\delta Z_q$  we obtain<sup>1</sup>

$$\delta Z_q = - \frac{\alpha_s}{4\pi} C_F B_0(0) . \quad (18)$$

<sup>1</sup> For an overview on renormalization see e.g. Ref. [66].



Note that this wave function renormalization acts on external particles, so we have to include the full expression despite working in the  $\overline{\text{MS}}$  scheme to guarantee that the residue of the propagator pole is correctly normalized to unity. So the renormalized expression becomes

$$\mathcal{M}_V \Big|_{\text{UV}} + \mathcal{M}_{CT} = \mathcal{M}_B \frac{\alpha_s}{4\pi} C_F \frac{(4\pi)^{\epsilon_{\text{IR}}}}{\Gamma(1 - \epsilon_{\text{IR}})} \frac{1}{\epsilon_{\text{IR}}}, \quad (19)$$

i.e. effectively in eq. (10), all  $\epsilon_{\text{UV}}$  have been replaced by  $\epsilon_{\text{IR}}$ , and we will drop the subscript from now on.

In total we obtain for the Born-Virtual interference [49]

$$\begin{aligned} 2\Re[\mathcal{M}_B^* \mathcal{M}_{V+CT}] &= |\mathcal{M}_B|^2 \frac{\alpha_s(\mu)}{2\pi} C_F \left( \frac{4\pi\mu^2}{Q_1^2} \right)^\epsilon \frac{1}{\Gamma(1 - \epsilon)} \left[ -\frac{2}{\epsilon^2} - \frac{3}{\epsilon} - 8 \right] \\ &= C_\epsilon \frac{\alpha_s}{2\pi} C_F |\mathcal{M}_B|^2 \\ &\quad \cdot \left( -\frac{2}{\epsilon^2} - \frac{3 + 2 \ln \frac{\mu_R^2}{2p_1 \cdot p_3}}{\epsilon} - 8 - 3 \ln \frac{\mu_R^2}{2p_1 \cdot p_3} - \ln^2 \frac{\mu_R^2}{2p_1 \cdot p_3} \right), \end{aligned} \quad (20)$$

with

$$C_\epsilon = \frac{1}{\Gamma(1 - \epsilon)} \left( \frac{4\pi\mu^2}{\mu_R^2} \right)^\epsilon. \quad (21)$$

In the last step the constant  $C_\epsilon$  has been pulled out, as is commonly done in loop calculations [67, 68], and the rest fully expanded in  $\epsilon$ . In dimensional reduction the number in the square bracket would be  $-7$  instead of  $-8$ .

For sufficiently inclusive quantities a theorem by Kinoshita, Lee and Nauenberg [69, 70] states that infrared divergences must cancel. The necessary additional contribution is exactly the real-emission diagrams of Fig. 7. If we look at the center diagram with final-state radiation and denote the momentum of the gluon by  $p_5$ , the propagator of the quark splitting into the final-state quark and the gluon is given by

$$\frac{i(\not{p}_3 + \not{p}_5)}{(p_3 + p_5)^2} = \frac{i(\not{p}_3 + \not{p}_5)}{2p_3 \cdot p_5}, \quad (22)$$

where we have used that both particles are massless. The denominator can be written in any reference frame as

$$2p_3 \cdot p_5 = 2E_3 E_5 (1 - \cos \theta). \quad (23)$$

In the full matrix element, this propagator is attached to the expression  $\bar{u}(p_3) \not{\epsilon}(p_5)$  from the right. So we get effectively another factor of  $\sqrt{E_3}$  from the fermion wave function, while no such term appears for the gluon. This additional factor breaks the apparent symmetry between the two in eq. (22).

There are two important limits here. First,  $p_5$  can go to zero such that the direction stays constant  $p_5 \rightarrow \lambda p_5$ ,  $\lambda \rightarrow 0$ . Then  $E_5 \rightarrow \lambda E_5$ , while the angle  $\theta$  stays constant. This denotes the soft limit. In the collinear limit,  $E_5$  is unchanged, but the two particles become collinear, i.e.  $\theta \rightarrow 0$ , which also leads to a divergence of the propagator. When integrated over the phase space, these lead to corresponding divergences of the cross section, which exactly cancel the corresponding divergences in the virtual amplitudes. For the quark, the

additional factor from the external wave function leads to finite expressions after phase-space integration.

If we want to do a numerical Monte-Carlo implementation of the cross section, we first need to cancel these divergences explicitly so that only finite results appear. This procedure is implemented via a subtraction scheme. Popular choices for NLO QCD are the Frixione-Kunszt-Signer (FKS) [71] or Catani-Seymour (CS) [7] scheme. We will follow the conventions of the latter one here. The idea in all schemes is to subtract a function  $A$  from the real-emission part which shows the same divergent behavior in the singular regions and is small in other regions. To not change the overall result, the same function needs to be subtracted again from the virtual part. If the function can be integrated analytically over the phase space of the extra emission, then this will produce poles in  $\epsilon$  which exactly cancel the ones from the loop integrals. Schematically, this can be written in the following way [7]:

$$\begin{aligned}
\sigma^{\text{NLO}} &= \int_m d\sigma_B + \int_m d\sigma_V + \int_{m+1} d\sigma_R \\
&= \int_m d\sigma_B + \int_m \left( d\sigma_V + \int_1 \sum_{\text{dipoles}} (d\sigma_B \otimes dV_{\text{dipole}}) \right)_{\epsilon=0} \\
&\quad + \int_{m+1} \left( d\sigma_R - \sum_{\text{dipoles}} d\sigma_B \otimes dV_{\text{dipole}} \right)_{\epsilon=0} .
\end{aligned} \tag{24}$$

Thereby,  $\int_m$  denotes the integration over the  $m$ -particle phase space,  $d\sigma_B$ ,  $d\sigma_V$  and  $d\sigma_R$  are the differential Born, Born-virtual interference and real-emission cross sections, respectively. The added function is chosen to factorize into the corresponding Born cross section and the so-called dipoles. These are independent of the details of the process. The name dipole originates from the fact that starting from the Born process we have one particle where the emission of the extra parton happens. To ensure overall momentum conservation for an emission with finite energy and angle, a second parton, the so-called spectator, is needed.

For our process of VBF production, only the other parton on the same quark line needs to be considered as a spectator, as color correlations present in the dipoles will make the contributions where the spectator is part of the other quark line vanish. Therefore, for a final-state emission of the gluon on the upper line, there are two dipoles,  $\mathcal{D}_{35}^{1}$  and  $\mathcal{D}_3^{15}$  in the notation of Ref. [7]:

$$\begin{aligned}
\mathcal{D}_{35}^{1} &= \frac{1}{2p_3 \cdot p_5} \frac{1}{x_{35,1}} 8\pi\alpha_s C_F \left( \frac{2}{1 - \tilde{z}_3 + (1 - x_{35,1})} - (1 + \tilde{z}_3) \right) |\mathcal{M}_B(\tilde{p})|^2 \\
\mathcal{D}_3^{15} &= \frac{1}{2p_1 \cdot p_5} \frac{1}{x_{35,1}} 8\pi\alpha_s C_F \left( \frac{2}{1 - x_{15,3} + u_5} - (1 + x_{15,3}) \right) |\mathcal{M}_B(\tilde{p})|^2 ,
\end{aligned} \tag{25}$$

with

$$\begin{aligned}
x \equiv x_{35,1} &= \frac{p_1 \cdot p_3 + p_1 \cdot p_5 - p_3 \cdot p_5}{p_1 \cdot p_3 + p_1 \cdot p_5} , \\
z \equiv \tilde{z}_3 = 1 - u_5 &= \frac{p_1 \cdot p_3}{p_1 \cdot p_3 + p_1 \cdot p_5} ,
\end{aligned} \tag{26}$$

and the Born momenta are

$$\tilde{p}_1 = xp_1 , \quad \tilde{p}_3 = p_3 + p_5 - (1 - x)p_1 \tag{27}$$

with all other momenta unchanged. Combining everything yields our subtraction matrix element

$$|\mathcal{M}_{\mathcal{D},f}|^2 = \mathcal{D}_{35}^{15} + \mathcal{D}_3^{15} = 8\pi\alpha_s C_F \frac{1}{Q^2} \frac{x^2 + z^2}{(1-x)(1-z)} |\mathcal{M}_B(\tilde{p})|^2. \quad (28)$$

Combining everything and also adding the convolution with the parton densities gives for the subtracted real-emission process with final-state gluon emission

$$\begin{aligned} \sigma_{R,\text{subtr}} &= \int_0^1 dx_a \int_0^1 dx_b f_{q/p}(x_a, \mu_F) f_{q'/p}(x_b, \mu_F) \\ &\cdot \frac{1}{4p_1 \cdot p_2} \int d\text{PS}_{2 \rightarrow 7} \left( |\mathcal{M}_R|^2 F_J^{(3)} - |\mathcal{M}_{\mathcal{D},f}|^2 F_J^{(2)}(\tilde{p}) \right), \end{aligned} \quad (29)$$

where  $\mathcal{M}_R$  denotes the real-emission matrix element and  $F_J^{(3)}$  and  $F_J^{(2)}$  is a infrared soft and collinear safe jet algorithm for the 3 and 2-parton final state, where the latter uses the momenta  $\tilde{p}$  as input.

Similarly, for the real emission process where the gluon is in the initial state,  $g(p_1)q'(p_2) \rightarrow q(p_3)\bar{q}(p_5)q'(p_4)e^+(k_1)\nu_e(k_2)\mu^+(k_3)\nu_\mu(k_4)$ , we find [7, 49]:

$$\begin{aligned} |\mathcal{M}_{\mathcal{D},i}|^2 &= \mathcal{D}_3^{15} + \mathcal{D}_5^{13} \\ &= 8\pi\alpha_s T_R \frac{1-2x(1-x)}{x} \left( \frac{1}{2p_1 \cdot p_5} |\mathcal{M}_B^q(\tilde{p})|^2 + \frac{1}{2p_1 \cdot p_3} |\mathcal{M}_B^{\bar{q}}(\tilde{p})|^2 \right) \\ &= 8\pi\alpha_s T_R \frac{x^2 + (1-x)^2}{Q^2} \left( \frac{1}{1-z} |\mathcal{M}_B^q(\tilde{p})|^2 + \frac{1}{z} |\mathcal{M}_B^{\bar{q}}(\tilde{p})|^2 \right). \end{aligned} \quad (30)$$

The color factor  $T_R = \frac{1}{2}$  and  $\mathcal{M}_B^{\bar{q}}$  is the Born matrix element with a  $\bar{q}$  as incoming parton on the upper line.

As said before, we need to integrate these dipoles and add them back to the born-virtual interference. This contribution is called the  $I$ -operator. The term operator is chosen because it contains color matrices which act on the Born matrix element. As their effect is trivial for our VBF process, we have already inserted these into the expression and get for the squared matrix element

$$\begin{aligned} |\mathcal{M}_I|^2 &= \frac{\alpha_s}{2\pi} C_F \frac{1}{\Gamma(1-\epsilon)} \left( \frac{4\pi\mu^2}{2p_1 \cdot p_3} \right)^\epsilon \left( \frac{2}{\epsilon^2} + \frac{3}{\epsilon} + 10 - \pi^2 \right) |\mathcal{M}_B|^2 \\ &= C_\epsilon \frac{\alpha_s}{2\pi} C_F |\mathcal{M}_B|^2 \\ &\cdot \left( \frac{2}{\epsilon^2} + \frac{3 + 2 \ln \frac{\mu_R^2}{2p_1 \cdot p_3}}{\epsilon} + 10 - \pi^2 + 3 \ln \frac{\mu_R^2}{2p_1 \cdot p_3} + \ln^2 \frac{\mu_R^2}{2p_1 \cdot p_3} \right), \end{aligned} \quad (31)$$

where the momenta are those of the Born process. In the last step the constant  $C_\epsilon$  has been pulled out again and the rest has been fully expanded in  $\epsilon$ .

The poles in  $\frac{1}{\epsilon^2}$  and  $\frac{1}{\epsilon}$  now cancel exactly with the corresponding parts from the virtual amplitude and the Born and renormalized virtual part of the cross section is given by

$$\begin{aligned} \sigma_{B+V} &= \int_0^1 dx_a \int_0^1 dx_b f_{q/p}(x_a, \mu_F) f_{q'/p}(x_b, \mu_F) \\ &\cdot \frac{1}{4p_1 \cdot p_2} \int d\text{PS}_{2 \rightarrow 6} |\mathcal{M}_B|^2 F_J^{(2)} \left( 1 + \frac{\alpha_s(\mu_{R1}) + \alpha_s(\mu_{R2})}{2\pi} C_F (2 - \pi^2) \right). \end{aligned} \quad (32)$$

In this expression the virtual effects on the lower line have been included as well and we have introduced the option to choose different renormalization scales for the two corrections, which we are going to exploit later.

### 1. Initial-state Collinear Divergences

A slight complication actually occurs due to the presence of partons in the initial state, and is related to the fact that their momentum is fixed. The corresponding Born process with momentum  $\tilde{p}$  has a center-of-mass energy of  $\sqrt{x2p_1 \cdot p_2}$  instead of  $\sqrt{2p_1 \cdot p_2}$  and hence the divergences of virtual correction and real emission do not match. In the soft limit  $x \rightarrow 1$  and everything is fine. In the collinear limit the solution is to include the remaining divergence in a redefinition of the PDFs. These then also become scheme-dependent, as there is an ambiguity which finite parts are absorbed into the PDFs as well. The most common choice for hadron-hadron collisions is the  $\overline{\text{MS}}$  scheme. This induces an additional collinear-subtraction counterterm in our expression

$$|\mathcal{M}_C|^2 = -\frac{\alpha_s}{2\pi} \frac{1}{\Gamma(1-\epsilon)} \int_0^1 dx \left[ -\frac{1}{\epsilon} \left( \frac{4\pi\mu^2}{\mu_F^2} \right)^\epsilon P^{qg}(x) + K^{qg}(x) \right] |\mathcal{M}_B^q(\tilde{p})|^2. \quad (33)$$

Here,  $\mu_F$  denotes the factorization scale,  $P^{qg}(x) = C_F \frac{1+(1-x)^2}{x}$  is the DGLAP [72–74] splitting kernel, and  $K^{qg}(x) \stackrel{\overline{\text{MS}}}{=} 0$  denotes a possible additional finite part. Because of these two symbols appearing, this contribution is sometimes also referred to as the  $PK$ -operator.

The corresponding cross section contribution then yields [49]

$$\begin{aligned} \sigma_C = & \int_0^1 dx_a \int_0^1 dx_b \frac{\alpha_s}{2\pi} \int_{x_a}^1 \frac{dx}{x} \tilde{f}_{q/p}(x_a, x, \mu_F) f_{q'/p}(x_b, \mu_F) \\ & \cdot \frac{1}{4p_1 \cdot p_2} \int d\text{PS}_{2 \rightarrow 6} |\mathcal{M}_B|^2 F_J^{(2)}, \end{aligned} \quad (34)$$

where the additional contribution has been put into

$$\begin{aligned} \tilde{f}_{q/p}(x_a, x, \mu_F) = & f_{g/p} \left( \frac{x_a}{x}, \mu_F \right) A(x) \\ & + \left[ f_{q/p} \left( \frac{x_a}{x}, \mu_F \right) - x f_{q/p}(x_a, \mu_F) \right] B(x) \\ & + f_{q/p} \left( \frac{x_a}{x}, \mu_F \right) C(x) + f_{q/p}(x_a, \mu_F) \frac{D(x_a)}{1-x_a} \end{aligned} \quad (35)$$

with

$$A(x) = T_R [x^2 + (1-x)^2] \ln \frac{(1-x)Q^2}{x\mu_F^2} + 2T_R x(1-x) \quad (36)$$

$$B(x) = C_F \left[ \frac{1}{1-x} \ln \frac{(1-x)Q^2}{\mu_F^2} - \frac{3}{2} \frac{1}{1-x} \right] \quad (37)$$

$$C(x) = C_F \left[ 1-x - \frac{2}{1-x} \ln x - (1+x) \ln \frac{(1-x)Q^2}{x\mu_F^2} \right] \quad (38)$$

$$D(x_a) = C_F \left[ \frac{3}{2} \ln \frac{Q^2}{(1-x_a)\mu_F^2} + 2 \ln(1-x_a) \ln \frac{Q^2}{\mu_F^2} + \ln^2(1-x_a) - \frac{11}{2} + \frac{2\pi^2}{3} \right]. \quad (39)$$

Since this expression originates from a limit of the real-emission phase space, it is possible to rewrite the extra  $\int dx$  integration into an integral  $\int d^3p_5$ , such that this contribution can be combined together with the real-emission processes into a single integration of the real-emission phase space.

Then we obtain [49]

$$\sigma_C = \int_0^1 dx_a \int_0^1 dx_b \frac{1}{4p_1 \cdot p_2} \cdot \int d\text{PS}_{2 \rightarrow 7} \tilde{f}_{q/p}(xx_a, x, \mu_F) f_{q'/p}(x_b, \mu_F) \frac{8\pi\alpha_s}{Q^2} |\mathcal{M}_B|^2 F_J^{(2)}, \quad (40)$$

with  $\tilde{f}_{q/p}$  given in eq. (35). This procedure is used for example in the VBFNLO implementation [27, 28, 75, 76] of the VBF processes.

The total NLO cross section is then finally given by the sum of all contributions

$$\sigma_{\text{NLO}} = \sigma_{B+V} + \sigma_{R,\text{subtr}} + \sigma_C. \quad (41)$$

As mentioned before, for general VBF processes the final-state gauge bosons can also be radiated off the quark lines. In this case loop corrections with up to five external particles, i.e. pentagons can appear. It is convenient to group all loop corrections to the quark line together [51], as shown in Fig. 8. There the three vector bosons can be either the  $t$ -channel or final-state bosons, with the other quark line or the final-state leptons removed for clarity. The order of the vector bosons is fixed, a permutation of them is another fermion line. The divergent pieces of this diagram sum factorize against the Born again, while for the finite terms an additional contribution appears,  $\widetilde{\mathcal{M}}_5$ ,

$$\mathcal{M}_{V,5} \Big|_{\text{renorm}} = \frac{\alpha_s(\mu)}{4\pi} C_F \left( \mathcal{M}_B \left( \frac{4\pi\mu^2}{Q_1^2} \right)^\epsilon \frac{1}{\Gamma(1-\epsilon)} \left[ -\frac{2}{\epsilon^2} - \frac{3}{\epsilon} - 8 \right] + \widetilde{\mathcal{M}}_5 \right). \quad (42)$$

The exact choice of splitting the finite part is arbitrary, but taking the part not included in  $\widetilde{\mathcal{M}}_5$  to be the same as for the pure vertex correction is convenient for numerical implementations. Then the part proportional to the Born matrix element is the same for all virtual corrections. Also it turns out that with this choice the contribution of  $\widetilde{\mathcal{M}}_5$  is fairly small. As its evaluation is rather time-consuming due to the presence of pentagon loop functions, this

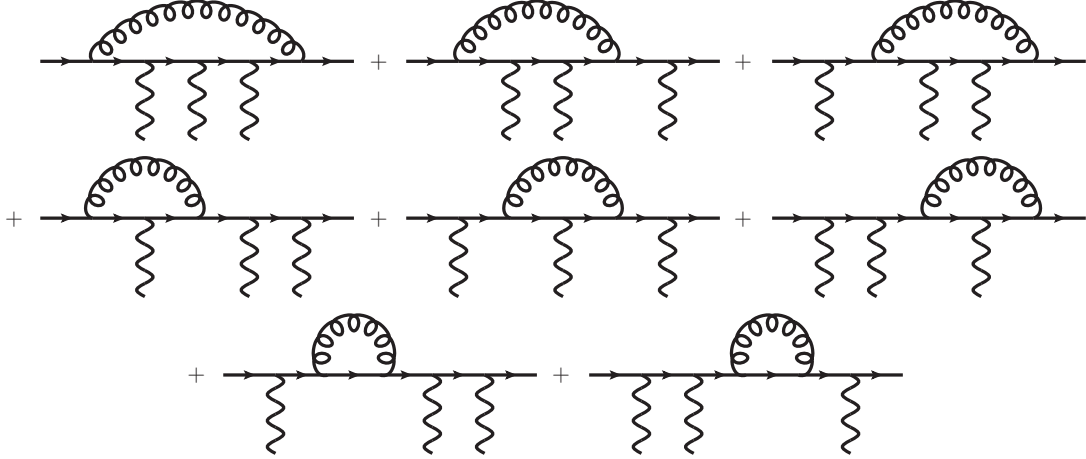


FIG. 8. NLO QCD loop corrections to the quark line with three attached gauge bosons. The order of the gauge bosons is the same between all diagrams.

allows us to integrate this part separately with less statistics without affecting the overall accuracy of the result.

These divergences are then canceled by the corresponding real-emission diagrams, where a gluon is emitted from the initial- or final-state quark. Gluon emission from internal quark lines yields only finite contributions.

## 2. Phenomenological Impact

Having everything in place, we can now evaluate NLO cross sections. A summary of reference values is given in Tables I and II, providing an updated version of Ref. [46].

As input parameters in the electroweak sector we choose the Fermi constant and  $W$ ,  $Z$  and the Higgs boson mass. The other electroweak parameters, namely the electromagnetic coupling and the weak mixing angle, are then fixed via tree-level relations. As numerical values we use [77]

$$\begin{aligned}
 M_W &= 80.385 \text{ GeV}, & \Gamma_W &= 2.097 \text{ GeV}, \\
 M_Z &= 91.1876 \text{ GeV}, & \Gamma_Z &= 2.508 \text{ GeV}, \\
 M_H &= 125.0 \text{ GeV}, & \Gamma_H &= 4.070 \text{ MeV}, \\
 G_F &= 1.16638 \cdot 10^{-5} \text{ GeV}^{-2}, \\
 \alpha^{-1} \equiv \alpha_{G_F}^{-1} &= 132.23308, & \sin^2(\theta_W) &= 0.22290.
 \end{aligned} \tag{43}$$

A set of minimal cuts is imposed on the transverse momenta and rapidities of the final-state charged leptons and photons as well as on their separation to simulate the capabilities of the experimental detectors.

$$\begin{aligned}
 p_{T,\ell(\gamma)} &> 20 \text{ GeV}, & |y_{\ell(\gamma)}| &< 2.5, \\
 R_{j\ell} &> 0.4, & R_{\ell\gamma} &> 0.4, \\
 R_{j\gamma} &> 0.7, & R_{\gamma\gamma} &> 0.4, \\
 M_{\ell^+\ell^-} &> 15 \text{ GeV}.
 \end{aligned} \tag{44}$$

LHC Process	$\sqrt{s} = 8 \text{ TeV}$		
	$\sigma_{\text{LO}}$	$\sigma_{\text{NLO}}$	K
$pp \rightarrow Hjj$ (“VBF- $H$ ”)	335.46(4) fb	316.23(2) fb	0.94
$pp \rightarrow Hjjj$ (“VBF- $H$ +jet”)	46.516(14) fb	37.56(18) fb	0.81
$pp \rightarrow HHjj$ (“VBF- $HH$ ”)	0.14812(3) fb	0.13821(10) fb	0.93
$pp \rightarrow H\gamma jj$ (“VBF- $H\gamma$ ”)	4.9768(7) fb	4.696(4) fb	0.94
$pp \rightarrow \ell^+ \ell^- jj$ (“VBF- $Z_\ell$ ”)	91.98(5) fb	93.77(17) fb	1.02
$pp \rightarrow \nu \bar{\nu} jj$ (“VBF- $Z_\nu$ ”)	230.11(12) fb	239.7(4) fb	1.04
$pp \rightarrow \ell^+ \nu jj$ (“VBF- $W^+$ ”)	882.77(16) fb	867.2(6) fb	0.98
$pp \rightarrow \ell^- \bar{\nu} jj$ (“VBF- $W^-$ ”)	471.24(9) fb	483.8(4) fb	1.03
$pp \rightarrow \gamma jj$ (“VBF- $\gamma$ ”)	2090.3(6) fb	2139(2) fb	1.02
$pp \rightarrow \ell_1^+ \nu_{\ell_1} \ell_2^- \bar{\nu}_{\ell_2} jj$ (“VBF- $W^+ W^-$ ”)	6.860(4) fb	6.704(13) fb	0.98
$pp \rightarrow \ell_1^+ \ell_1^- \ell_2^+ \ell_2^- jj$ (“VBF- $Z_\ell Z_\ell$ ”)	59.79(5) ab	61.11(15) ab	1.02
$pp \rightarrow \ell_1^+ \ell_1^- \nu_{\ell_2} \bar{\nu}_{\ell_2} jj$ (“VBF- $Z_\ell Z_\nu$ ”)	0.4279(3) fb	0.4313(13) fb	1.01
$pp \rightarrow \ell_1^+ \nu_{\ell_1} \ell_2^+ \ell_2^- jj$ (“VBF- $W^+ Z_\ell$ ”)	0.48291(18) fb	0.4718(8) fb	0.98
$pp \rightarrow \ell_1^- \bar{\nu}_{\ell_1} \ell_2^+ \ell_2^- jj$ (“VBF- $W^- Z_\ell$ ”)	0.22909(5) fb	0.2373(3) fb	1.04
$pp \rightarrow \ell_1^+ \nu_{\ell_1} \ell_2^+ \nu_{\ell_2} jj$ (“VBF- $W^+ W^+$ ”)	1.6778(5) fb	1.6230(14) fb	0.97
$pp \rightarrow \ell_1^- \bar{\nu}_{\ell_1} \ell_2^- \bar{\nu}_{\ell_2} jj$ (“VBF- $W^- W^-$ ”)	0.39862(11) fb	0.4411(12) fb	1.11
$pp \rightarrow \ell^+ \nu \gamma jj$ (“VBF- $W^+ \gamma$ ”)	11.004(3) fb	10.694(15) fb	0.97
$pp \rightarrow \ell^- \bar{\nu} \gamma jj$ (“VBF- $W^- \gamma$ ”)	5.5906(15) fb	5.695(7) fb	1.02
$pp \rightarrow \ell^+ \ell^- \gamma jj$ (“VBF- $Z_\ell \gamma$ ”)	2.2749(9) fb	2.310(4) fb	1.02
$pp \rightarrow \nu \bar{\nu} \gamma jj$ (“VBF- $Z_\nu \gamma$ ”)	5.2025(13) fb	5.335(6) fb	1.03
$pp \rightarrow q\bar{q}\ell^- \bar{\nu}_\ell jj$ (“VBF- $W_{\text{had}}^+ W^-$ ”)	6.138(5) fb	6.68(2) fb	1.09
$pp \rightarrow \ell^+ \nu_\ell q\bar{q} jj$ (“VBF- $W^+ W_{\text{had}}^-$ ”)	5.782(5) fb	6.31(3) fb	1.09
$pp \rightarrow \ell^+ \ell^- q\bar{q} jj$ (“VBF- $Z_\ell Z_{\text{had}}$ ”)	0.5284(6) fb	0.588(3) fb	1.11
$pp \rightarrow q\bar{q}\ell^+ \ell^- jj$ (“VBF- $W_{\text{had}}^+ Z_\ell$ ”)	0.5592(3) fb	0.5992(10) fb	1.07
$pp \rightarrow \ell^+ \nu_\ell q\bar{q} jj$ (“VBF- $W^+ Z_{\text{had}}$ ”)	2.3829(12) fb	2.500(6) fb	1.05
$pp \rightarrow q\bar{q}\ell^+ \ell^- jj$ (“VBF- $W_{\text{had}}^- Z_\ell$ ”)	0.24536(12) fb	0.2763(5) fb	1.13
$pp \rightarrow \ell^- \bar{\nu}_\ell q\bar{q} jj$ (“VBF- $W^- Z_{\text{had}}$ ”)	1.0994(6) fb	1.238(2) fb	1.13
$pp \rightarrow q\bar{q}\ell^+ \nu_\ell jj$ (“VBF- $W_{\text{had}}^+ W^+$ ”)	3.8878(15) fb	4.042(6) fb	1.04
$pp \rightarrow q\bar{q}\ell^- \bar{\nu}_\ell jj$ (“VBF- $W_{\text{had}}^- W^-$ ”)	0.8494(3) fb	1.0159(13) fb	1.20

TABLE I. Integrated cross sections for VBF production processes for the LHC running at a center-of-mass energy of 8 TeV using the cuts given in eq. (44). Results are given summed over all three lepton generations and, in case of quarks, all combinations which do not involve a top quark. The error in brackets is the statistical error from Monte Carlo integration.

LHC Process	$\sqrt{s} = 13 \text{ TeV}$		
	$\sigma_{\text{LO}}$	$\sigma_{\text{NLO}}$	K
$pp \rightarrow Hjj$ (“VBF- $H$ ”)	960.61(10) fb	906.2(5) fb	0.94
$pp \rightarrow Hjjj$ (“VBF- $H$ +jet”)	163.73(5) fb	131.9(8) fb	0.81
$pp \rightarrow HHjj$ (“VBF- $HH$ ”)	0.60364(12) fb	0.5613(4) fb	0.93
$pp \rightarrow H\gamma jj$ (“VBF- $H\gamma$ ”)	15.596(2) fb	14.666(11) fb	0.94
$pp \rightarrow \ell^+ \ell^- jj$ (“VBF- $Z_\ell$ ”)	265.69(15) fb	274.4(5) fb	1.03
$pp \rightarrow \nu \bar{\nu} jj$ (“VBF- $Z_\nu$ ”)	714.3(4) fb	750.8(13) fb	1.05
$pp \rightarrow \ell^+ \nu jj$ (“VBF- $W^+$ ”)	2319.4(4) fb	2317.4(15) fb	1.00
$pp \rightarrow \ell^- \bar{\nu} jj$ (“VBF- $W^-$ ”)	1387.3(3) fb	1432.1(9) fb	1.03
$pp \rightarrow \gamma jj$ (“VBF- $\gamma$ ”)	5327.1(15) fb	5528(9) fb	1.04
$pp \rightarrow \ell_1^+ \nu_{\ell_1} \ell_2^- \bar{\nu}_{\ell_2} jj$ (“VBF- $W^+ W^-$ ”)	22.691(13) fb	22.30(4) fb	0.98
$pp \rightarrow \ell_1^+ \ell_1^- \ell_2^+ \ell_2^- jj$ (“VBF- $Z_\ell Z_\ell$ ”)	228.90(16) ab	234.0(7) ab	1.02
$pp \rightarrow \ell_1^+ \ell_1^- \nu_2 \bar{\nu}_2 jj$ (“VBF- $Z_\ell Z_\nu$ ”)	1.5654(9) fb	1.581(4) fb	1.01
$pp \rightarrow \ell_1^+ \nu_{\ell_1} \ell_2^+ \ell_2^- jj$ (“VBF- $W^+ Z_\ell$ ”)	1.7056(7) fb	1.679(2) fb	0.98
$pp \rightarrow \ell_1^- \bar{\nu}_{\ell_1} \ell_2^+ \ell_2^- jj$ (“VBF- $W^- Z_\ell$ ”)	0.9164(3) fb	0.9424(9) fb	1.03
$pp \rightarrow \ell_1^+ \nu_{\ell_1} \ell_2^+ \nu_{\ell_2} jj$ (“VBF- $W^+ W^+$ ”)	5.7321(17) fb	5.616(4) fb	0.98
$pp \rightarrow \ell_1^- \bar{\nu}_{\ell_1} \ell_2^- \bar{\nu}_{\ell_2} jj$ (“VBF- $W^- W^-$ ”)	1.7388(5) fb	1.8785(18) fb	1.08
$pp \rightarrow \ell^+ \nu \gamma jj$ (“VBF- $W^+ \gamma$ ”)	32.412(10) fb	31.98(3) fb	0.99
$pp \rightarrow \ell^- \bar{\nu} \gamma jj$ (“VBF- $W^- \gamma$ ”)	18.496(5) fb	18.88(2) fb	1.02
$pp \rightarrow \ell^+ \ell^- \gamma jj$ (“VBF- $Z_\ell \gamma$ ”)	7.406(3) fb	7.560(14) fb	1.02
$pp \rightarrow \nu \bar{\nu} \gamma jj$ (“VBF- $Z_\nu \gamma$ ”)	18.123(5) fb	18.62(3) fb	1.03
$pp \rightarrow q\bar{q} \ell^- \bar{\nu}_\ell jj$ (“VBF- $W_{\text{had}}^+ W^-$ ”)	22.384(18) fb	24.97(7) fb	1.12
$pp \rightarrow \ell^+ \nu_\ell q\bar{q} jj$ (“VBF- $W_{\text{had}}^+ W^-$ ”)	21.075(17) fb	23.44(9) fb	1.11
$pp \rightarrow \ell^+ \ell^- q\bar{q} jj$ (“VBF- $Z_\ell Z_{\text{had}}$ ”)	2.186(3) fb	2.455(19) fb	1.12
$pp \rightarrow q\bar{q} \ell^+ \ell^- jj$ (“VBF- $W_{\text{had}}^+ Z_\ell$ ”)	2.0880(10) fb	2.304(4) fb	1.10
$pp \rightarrow \ell^+ \nu_\ell q\bar{q} jj$ (“VBF- $W_{\text{had}}^+ Z_{\text{had}}$ ”)	9.046(5) fb	9.71(2) fb	1.07
$pp \rightarrow q\bar{q} \ell^+ \ell^- jj$ (“VBF- $W_{\text{had}}^- Z_\ell$ ”)	1.0516(5) fb	1.1991(19) fb	1.14
$pp \rightarrow \ell^- \bar{\nu}_\ell q\bar{q} jj$ (“VBF- $W_{\text{had}}^- Z_{\text{had}}$ ”)	4.670(2) fb	5.347(11) fb	1.14
$pp \rightarrow q\bar{q} \ell^+ \nu_\ell jj$ (“VBF- $W_{\text{had}}^+ W^+$ ”)	13.942(5) fb	14.960(15) fb	1.07
$pp \rightarrow q\bar{q} \ell^- \bar{\nu}_\ell jj$ (“VBF- $W_{\text{had}}^- W^-$ ”)	3.9314(15) fb	4.685(7) fb	1.19

TABLE II. Integrated cross sections for VBF production processes for the LHC running at a center-of-mass energy of 13 TeV using the cuts given in eq. (44). Results are given summed over all three lepton generations and, in case of quarks, all combinations which do not involve a top quark. The error in brackets is the statistical error from Monte Carlo integration.



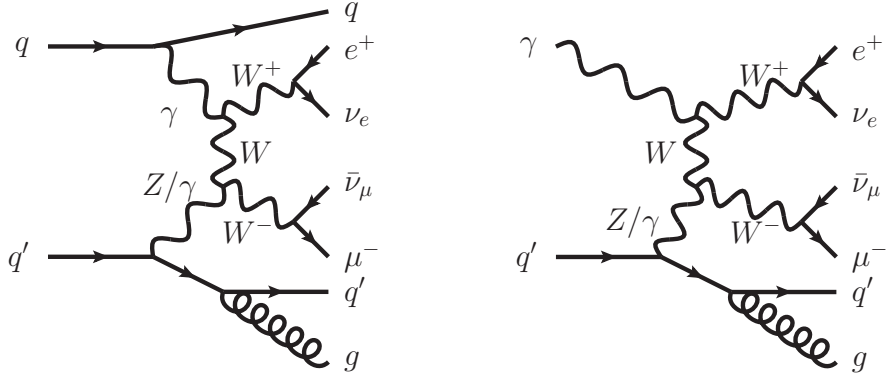


FIG. 9. Example Feynman diagrams of a VBF process (VBF- $W^+W^-$  production) where a  $t$ -channel photon can develop a QED divergence. *Left*: real-emission diagram with divergence, *right*: corresponding Born diagram which would provide the contribution to cancel the divergence.

The last cut is chosen to remove singularities from a virtual photon splitting into a pair of charged leptons,  $\gamma^* \rightarrow \ell^+\ell^-$ .

All final-state partons with pseudorapidity  $\eta < 5.0$  are clustered into jets with the anti- $k_T$  algorithm [78, 79] using an  $R$  separation parameter of 0.4. Jets are required to have a transverse momentum  $p_{T,j} > 30$  GeV and rapidity  $|y_j| < 4.5$ . A fixed  $R$  separation cut between partons and jets would spoil the cancellation of infrared singularities. Therefore, to separate final-state jets and photons, we employ the procedure suggested by Frixione in Ref. [80]. An event is only accepted, if the condition

$$\sum_i E_{T,i} \Theta(\delta - R_{i\gamma}) \leq p_{T,\gamma} \frac{1 - \cos \delta}{1 - \cos \delta_0} \quad \forall \delta \leq \delta_0 \quad (45)$$

is fulfilled. Thereby,  $E_{T,i}$  denotes the transverse energy of parton  $i$ ,  $p_{T,\gamma}$  the transverse momentum of the photon and  $R_{i\gamma}$  their separation. In our setup we choose the separation parameter  $\delta_0 = 0.7$ . The formula given above avoids the QED IR divergence from collinear emission of a photon from a quark, while at the same time allowing final-state gluons arbitrarily close to the direction of the photon as long as these are soft enough, thus retaining the full QCD pole.

Another issue arises in VBF processes where an exchanged virtual photon can become on-shell. An example Feynman diagram where this can occur is given on the left-hand side of Fig. 9, taking VBF- $W^+W^-$  production as an example. If both the final-state quark on the lower line and the gluon are hard enough and well separated to be identified as the two tagging jets of the process, the transverse momentum of the upper quark is no longer restricted. In particular it can become collinear to the beam axis, i.e.  $p_1 \parallel p_3$ . In this case, the momentum transfer becomes zero and the photon propagator develops a divergence. Note that this issue can only appear in the real-emission part, as for Born kinematics both quarks need to have a finite transverse momentum to be identified as the tagging jets. Also, if only massive bosons can appear in the  $t$ -channel, like in VBF- $H$  or VBF- $W^+W^+$  production, the divergence is regulated by the mass of the exchanged boson. The origin of this QED divergence is the fact that this diagram is also the real-emission correction to another process,

namely  $\gamma q' \rightarrow q' g e^+ \nu_e \bar{\nu}_\mu \mu^-$ . The corresponding Feynman diagram is depicted on the right-hand side of Fig. 9. The virtual corrections to this process and the  $\mathcal{O}(\alpha)$  corrections to the photon PDF will then generate the same terms, but with a relative minus sign, so that the divergences cancel. To calculate this, we would also need the parton density of photons in the proton. Such PDF sets are in principle available nowadays, but have quite large errors on the photon densities [81–83]. To avoid adding this contribution altogether, we can alternatively introduce a technical cut on the photon virtuality. In our case we choose  $Q^2 > 4 \text{ GeV}^2$ . Varying this cut then gives an estimate on the error introduced by this procedure, which turns out to be small and overall negligible [50]. One can understand the smallness also from the kinematic structure of these events. As  $Q^2$  approaches zero, the final-state quark has no transverse momentum and is lost in the beam pipe. Therefore, the extra gluon emission must form the second jet of the VBF signature. For both the quark and the gluon radiated from it to be identified as tagging jets, the latter needs to be a very hard and wide-angle emission, which induces a large suppression factor from the matrix element.

In order to exploit the particular properties of our VBF signature, we require the presence of at least two jets in the final state. The two jets with the largest transverse momentum are labeled tagging jets and must additionally fulfill

$$|\Delta y_{jj}| > 3.6, \quad m_{jj} > 600 \text{ GeV}. \quad (46)$$

For processes with semi-leptonic decays of the vector bosons, where additional jets due to these decays appear in the final-state, the jet pair with an invariant mass closest to the vector boson mass is removed first before applying the tagging jet criterion above.

As PDFs we choose the CT14llo set [84] with  $\alpha_s(m_Z) = 0.130$  at LO and the central set of PDF4LHC15\_nlo at NLO having  $\alpha_s(m_Z) = 0.118$ , using the implementation provided by LHAPDF [85].

Looking at the results for the LHC running 8 and 13 TeV center-of-mass energy given in Tables I and II, respectively, we see that the NLO QCD corrections are modest, typically ranging in the  $\pm 10\%$  range. Comparing with the results in Ref. [46], the more relaxed jet cuts give in general larger cross sections. Also the CT14llo set produces larger PDF values in the relevant  $x$  regions than the older CTEQ6L1 sets used in Ref. [46], while the difference in the used NLO sets is smaller. Hence, the  $K$  factors are consistently smaller here.

Factorization and renormalization scale have been taken as the virtuality of the  $t$ -channel gauge bosons,  $\mu_{F,i} = \mu_{R,i} = \sqrt{Q_i^2}$ . Thereby, we use independent values for the PDFs, loop corrections or gluon emissions on the upper line and on the lower line. As we have already seen in the analytic calculations above, e.g. eq. (10), this is the relevant scale appearing in the process, so should be a good choice.

An estimate of missing higher-order corrections is given by varying factorization and renormalization scale or taking other sensible choices, as the scale dependence of cross sections is an artifact of the truncation of the perturbative series and vanishes for calculations to all orders. Besides the virtuality of the exchanged bosons, we consider also two other choices. One is simply a fixed scale, where as central value we use  $2M_W$ , taking again our example process of VBF- $W^+W^+jj$  production. The second option we are going to use is the transverse momentum of the leading jet. This observable has the advantage that it is directly observable and also well-defined once we include additional parton-shower and hadronization effects.

Numerical results are shown in Fig. 10. On the left we use the virtuality of the exchanged bosons as central value  $\mu_{Q^2}$  and vary this with a factor  $\xi$  from 0.1 to 10. At LO, as no

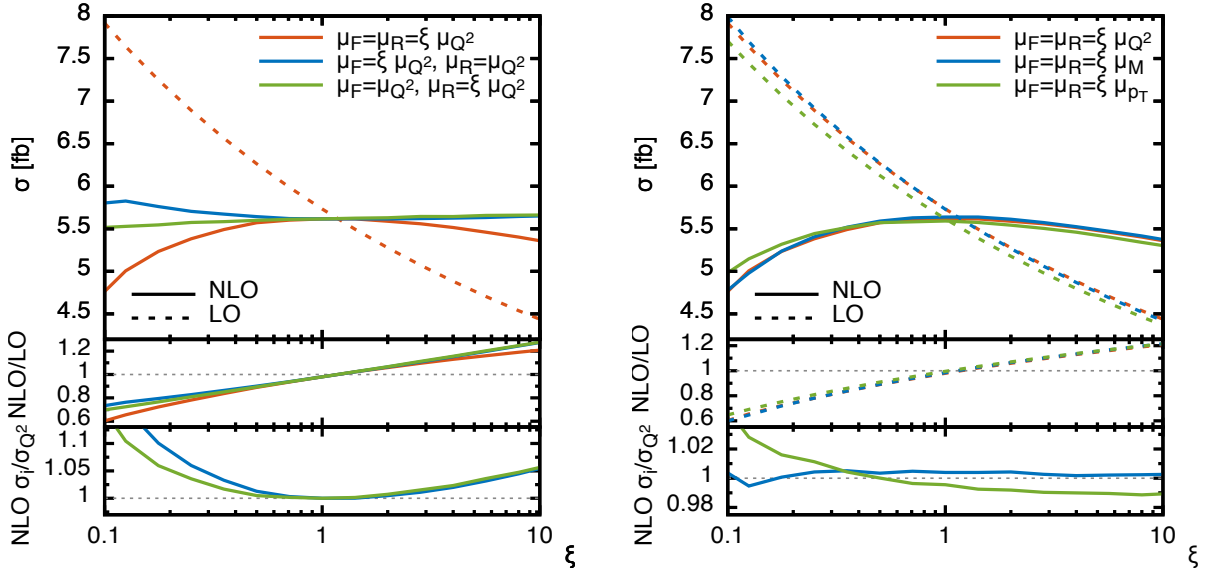


FIG. 10. Scale variation of the LO and NLO cross sections for the process  $pp \rightarrow e^+ \nu_e \mu^+ \nu_\mu jj$  (“VBF- $W^+W^+jj$ ”) for the LHC at 13 TeV center-of-mass energy. *Left:* Joint and independent variation of the factorization scale  $\mu_F$  and renormalization scale  $\mu_R$  using the virtuality  $Q^2$  of the exchanged bosons as central value. *Right:* Comparison of three different choices for the central scale: virtuality  $Q^2$ , fixed value  $\mu_M = 2M_W$  and transverse momentum  $p_T$  of the leading jet. The smaller panels in both plots show the ratio of NLO over LO cross sections in the upper one and in the lower one the cross section ratio over a joint scale variation using  $\mu_{Q^2}$  as the central scale.

factors of  $\alpha_s$  are present in the cross section, the dependence is purely on the factorization scale. A conventional estimate for the associated errors is given by a scale variation with a factor between  $\frac{1}{2}$  and 2, which here yields a cross section variation of +9.3% and  $-8.0\%$ , respectively. At NLO, the scale dependence is very flat in the central region, with a remaining scale variation uncertainty of around  $-0.8\%$  when varying both scales either jointly or only one of them. In the two smaller panels below we plot ratios of cross sections. The upper of those shows the  $K$  factor, the ratio of NLO over the LO cross section. While in the central range around  $\xi = 1$  the two agree reasonably well, for smaller or larger values the strong scale dependence of the LO cross section induces  $K$  values significantly different from 1. The lowest panel contains the ratio of individual scale variations over the joint one, again showing a very small spread in the different predictions except for very small or large values of  $\xi$ .

The right plot in Fig. 10 compares the three different scale choices, virtuality  $Q^2$ , fixed value  $M$  and leading-jet transverse momentum  $p_T$  for a joint factorization and renormalization scale variation. Similar to the previous case, the quite significant scale dependence at LO is vastly reduced for the NLO results, namely around one percent for both fixed value and momentum transfer. The middle panel shows again the  $K$  factor, which is basically independent of the scale type choice. In the lowest panel we finally compare cross section ratios of the three scale types. Choosing different scale types can serve as another method of obtaining a scale variation error. However, also there we only get a difference of  $0.4\%$  when comparing the central values and  $1.3\%$  when additionally taking a variation within  $\xi \in [0.5; 2]$  into account.

Such tiny numbers should however be taken with a grain of salt, as the variation by a factor 2 is purely conventional and there are numerous examples where this underestimates known higher-order corrections. Also, the effect of new topologies opening up, like double-gluon exchange between the quark lines, is not covered by this scale variation procedure at all. We will see in the last section of this chapter how the known 2-loop corrections in VBF- $H$  production modify this picture.

Finally, the central values of the PDFs and  $\alpha_s$  are only determined with a finite accuracy, as they are extracted from a large number of different experimental measurements. Modern PDF sets contain different member sets besides the best-fit one, where the internal parameters are varied along the eigenvectors of their correlation matrix within the uncertainties given by the experimental input. Taking the minimum and maximum value of the different results then yields the PDF variation uncertainty. Using the PDF4LHC15\_nlo\_30\_pdfas set [86], which is a compressed [87–89] set combining the latest results of the three main PDF fitting groups CTEQ [84], MMHT [90] and NNPDF [91], we obtain variations of  $-0.7\%$  and  $+1.2\%$  compared to the central set. Consistently varying  $\alpha_s(M_Z)$  to 0.0165 and 0.0195 both in the PDF and the matrix element changes the cross section by  $\pm 0.2\%$ , respectively.

## B. NLO Electroweak Corrections

Corrections beyond the NLO QCD level are known so far only for VBF- $H$  production. While a definitive statement about these effects for other VBF processes can only be made once they have been explicitly calculated, the expectation is that the general features will be similar in all VBF processes.

The first type we are going to discuss are electroweak corrections to VBF- $H$  production [92–94]. The virtual corrections are much richer than for the QCD case. Some example Feynman diagrams are shown in Fig. 11. Besides loop contributions to the  $qqV$  vertices, now also the  $VVH$  vertex receives corrections, either by a loop of electroweak gauge bosons or a closed loop of heavy, third-generation fermions. Gauge bosons can also connect the two quark lines, giving rise to loop diagrams up to the pentagon level. Whenever a photon is attached to an external quark, the corresponding diagram shows an infrared divergence. These need to be canceled by corresponding real-emission diagrams with an additional external photon. These can be either in the final-state or appearing in the initial-state as partons coming from the proton. For the latter case, corresponding QED PDFs are necessary for the calculation. Emission of heavy vector bosons does not need to be taken into account. Due to their finite mass, no divergences appear in the soft or collinear limit, and their decay products leave extra signatures in the detector, so these processes are clearly distinguishable. The diagrams also point to the main difficulty in calculating the electroweak corrections for other VBF processes. There will always be diagrams where all external particles are connected by one big loop like the pentagon diagram for VBF- $H$ . So for single  $V$  production these are hexagons and for vector-boson scattering with decays one needs to compute octagons, loops with eight external particles. Both of them are challenging in terms of numerical stability as well as run time.

For a Higgs boson of 125 GeV, the size of the NLO electroweak correction on the total VBF- $H$  cross section is around  $-5\%$  [92–94], and therefore of the same size as the NLO QCD corrections. Applying typical VBF cuts changes this value only mildly. The photon-induced real-emission processes thereby lead to a small reduction of the corrections by about 1% of the Born cross section.

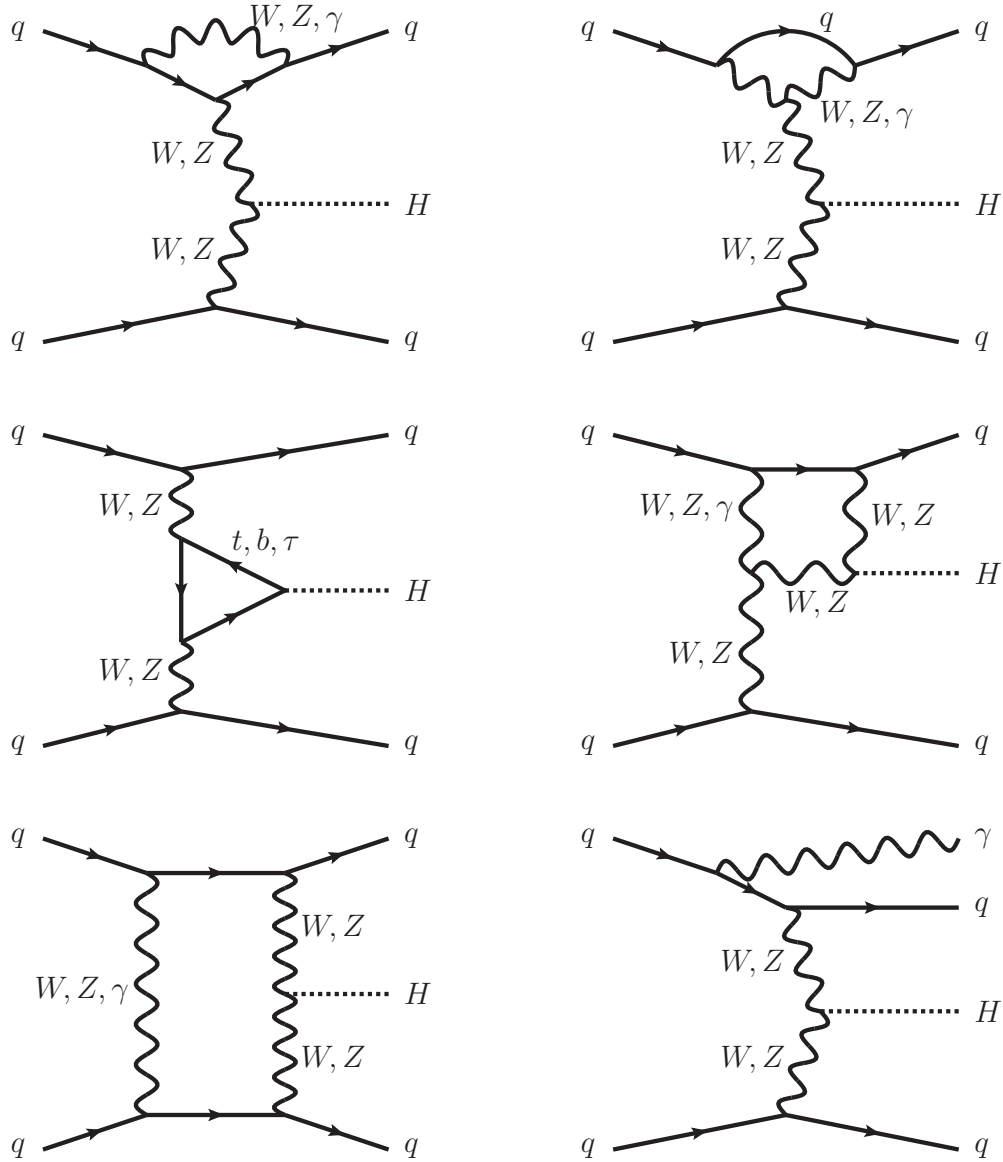


FIG. 11. Example Feynman diagrams of electroweak corrections in VBF- $H$  production. When selecting specific values for the quark flavors or gauge bosons, electromagnetic charge conservation needs to be taken into account.

In Fig. 12, generated with HAWK [95], we show the effects on two important distributions, namely the transverse momentum of the leading jet and the invariant mass of the two tagging jets. The left panels in the figure show the absolute distributions both for LO and the combined NLO QCD and EW contribution and the right panels their relative effects both separately and jointly. Looking at the various curves, we see that for the transverse-momentum distribution the two types of corrections show a similar behavior. They are fairly modest for small values and rise significantly when going to larger transverse momenta, reaching almost 60% for a value of 400 GeV. The same effect also happens for the second

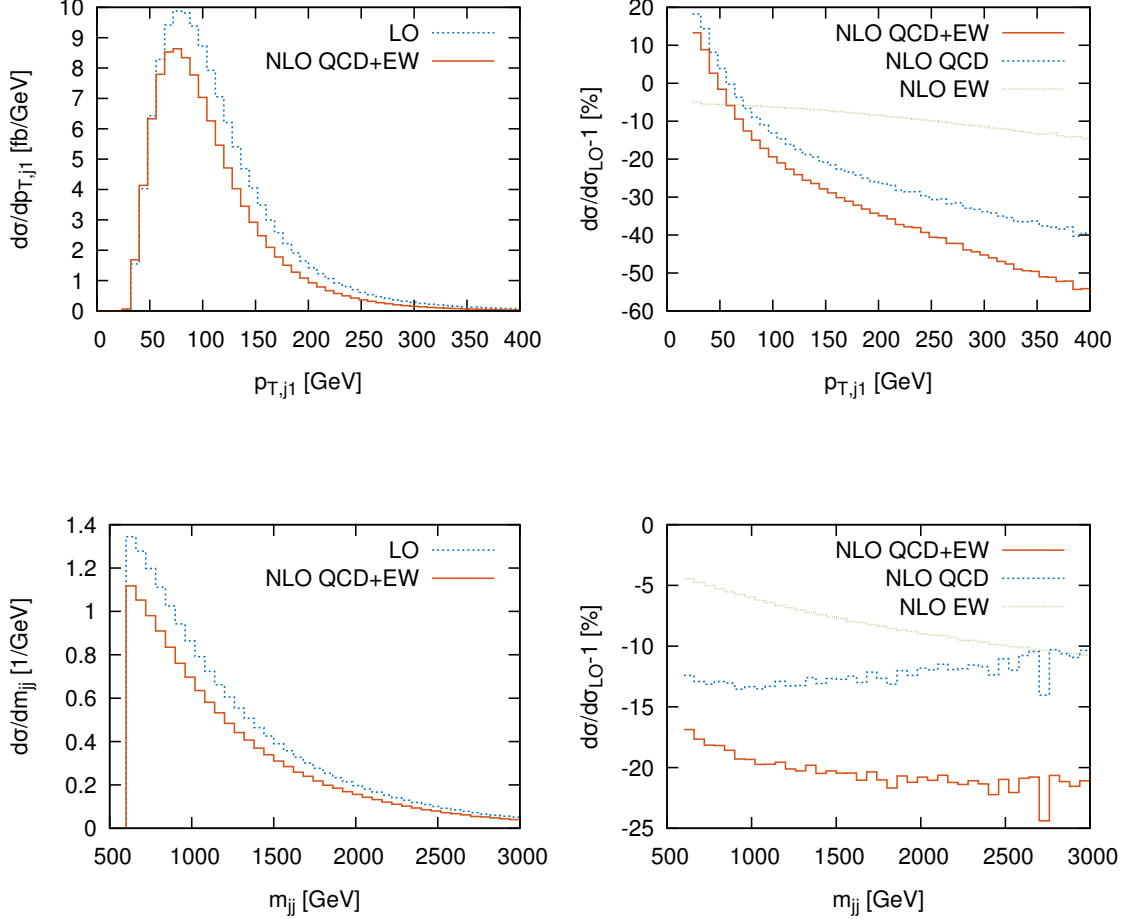


FIG. 12. NLO QCD and EW effects in VBF- $H$  production with VBF cuts for the LHC with 13 TeV center-of-mass energy. *Top row*: Transverse momentum distribution of the leading jet. *Bottom row*: Invariant mass distribution of the two tagging jets.

tagging jet, inducing corrections of more than  $-40\%$  for transverse momenta larger than 150 GeV. EW corrections hence lead to a significantly larger suppression of tagging jets with large transverse momenta compared than would be expected from QCD effects alone. The situation is different for the invariant mass of the two tagging jets, shown in the bottom row of Fig. 12. Here the mass dependence of QCD and EW corrections approximately cancels between the two for large invariant-mass values, leading to a flattening of the correction with a numerical value of about  $-20\%$ .

### C. QCD Corrections beyond NLO

Another class of contributions beyond NLO QCD are the NNLO QCD corrections. As with the NLO EW corrections, these have been considered only for VBF- $H$  production so far. Also, the results are known only in the VBF approximation discussed at the end of section II, where the two quarks coming from the proton are assumed to be in two separate

copies of the color  $SU(3)$  group. Hence, the only contributions are loop corrections to the  $qqV$  vertices and real-emission diagrams without interference of emissions from the upper and lower line. The two-loop virtual diagram with two gluons exchanged between the quark lines, which is color-suppressed compared to other two-loop matrix elements, is neglected in this structure-function approach. The NNLO QCD corrections to the inclusive cross section have been computed in Ref. [96, 97] and are found to be very small, on the order of 0.4%. The uncertainty determined by varying factorization and renormalization scale around the central choice of momentum transfer  $Q$  is further reduced compared to the NLO QCD value. Recently, also the N3LO QCD corrections for the inclusive cross section in the structure-function approach have been calculated [98, 99]. Their impact is tiny, at the level of 0.1 – 0.2%, which is well covered by the scale variation band of the NNLO QCD calculation. The remaining scale uncertainty is also at the per mill level.

The NNLO QCD calculation has been recently extended to differential cross sections in Ref. [100]. The calculation uses a trick, which is possible due to the rather simple QCD structure of the diagram. It is based on the fact that the knowledge of the momentum-transfer vectors  $q_i$ , when combined with both quarks being on-shell and the incoming ones along the  $z$ -axis, allows to fully reconstruct the four-vectors of the external quarks in the Born diagram. The inclusive corrections given by the structure function approach yield the loop contributions and the corresponding single and double real-emission contributions, with extra radiation integrated out, combined in one single number per Born event. This can then be augmented by the contributions with a single real emission and a one-loop vertex correction and the ones with two real emissions. These contain the extra emissions explicitly and therefore have the correct momentum structure of the real-emission events instead of the integrated out net effect. The necessary ingredients are given exactly by the NLO QCD calculation of electroweak  $H + 3$  jets production [101–103]. To remove the double-counting just introduced, we finally need to project these extra-emission events back to their corresponding Born structure. To this end we require that the momentum transfer  $q_i$  stays unchanged and then recompute the external quark momenta. These projected events then enter with the same absolute weight as the real-emission one but opposite sign and thus cancel their corresponding contribution in the structure-function part.

In Fig. 13 we present differential distributions, taken from Ref. [100]. Plotted results are the LO, NLO and NNLO QCD differential cross sections, all evaluated in the VBF approximation and with VBF cuts applied. The fourth set of bins is the NLO QCD calculation combined with parton shower effects (see section IV for more details), using the POWHEG-Box implementation [104] combined with Pythia 6.428 with the Perugia 2012 tune [105]. The left panel shows again the transverse momentum of the leading jet. From the lower part, where the relative difference to the NLO QCD curve is plotted, we see that the general feature of the NNLO QCD corrections is a reduction in the cross section of up to 10%, except for small transverse momenta where instead an enhancement occurs. The underlying cause for this is assumed to come from a redistribution of the jets from higher to lower transverse momenta, and this makes it more difficult to fulfill the VBF cuts, thus reducing the cross section [100]. These corrections are generally outside the scale variation bands of the NLO cross section and only at larger transverse-momentum values do they start to overlap. Comparing to the NLO plus parton-shower curve instead yields smaller deviations, but still outside the scale variation bands.

In the right panel the rapidity difference between the two tagging jets is plotted. The NNLO compared to the NLO curve yields corrections of up to 10% again, with negative

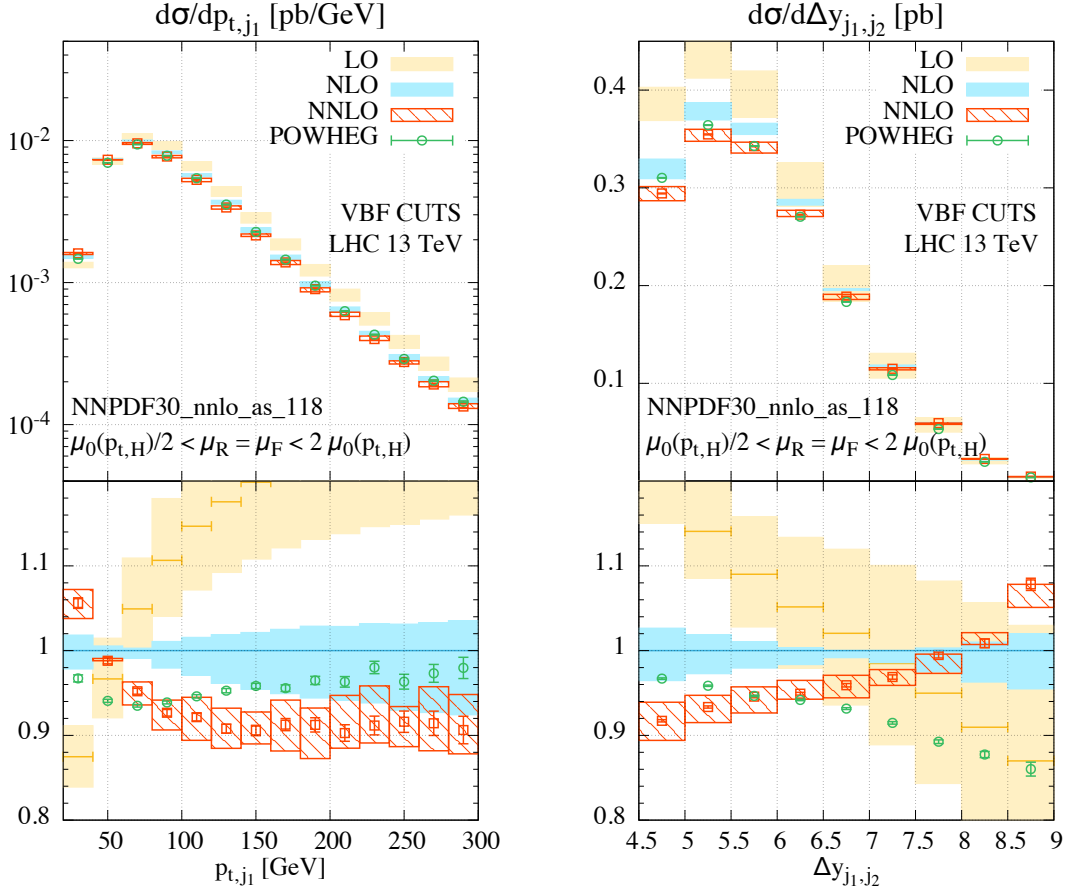


FIG. 13. Differential cross section for VBF- $H$  production at the LHC up to NNLO QCD and NLO QCD combined with parton shower (POWHEG-BOX and Pythia 6). Shown distributions are the transverse momentum of the leading jet (*left*) and the rapidity difference of the two tagging jets (*right*). The vertical bars denote the statistical error, and the boxes give the uncertainty from varying factorization and renormalization scales jointly by factors  $\frac{1}{2}$  and 2 around the central scale  $\mu_0 = \frac{M_H}{2} \sqrt{\frac{M_H^2}{4} + p_{T,H}^2}$ . Figure taken from Ref. [100].

values for small rapidity differences and rising to positive values for large ones. As before the corrections are not covered by the scale variation estimates. For this distribution adding parton-shower effects does not help at all, but instead increases the deviations when compared to the NNLO curve.

Overall, additional effects beyond the NLO QCD accuracy are expected to yield corrections to inclusive cross sections and in particular to distributions of the order of several percent. In the tails of distributions effects of up to 10% have been observed. The uncertainty estimate from performing scale variation clearly underestimates these corrections. As mentioned before, the small values obtained there should be taken with the necessary caution.



## IV. PARTON SHOWER EFFECTS

For a useful comparison between theory and experiment, it is necessary to bring the fixed-order parton-level calculations, which we have considered so far, closer to quantities actually measured by experiments. In the language of Monte-Carlo event generators, the fixed-order parton-level process, calculated via perturbation theory is often called the hard process. At LO, the final-state partons are directly identified with the jets, streams of clustered hadrons, observed in the detector. At NLO, as we have already shortly mentioned in the previous chapter, we need to apply a so-called jet algorithm. This ensures that when radiation becomes soft or collinear, the event asymptotically approaches its corresponding Born configuration, thereby ensuring the cancellation of the poles with their corresponding counterparts from the virtual expression. An extra jet can only appear for hard, wide-angle emissions. This behavior is known as the infrared-safeness of observables. The typical scale of the hard process is given by the factorization scale. They give us a good description of inclusive observables with hard and well-separated jets.

What the detector ultimately observes is inclusive only within a size the order of a single detector cell, so actually a very fine-grained picture. When we reduce the energy and angular-separation requirements, we will gradually start to see more and more jets emerging. To model this from the theory side with corresponding hard processes quickly becomes cumbersome. Therefore, a different approach is used, which starts from the hard process and generates additional radiation by a unitary procedure, the so-called parton shower. We will describe the details necessary for our VBF discussion in the following section.

After several steps, eventually the energy of the partons has dropped to a level where the strong coupling constant  $\alpha_s$  becomes very large and any perturbative description breaks down. The usual scale for this to happen is around 1 GeV. There, the transition from colored partons into color-neutral hadrons takes place. Combining the partons is modeled non-perturbatively, taking into account information from momenta, quark flavor and color assignment of the partons. Finally, these hadrons, which at this stage also contain excited and short-lived states, decay into the long-lived objects that are able to hit the detector elements, namely protons, neutrons, pions and Kaons, together with electrons, muons and photons.

These two steps, parton shower and hadronization, are the task of Monte Carlo event generators. The most common choices nowadays are Herwig 7 [106, 107], with its predecessors HERWIG [108, 109] and Herwig++ [110], Pythia 8 [111] and the previous Pythia 6 [112], and Sherpa [113].

In the following, we will first introduce the main concepts and formulae of parton showers, and then discuss the consequences for VBF production processes. Hadronization effects do not play any particular role, so we are not going to cover this topic further. This, and a more in-depth discussion of general features of Monte Carlo event generators, can be found in Refs. [114–117]. The discussion in the next section follows the presentation in Ref. [117].

### A. Parton Shower Overview

#### 1. Parton Shower with Born Matrix Elements

The main properties on which parton showers are based are unitarity and collinear factorization. The latter states that in the collinear limit, the emission of an extra parton  $j$

from an emitter  $i$  can be written as

$$d\sigma = \sigma_B \sum_{i,j} \frac{\alpha_s}{2\pi} \frac{d\theta^2}{\theta^2} P_{ij}(z) dz d\phi. \quad (47)$$

Here,  $z$  is the energy fraction of the emission  $j$ , and  $\theta$  the emission angle, which can be replaced by any other variable linearly dependent on the angle, like the transverse momentum  $p_T$  or the virtuality  $Q$ , without changing the expression. Eq. 47 neglects interference effects between different emissions, which do not play a role, and so we can build up the whole evolution as a sequence of single emissions.  $P_{ij}$  are the DGLAP splitting kernels [72–74], which we have already seen in the previous chapter. Their explicit form, averaged over azimuthal angles and spins, is

$$\begin{aligned} P_{qq}(z) &= C_F \frac{1+z^2}{1-z}, \\ P_{gq}(z) &= C_F \frac{1+(1-z)^2}{z}, \\ P_{qg}(z) &= C_A \frac{(1-z(1-z))^2}{z(1-z)}, \\ P_{gg}(z) &= T_R(1-2z(1-z)), \end{aligned} \quad (48)$$

with the color factors  $C_F = \frac{4}{3}$ ,  $C_A = 3$  and  $T_R = \frac{1}{2}$ . The poles when integrating eq. (47) would again be canceled by corresponding virtual loop diagrams. To avoid their explicit calculation, we can employ two arguments. First, in the limit where the energy fraction  $z$  approaches 0 or 1 or the angle  $\theta$  goes to 0, whether an emission happens or not becomes indistinguishable. So we can introduce cutoffs  $z_{\pm}(\theta)$  that eliminate these regions. Second, unitarity tells us that the combined probability of having an emission or not having one must sum to 1. This also ensures that the leading logarithmic behavior of the virtual corrections is correctly modeled by the parton shower. Finally, the hard process gives the starting value for the parton shower, e.g. for the opening angle  $\theta$ ,  $\theta_{\max}$ . The probability density for the first branching happening at an angle  $\theta$ ,  $d\Delta_i(\theta_{\max}, \theta)$ , is given by the probability of having no emission up to  $\theta$  times the emission probability within an infinitesimal interval  $d\theta$  around  $\theta$ , which is given by  $\frac{\alpha_s}{2\pi} \frac{d\theta^2}{\theta^2} \int_{z_-(\theta)}^{z_+(\theta)} P_{ij}(z) dz$ . This differential expression can be integrated and yields the so-called Sudakov form factor

$$\Delta_i(\theta_{\max}, \theta) = \exp \left( - \sum_j \int_{\theta^2}^{\theta_{\max}^2} \frac{d\tilde{\theta}^2}{\tilde{\theta}^2} \int_{z_-(\tilde{\theta})}^{z_+(\tilde{\theta})} dz \frac{\alpha_s}{2\pi} P_{ij}(z) \right), \quad (49)$$

the probability of not having any resolvable emission between  $\theta_{\max}$  and  $\theta$ . The  $\alpha_s$  factor has been moved in the innermost integral, as it is a function of the renormalization scale, whose choice may depend on both  $z$  and  $\theta$ . The probability for an emission at an angle  $\theta_1$  is then given by  $\frac{d\Delta_i(\theta_{\max}, \theta_1)}{d\theta_1}$ . The individual branchings should be ordered. Hence, the probability for the second emission  $\theta_2$  has now  $\theta_1$  as its starting value. With this, we can build up the full tower of emissions until we reach the lower cutoff, where we can no longer resolve any emissions.

The expressions we have discussed so far are for radiation off final-state particles. But extra parton emissions can also happen from the initial-state partons, occurring before the hard

process. Technically, the parton-shower evolution is performed starting with the hard process and then gradually going backwards in time and adding further emissions to the current initial-state particle, again going from large angles to small angles. As the extra emission requires more energy to be extracted from the parton, an extra factor, the corresponding ratio of the PDFs, appears in the Sudakov form factor, such that it reads

$$\Delta_i(\theta_1, \theta_2, x) = \exp \left( - \sum_j \int_{\theta_2^2}^{\theta_1^2} \frac{d\tilde{\theta}^2}{\tilde{\theta}^2} \int_{z_-(\tilde{\theta})}^{z_+(\tilde{\theta})} dz \frac{x}{z} \frac{f_j(\frac{x}{z}, q^2)}{x f_i(x, q^2)} \frac{\alpha_s}{2\pi} P_{ij}(z) \right), \quad (50)$$

with proton momentum fraction  $x$  as an extra argument and  $q^2$  is the extraction scale corresponding to the angle  $\theta_2$ . Any radiation generated as such will then of course also undergo the normal final-state shower discussed before.

Soft emission already factorizes on the amplitude level. This also means that these emissions appear equally well for interference terms and one cannot interpret the results in terms of individual Feynman diagrams. The corresponding emission cross section of a soft gluon with four-momentum  $q$  in solid angle  $\Omega$  can be written as

$$d\sigma = d\sigma_B \frac{dq_0}{q_0} d\Omega \frac{2\pi \alpha_s}{2\pi} \sum_{i,j} C_{ij} q_0^2 \frac{p_i \cdot p_j}{(p_i \cdot q)(p_j \cdot q)}, \quad (51)$$

where the sum is over all pairs  $(i, j)$  of colored external particles and  $C_{ij}$  is their color factor,  $C_F$  for a quark or anti-quark emitter,  $C_A$  for a gluon emitter splitting into a quark pair, and  $C_A/2$  for a gluon splitting into gluons, where the additional factor accounts for the symmetry that either emitted gluon can be soft. From this expression one can deduce that after azimuthal averaging the emission of wide-angle soft gluons predominantly takes place within a cone spanned by the two emitting particles.

## 2. Combining Parton Shower and NLO Calculations

So far, we have discussed adding parton showers on top of Born-level cross section calculations. For fixed-order, NLO accuracy can be seen as more or less standard nowadays, so the next step is to discuss the necessary modifications when adding parton showers to NLO cross sections instead.

As we have seen in the previous section, the parton shower generates extra emissions of final-state partons, which are subsequently smaller in the ordering parameter, which we have taken as  $\theta$ . The real-emission part of our NLO calculation, however, also contains already one extra emission compared to the Born process. In order to obtain a reasonable prediction, this has to be taken into account to avoid double-counting. This procedure is also known under the term of matching NLO calculations with parton showers.

In the previous chapter, we have discussed the individual pieces entering an NLO calculation, with the final expression given by eq. (41). We now come back to this, but rewrite it slightly for the following discussion, considering its effect on an observable  $\mathcal{O}$ , such that  $\langle \mathcal{O} \rangle_{\text{LO}} = B\mathcal{O}(0)$ . Then we obtain

$$\langle \mathcal{O} \rangle_{\text{NLO}} = B\mathcal{O}(0) + \left( V + \int dx D(x) \right) \mathcal{O}(0) + \int_0^1 dx (R(x)\mathcal{O}(x) - D(x)\mathcal{O}(0)). \quad (52)$$

The first term is the Born contribution, the second one the virtual part with the integrated dipoles added to yield an infrared-finite result, and the last term is the real-emission contribution from which the dipole terms are subtracted. The variable  $x \in [0; 1]$ , which also is the argument of  $\mathcal{O}$ , denotes the phase space of the extra emission in a symbolic notation. In the limit  $x \rightarrow 0$ , it approaches the Born phase space. As the dipole subtraction terms are evaluated with the corresponding tilde kinematics, the observable is hence evaluated at  $x = 0$ .

The Sudakov form factor, eq. (49), can be expressed in the following schematic form with the splitting function  $P(x)$

$$\Delta(x) = \exp\left(-\int_{\mu}^x dx' P(x')\right) \simeq 1 - \int_{\mu}^x dx' P(x'). \quad (53)$$

The parameter  $\mu$  is the lower cutoff, where extra emissions are not resolved explicitly anymore, and on the right-hand the expression has been expanded up to the NLO order, as  $P(x)$  contains an implicit factor of  $\alpha_s$ . As the next step we now apply the parton shower to the Born and consider up to one extra emission only. Then for the observable it follows that

$$\langle \mathcal{O} \rangle_{\text{PS}, \leq 1 \text{ emission}} = B\mathcal{O}(0)\Delta(1) + \int_{\mu}^1 dx B\mathcal{O}(x)P(x) \frac{\Delta(1)}{\Delta(x)}. \quad (54)$$

The first term describes the no-emission contribution and gets weighted by the Sudakov factor, while the second term has one emission at  $x$ , giving the factor  $P(x)$ , and the lower bound of the integral in the Sudakov factor becomes  $x$ , which can be formally also written as the ratio of Sudakov factors in the expression above. The expansion of the Sudakov factors in eq. (54), dropping all terms higher than NLO in  $\alpha_s$ , yields

$$\langle \mathcal{O} \rangle_{\text{PS}, \leq 1 \text{ emission}} = B\mathcal{O}(0) \left(1 - \int_{\mu}^1 dx P(x)\right) + \int_{\mu}^1 dx B\mathcal{O}(x)P(x). \quad (55)$$

This expression can now be inserted in our NLO cross section, eq. (52), again dropping terms which are beyond the NLO level,

$$\begin{aligned} \langle \mathcal{O} \rangle_{\text{NLO}+1 \text{ emission}} &= B\mathcal{O}(0) + \left(V + \int dx D(x)\right) \mathcal{O}(0) \\ &+ \int_0^1 dx (R(x)\mathcal{O}(x) - D(x)\mathcal{O}(0)) \\ &- B\mathcal{O}(0) \int_{\mu}^1 dx P(x) + \int_{\mu}^1 dx B\mathcal{O}(x)P(x). \end{aligned} \quad (56)$$

The first emission of the parton shower has generated the last two extra terms. However, one condition of our parton shower was unitarity, i.e. the total effect, integrating out any extra emissions generated, should vanish. Therefore, these two terms are exactly the double-counting effect which has been mentioned in the introduction, and these must be subtracted from the NLO cross section before applying the parton shower. Hence, the expression reads

$$\begin{aligned} \langle \mathcal{O} \rangle_{\text{NLO,PS}} &= \left(B + \left(V + \int dx D(x)\right) + \int_0^1 dx (B \cdot P(x) - D(x))\right) \mathcal{O}(0) \\ &+ \int_0^1 dx (R(x) - B \cdot P(x)) \mathcal{O}(x). \end{aligned} \quad (57)$$

Here we have used the fact that the splitting kernel times the Born also approaches the real-emission matrix element in the singular limits, and therefore both parts are regularized.

In eq. (57) we still have the freedom of how to exactly choose the splitting kernels. The only relevant property is that in the soft or collinear limit, the correct form of the divergence is reproduced, but the finite terms away from this limit can in principle be chosen arbitrary. The most obvious possibility is to take the DGLAP splitting kernels, which are also used in the parton shower. This scheme is known as the MC@NLO method [11], or subtractive matching. The second term of eq. (57) contains the difference  $R(x) - B \cdot P(x)$ . This expression is only guaranteed to be positive when evaluated as part of a physical observable, as it appears as result on the left-hand side of the equation. Individual events can however have negative weights, and these are indeed observed in physics calculations. Their effect is balanced by corresponding events with positive weight which enter the same histogram bin, thus giving an overall positive result.

An alternative approach, which has been specifically designed to circumvent the negative-weights issue, is the POWHEG (POSitive Weight Hard Emission Generator) [8, 9] method. Here, the splitting kernel is chosen as

$$P(x)_{\text{POWHEG}} = \frac{R(x)}{B}, \quad (58)$$

the ratio of real-emission over Born matrix element. This gives a very simple expression for eq. (57), as the last term just drops out. The parton shower input now only consists of events with Born kinematics. But this simplicity at the level of the matrix elements comes with a price for the parton shower. The splitting kernel in the Sudakov form factor, which governs the appearance of extra emissions, now contains the full real-emission matrix element. This is except for very simple cases known numerically only and takes a noticeable amount of time to evaluate. Hence, the actual parton shower generation is much more complicated. A way out of this is to consider the first emission separately from subsequent ones. For the first one,  $P(x)_{\text{POWHEG}}$  is used, so that subtracting the double-counting does not introduce negative weights. For the subsequent emissions then only the simpler standard splitting kernels of the parton shower are used. The difference between the two is of higher order and therefore the two approaches are equivalent up to the next-to-leading order considered here.

Also, in the POWHEG approach the Sudakov form factor takes a special ordering variable, namely the transverse momentum, so that it reads in the symbolic form

$$\Delta_{\text{POWHEG}} = \exp \left( - \int_{\mu}^x dx' \frac{R(x')}{B} \Theta(p_T(x) - p_T) \right). \quad (59)$$

This makes the POWHEG-generated emission the hardest emission in the process. In the subsequent parton shower this ordering has to be respected as well. For parton showers which are ordered in transverse momentum, this poses no problem, as one can simply choose the appropriate  $p_T$  as the starting scale. For angular-ordered showers, like the default shower of Herwig, this is however not the case. The hardest emission generated by the parton shower will occur somewhere in the middle of the sequence. To preserve the approximate color structure of the emissions, we need to keep the ordering of the emissions. Therefore, the standard technique in these cases is to split the parton shower into two separate parts. First one generates the soft, wide-angle emissions before the hardest one and stops the parton shower at that value of the evolution variable where the emission of the POWHEG-generated one takes place in the ordered sequence. This restriction of the parton shower

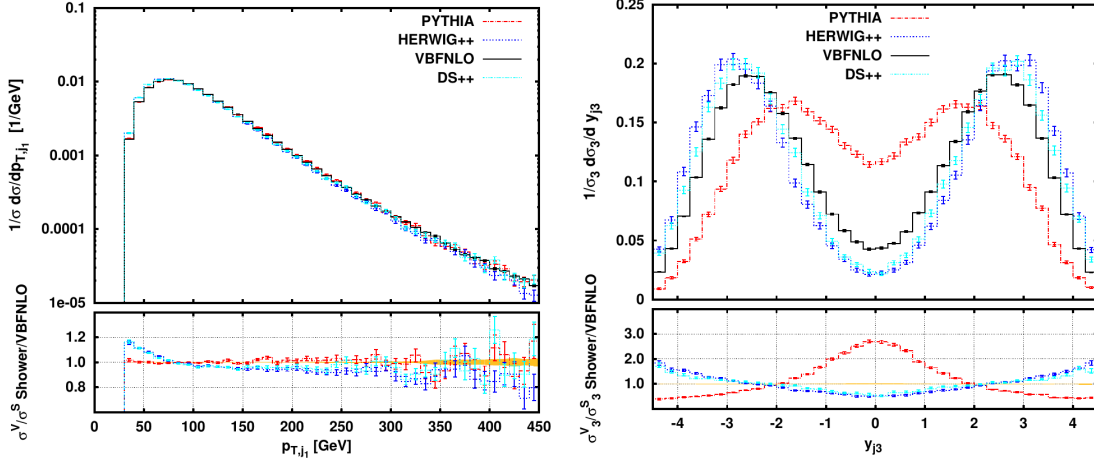


FIG. 14. Normalized differential distributions of the transverse momentum of the leading jet (*left*) and the rapidity of the third jet (*right*) in VBF- $H$  production. Shown are distributions for LO calculated with VBFNLO (using electroweak  $H + 3$  jets production for the right plot) and LO plus three different parton showers. The lower ratio plot is normalized to the respective LO cross section. Error bands and bars are statistical only. Figure taken from Ref. [31].

is known under the name truncated shower. Then the parton shower is run again with the POWHEG-generated emission as starting one, and any harder emissions which might appear afterwards are vetoed. Hence this restriction is also called a vetoed shower. The application of both is necessary to obtain correct results [118].

A third possibility, which has appeared in recent years [119–124], uses the subtraction dipoles of the NLO calculation as splitting kernel, i.e.  $P_{\text{subtr}}(x) = \frac{D(x)}{B}$ . Looking at eq. (57), we see that the matching becomes particularly easy, as the only necessary ingredients are known from the fixed-order NLO calculation anyway. Plugging  $P_{\text{subtr}}(x)$  in, we see that the only difference is the evaluation of  $\mathcal{O}$  for the real-emission dipole. Instead of the Born-type tilde kinematics, it is now calculated at the corresponding real-emission phase-space point. Since the subtraction dipoles are known analytically, building a corresponding parton shower out of them becomes a feasible task.

Parton showers in general resum the leading logarithmic terms and the leading-color part of the next-to-leading logarithmic terms. This level of accuracy is sufficient to combine them with LO and NLO calculations of the hard matrix element.

## B. Applying Parton Showers to LO VBF Processes

Having discussed the general basics of parton shower algorithms, we can now apply them to the VBF processes. In this section we will shortly discuss the combination of LO calculations and parton shower, before turning to the NLO case in the next section. As the aim of this part is mainly to motivate some discussions of special features in the next one, we will restrict ourselves to considering VBF- $H$  production as a simple example.

In Fig. 14, taken from Ref.[31], we show in the left panel the transverse momentum distribution of the leading jet. The black LO curve has been generated with VBFNLO [27–

29] and is labeled as such. Additionally, three different parton showers have been applied on top of this. They are Pythia 6.4.25 [112] with the Perugia 0-tune [105] in red, which is a  $p_T$ -ordered shower, the angular-ordered default shower of Herwig++ 2.7.0 [110] in blue, and the  $p_T$ -ordered dipole shower [122] of Herwig++ in cyan, labeled as DS++ here. We note that the angular-ordered shower of Herwig++ does not implement truncation, so some soft, wide-angle radiation is not present there. The comparison with the dipole shower allows for an estimate of the importance of these contributions which, as we will see, turns out to be negligible. Each curve in the distribution is normalized to its respective integrated cross section. The lower panel contains the ratio of the showered samples to the LO one. The bands and error bars are statistical. Standard VBF cuts have been used for the generation, namely

$$\begin{aligned}
 p_{T,j,\text{tag}} > 30 \text{ GeV}, & & p_{T,j,\text{other}} > 20 \text{ GeV}, & & |y_j| < 4.5, \\
 m_{jj,\text{tag}} > 600 \text{ GeV}, & & \Delta y_{jj,\text{tag}} > 4, & & y_{j_1} \cdot y_{j_2} < 0.
 \end{aligned}
 \tag{60}$$

For the showered samples, looser generation cuts have been used to allow for migration effects. We observe that the Pythia shower induces almost no shape changes to this distribution. For the two Herwig++ showers, the distribution is shifted towards smaller values of the leading-jet transverse momentum. This is in accordance with the corresponding NLO distribution (not shown), which generates a similar shift.

In the right panel of Fig. 14, we show the rapidity distribution of the third jet. This one is generated purely by the respective parton shower. For the LO curve, we therefore use the prediction for electroweak  $H + 3$  jets production. This rapidity distribution has important applications for the experimental detection of VBF processes as already discussed in section II. The NLO cross section, which is equivalent to the LO electroweak  $Hjjj$ , predicts that also the third jet is generated predominantly in the forward direction, and radiation in the central region is strongly reduced. This is in contrast to QCD-induced production mechanisms, where more jet activity happens in the central region. This can be exploited by applying a central jet veto for VBF processes [30, 125–128]. The additional radiation from the parton shower could however also fill up the central region, thereby invalidating this criterion. The result of Fig. 14 shows a quite different answer to this question depending on which parton shower is used. The Pythia shower predicts that the gap is filled with a significant amount of radiation, more than 2.5 times the value of the LO  $H + 3$  jets cross section at  $y_{j_3} = 0$ . The two Herwig++ showers in contrast exhibit only a very mild jet activity, even slightly below the fixed-order curve. From the parton-shower side, there is no reason to prefer one implementation over the other, as all should be equivalent up to corrections higher than the considered order. Hence, in first approximation one would take the envelope of the predictions as uncertainty on the central jet veto, thus removing any possible discrimination power.

To investigate this issue further, we should combine the NLO prediction with a parton shower. In that way, one gets the correct description of the large transverse-momentum behavior and the correct normalization of the cross section from the fixed-order calculation. The parton shower augments this with the correct description of soft and collinear radiation and the resummation of the leading logarithms.

### C. Parton Showers Matched to NLO VBF Processes

NLO calculations of VBF processes matched to parton showers have been first presented using the POWHEG-BOX framework [8–10]. Results can also be obtained nowadays using the available automated frameworks, e.g. via Sherpa [113], with generating events by MadGraph5\_aMC@NLO [43] and feeding them through a parton-shower and hadronization program, or from Herwig 7 [106, 107], obtaining the required amplitudes either from automatic generators like MadGraph5\_aMC@NLO [43] or GoSam [129, 130], or dedicated tools like VBFNLO [27–29] or HJets++ [103] for electroweak Higgs-boson production in association with two or three jets.

#### 1. The POWHEG-BOX Approach

The POWHEG-BOX framework is a semi-automated approach implementing the POWHEG matching scheme. For each process one needs to implement the following ingredients:

- the squared matrix elements for all Born subprocesses,
- the interference between the renormalized virtual amplitude and the Born amplitude with integrated subtraction dipoles in the FKS scheme [71] added,
- the squared matrix elements for all real-emission subprocesses,
- the phase space for the Born kinematics,
- the flavor structure of all Born and real-emission subprocesses,
- the color structure of the Born processes in the limit of a large number of colors.

The framework itself takes care of all other parts, like the steering of the phase-space integration, generating the real-emission phase space with one extra emission, and writing out Les Houches event files [131, 132]. These can then be used as input for a transverse-momentum-ordered or a truncated and vetoed angular-ordered parton shower.

Implementations are available for the VBF production of  $Hjj$  [104],  $W^\pm jj$  [133],  $Zjj$  [133, 134],  $W^+W^-jj$  [135],  $W^\pm W^\pm jj$  [35],  $ZZjj$  [136] and electroweak production of  $Hjjj$  [102].

Coming back to the discussion about additional jet activity in the central region between the two tagging jets, we now look at the corresponding distributions at NLO combined with parton shower accuracy, taking VBF- $W^+jj$ ,  $W^+ \rightarrow \ell^+ \nu_\ell$ ,  $\ell = e, \mu$  as example. In the upper left panel of Fig. 15, taken from Ref. [133], we first show the transverse momentum of the charged lepton as example of a distribution which should receive only mild corrections from the parton shower. From the plot we see that this is indeed the case. The labeling of the curves is similar to Fig. 14. The black NLO curve has been generated with VBFNLO [27–29] and is labeled such. Additionally, three different parton showers have been applied on top of this. They are Pythia 6.4.25 [112] with the Perugia 0-tune [105] in red, which is a  $p_T$ -ordered shower, the angular-ordered default shower of Herwig++ 2.7.0 [110] in blue, and the  $p_T$ -ordered dipole shower [122] of Herwig++ in cyan, labeled as Herwig++ Dipole here. Each curve in the distribution is normalized to its respective integrated cross section. The



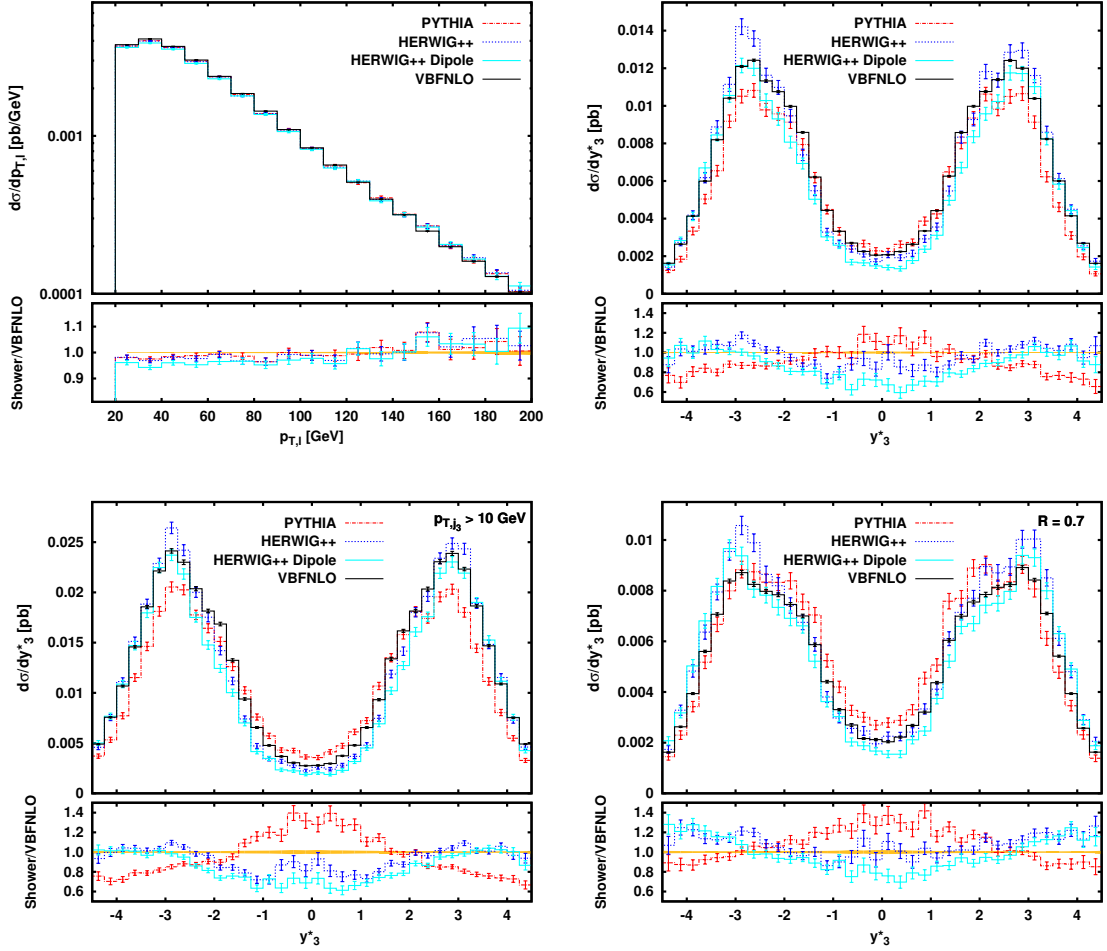


FIG. 15. Differential distributions of the transverse momentum of the charged lepton (*upper left*) and the rapidity of the third jet relative to the average tagging jet position (*upper right and both lower panels*) in VBF- $W^+$  production with leptonic decay. In the lower panels, the  $p_{T,j3}$  cut has been lowered from 20 to 10 GeV (*lower left*), or the jet clustering parameter  $R_{jj}$  increased from 0.5 to 0.7 (*lower right*). Shown are distributions for fixed-order NLO calculated with VBFNLO and NLO plus three different parton showers using the POWHEG matching scheme. The lower ratio plot is normalized to the fixed-order NLO cross section. Error bands and bars are statistical only. Figure taken from Ref. [133].

lower panel contains the ratio of the showered samples to the NLO one. The bands and error bars are statistical. Cuts are as in eq. (60), with additionally requiring for the lepton

$$\begin{aligned}
 p_{T,\ell} &> 20 \text{ GeV}, & |y_\ell| &< 2.5, \\
 \Delta R_{j\ell} &> 0.4, & y_{j,\text{tag}}^{\min} &< y_\ell < y_{j,\text{tag}}^{\max}.
 \end{aligned}
 \tag{61}$$

From the ratio plot in the lower part we see that the parton-shower results exhibit a slightly larger cross section for larger transverse momentum. This can be easily understood from additional initial-state radiation, which then gives a transverse momentum boost to the hard process. As the cross section is falling with larger transverse momenta, migration

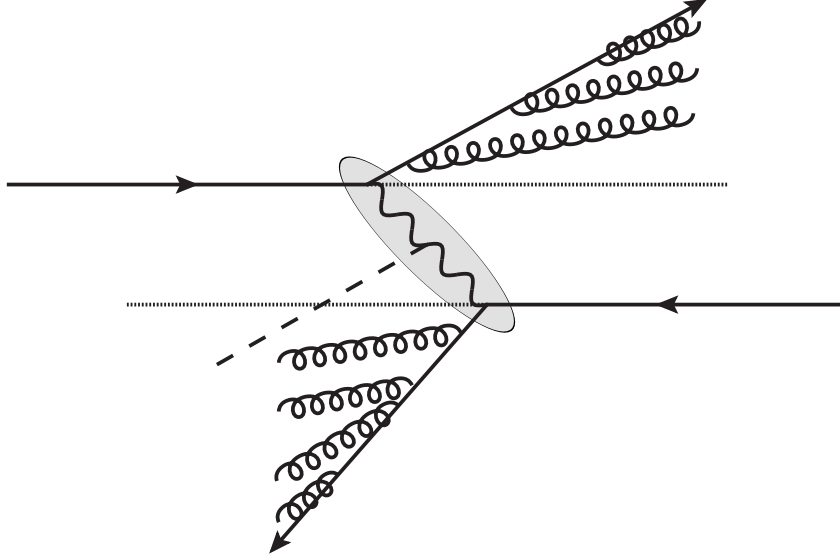


FIG. 16. Schematic picture of additional radiation generated by parton showers for VBF processes.

effects towards larger values dominate over those to smaller values and thus increase the differential cross section there. Unitarity of the parton shower then leads to the observed decrease for small transverse momenta.

The upper right plot of Fig. 15 shows the rapidity of the third jet relative to the two tagging jets, using the variable  $y_{j,3}^*$  defined in eq. (5). Overall, the agreement between the fixed-order result and the parton-shower ones is much better than for LO, as the parton-shower results get corrected by the  $W + 3$  jet matrix element, which enters through the real-emission part of the NLO process. Significant differences between the parton-shower results are nevertheless still present. In the central region, the Pythia shower predicts a differential cross section enhanced by about 10% compared to the NLO one. The two Herwig++ showers in contrast show a reduction, in the case of the dipole shower up to 30%. The behavior gets reversed when looking at the regions further forward than the tagging jets at around  $\pm 2.7$ . There the two Herwig++ showers hardly modify the NLO result, while Pythia exhibits significantly lower values. The difference becomes even more pronounced when lowering the minimum transverse momentum cut of the third jet to 10 GeV (lower left panel of Fig. 15) or increasing the jet clustering parameter  $R_{jj}$  to 0.7 (lower right panel).

Let us consider again the color structure of VBF processes. The exchange of a color-singlet electroweak boson between the two quark lines means that in the hard process color connections only exist between the parton forming a tagging jet and its corresponding initial-state parton connected by a fermion line. Going to a pure final-state picture, the conjugate color charge of the initial-state parton is carried by the proton remnant moving along the beam line. Hence, we expect that color correlations should enhance additional radiation between the tagging jet and the corresponding positive or negative  $z$ -axis, but not in the central region. A schematic picture is shown in Fig. 16.

Pythia tends to generate more additional soft partons in the central region than the two Herwig++ showers, which emit more into the forward regions. Therefore, for the Herwig++ showers the jet clustering algorithm mostly picks up additional radiation from the forward region and hence the jet moves in that direction, while for Pythia the enhanced central-region

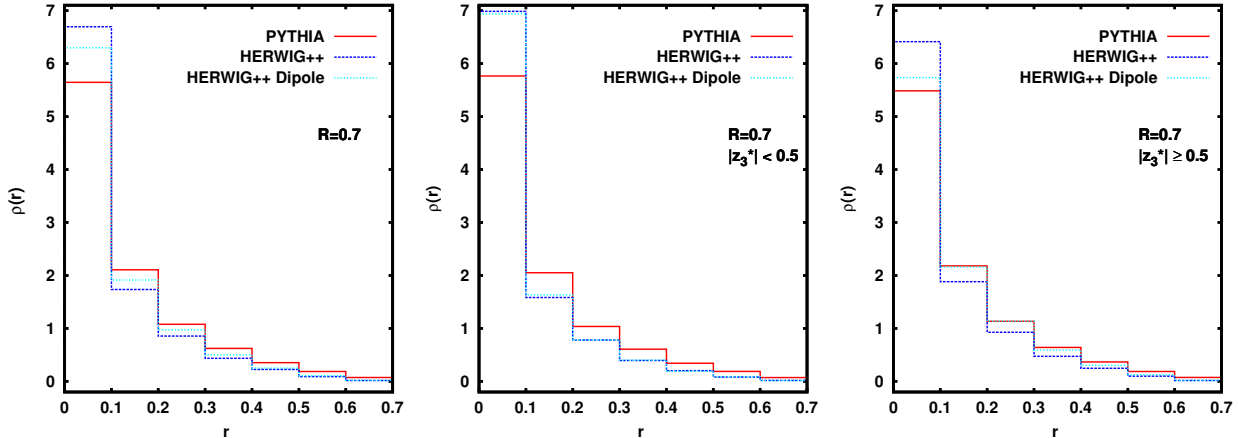


FIG. 17. Differential jet shape distribution  $\rho(r)$  for  $R_{jj} = 0.7$ , for the full phase-space region (*left*), and separated into the central region between the two tagging jets (*center*) and the forward regions outside the tagging jets (*right*). Figure taken from Ref. [133].

radiation pulls the jet there.

One can also look at the differential shape of the third jet, defined as [133, 137, 138]

$$\rho(r) = \frac{1}{\Delta r} \sum_{\substack{\text{parton} \in j_3 \\ r_{\text{parton}} \in [r - \frac{\Delta r}{2}, r + \frac{\Delta r}{2}]}} \frac{p_{T,\text{parton}}}{p_{T,j_3}}, \quad (62)$$

where  $r$  denotes the  $R$  separation from the center of the third jet. Its value can range from  $\frac{\Delta r}{2}$  to  $R_{jj} - \frac{\Delta r}{2}$ . For the calculation of  $\rho(r)$ , all partons belonging to the third jet within a cone from  $r - \frac{\Delta r}{2}$  to  $r + \frac{\Delta r}{2}$  are used. The formula above automatically yields the normalization  $\int_0^{R_{jj}} dr \rho(r) = 1$ .

In Fig. 17 we show the distribution of this variable, using  $\Delta r = 0.1$ . The left panel shows this variable plotted over the whole phase space after cuts. We observe that Pythia generates much wider jets than the two Herwig++ showers. The density  $\rho(r)$  for  $r > 0.1$  is considerably enhanced. This behavior is even more pronounced when considering only jets which are located between the two tagging jets in rapidity, shown in the center panel of Fig. 17. The selection is done by requiring  $|z_{j_3}^*| < 0.5$ , with  $|z_{j_3}^*|$  defined in eq. (6). For third jets in the forward region on the other hand (right panel), the distributions differ less, with the Herwig++ dipole shower almost equaling the Pythia results. The reason for the observed differences is the already mentioned generation of more soft, wide-angle radiation in Pythia. Collinear radiation happens predominantly close to the emitting parton, so for small values of  $r$ , while soft emission is less correlated to it and leads equally well to jet contributions at larger  $r$  values. This can also explain the broader jets of the Herwig++ dipole shower compared to the default shower in the forward region, as a lower IR cutoff of the Sudakov form factor generates more soft radiation.

When considering distributions of the third jet in VBF processes, the corresponding matrix elements are those of the real-emission process and hence of LO accuracy only. To study these distributions at NLO accuracy, one needs to consider electroweak production in association with three jets. In Ref. [102], this task has been performed for electroweak Higgs

plus three jets production using again the POWHEG method, again comparing Pythia and the two showers available in Herwig++ 2.7.0. The rapidity distribution of the third jet shows good agreement between the showered and the fixed-order NLO results. As before, Pythia predicts slightly more radiation in the central region, while the two Herwig++ showers show a mild increase in the forward region. Larger differences then again occur for rapidity distributions of further jets which are corrected by LO matrix elements only (fourth jet) or originate purely from the parton shower (fifth and higher jets).

## 2. Shower Uncertainties

The existence of different parton-shower approaches and different matching methods allows for comparing the results between them. Possible deviations are formally effects of higher order, and so the envelope of the predictions can also serve as an estimate for the impact of these corrections. A study for VBF- $H$  production, comparing the MC@NLO and POWHEG matching schemes as well as changes in the factorization and renormalization scheme, has been performed in Ref. [139].

In the following, we will consider the VBF production process  $pp \rightarrow e^+ \nu_e \mu^- \bar{\nu}_\mu jj$  to study shower uncertainties [140]. All results have been generated with Herwig 7 [106, 107] using VBFNLO [27–29]. Cuts are imposed as follows

$$\begin{aligned}
 p_{T,j} &> 30 \text{ GeV}, & |y_j| &< 4.5, \\
 p_{T,\ell} &> 20 \text{ GeV}, & |y_\ell| &< 2.5, \\
 m_{j_1,j_2} &> 600 \text{ GeV}, & |y_{j_1} - y_{j_2}| &> 3.6,
 \end{aligned} \tag{63}$$

where partons are clustered into jets with the anti- $k_T$  algorithm [78, 79] using an  $R$  separation parameter of 0.4. The central value for the factorization, renormalization and shower-starting scale is taken as the transverse momentum of the leading jet,  $\mu_0 = p_{T,j_1}$ .

In Fig. 18 we show the invariant mass distribution of the four final-state leptons. This variable is expected to be rather insensitive to parton-shower effects. The upper panel shows differential cross sections for various combinations of fixed-order result and parton shower. The black line denotes the fixed-order NLO QCD result without any parton shower attached, the two blue lines employ the dipole shower, where the brighter line shows the combination with the LO result and the darker one with the NLO result, and the red line depicts the NLO plus angular-ordered shower result. The matching is performed using the MC@NLO-type, subtractive scheme in both cases. In all cases, the distribution clearly shows the Higgs peak at 125 GeV, followed by the continuum production of two on-shell  $W$  bosons starting around the  $2M_W$  threshold. The second panel depicts the ratio of the different cross sections over the fixed-order NLO result, given by the solid lines. The shaded area describes the scale variation band, which we will explain afterwards. As one can see from the figure, the fixed-order NLO QCD curve yields the largest cross section, and all parton-shower results are smaller by a factor which is approximately constant over the invariant mass. The reason for this is an effect we have already seen when discussing the NNLO QCD corrections. The parton shower generates additional splittings of final-state partons. If these are wide-angle and hard enough, they will not be clustered into the same jet as the original parton, but form a separate jet. Hence, the energy of the two leading jets gets decreased and its invariant mass becomes smaller. Thus this VBF cut removes a fraction of the events and the cross section becomes smaller. For the LO curve, the larger strong coupling constant increases the parton

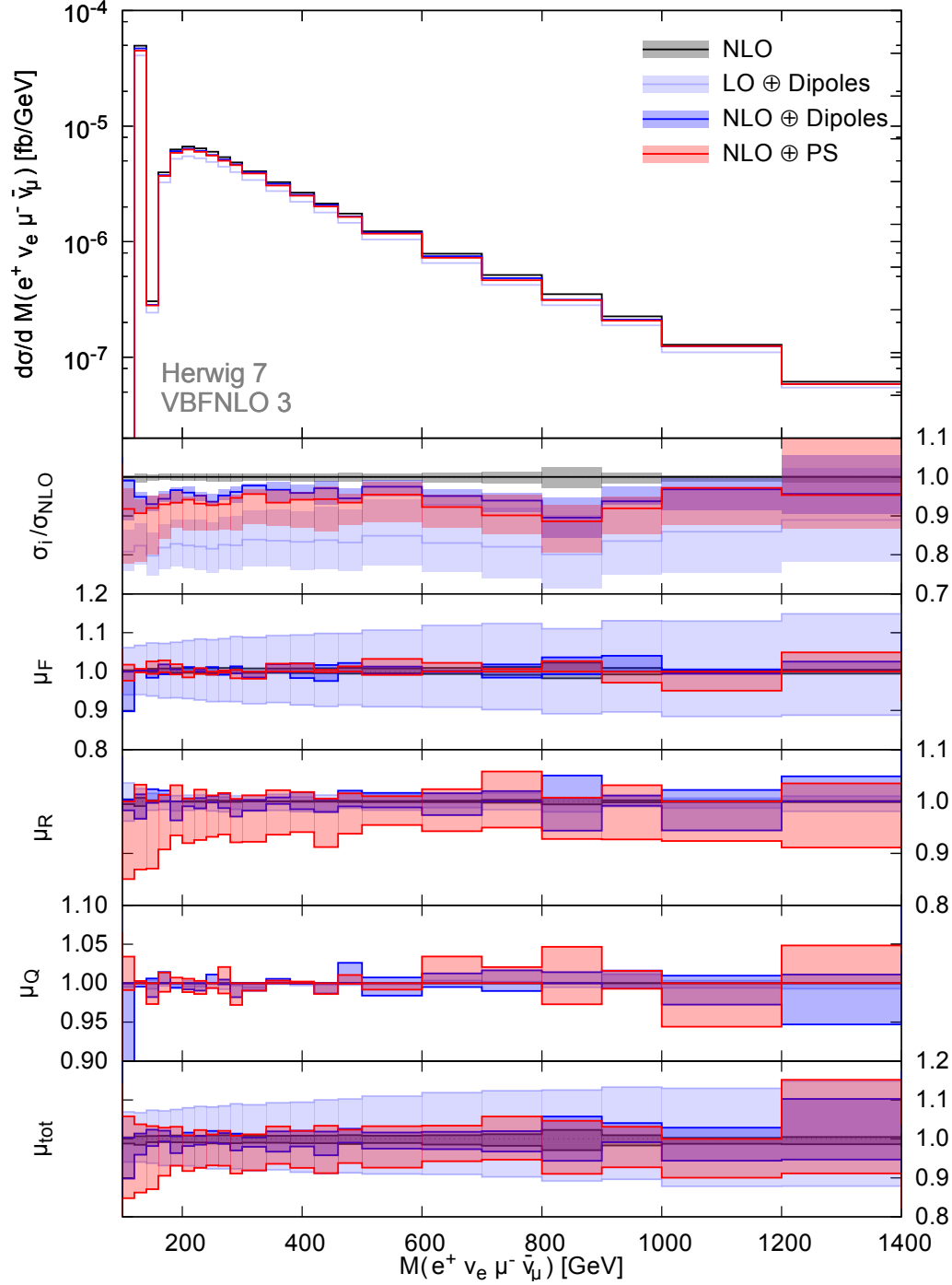


FIG. 18. Invariant mass distribution of the four leptons in  $e^+ \nu_e \mu^- \bar{\nu}_\mu jj$  production via VBF. The upper panel shows the differential cross section for various combinations of fixed-order result and parton shower. The four lowest panels show the uncertainty band when varying the factorization scale  $\mu_F$ , renormalization scale  $\mu_R$ , shower scale  $\mu_Q$ , and all three  $\mu_{\text{tot}}$  by a factor  $2^{\pm 1}$  around the central scale  $\mu_0 = p_{T,j1}$ . The second uppermost panel shows the ratio of each cross section over the fixed-order NLO result, with the band given by the envelope of all scale variations as in the lowest panel. Figure taken from Ref. [140].

splitting probability and so the drop in cross section is stronger than for the other results. The four lower panels show scale uncertainty bands, individually normalized to the central results. Varied are, from top to bottom, the factorization scale  $\mu_F$ , the renormalization scale  $\mu_R$ , the starting scale of the shower  $\mu_Q$ , and all three at the same time, labeled  $\mu_{\text{tot}}$ . For the individual scale variations, these are probed by changing each scale by a factor  $2^{\pm 1}$  from the central scale  $\mu_0$ . For the joint case, all scales are allowed to vary separately, but the ratio of any two scales must be within the range  $[0.5; 2]$ . So if any of the scales is varied upwards, none of the others can fluctuate downwards and vice versa. The result of varying all scales in this way is also depicted as the band shown in the ratio panel. Both factorization and renormalization scale are varied consistently in the hard process and the parton shower, changing all occurrences simultaneously. We see from the figure that the scale variation behavior is dominated by the fixed-order part. The total LO variation is dominated by the effect of changing the factorization scale and leads to an uncertainty band of about 10%, while the renormalization scale enters through the shower only and yields small effects. The dependence on the shower scale is rather small in all cases. From the ratio plot we also see that the bands of the fixed-order NLO result, the NLO result matched with the dipole shower and the LO plus dipole shower are all non-overlapping. Simple scale variation thus tends to underestimate these migration effects.

In Fig. 19 we present results for the variable  $y_3^*$ , the rapidity of the third jet relative to the averaged rapidities of the two tagging jets, which has been defined in eq. (5). This variable plays an important role for VBF processes, as a veto on additional jets in the central region allows to reduce QCD-induced background processes. The differential cross section in the upper panel of the figure shows the same picture we have already seen during the discussion of the POWHEG-BOX results. At large absolute values of the observable, the results of the fixed-order calculation and the parton-shower ones agree well. In the central region, the situation looks different. Here much less radiation than at NLO is predicted. This is particularly striking for the LO plus dipole shower curve, where the differential cross section in the two central bins is only 20% of the NLO number. In this case the third jet originates purely from partons generated by the shower, and radiation is in general too soft to produce sufficient jet activity. An indication for problematic behavior can be seen in the large uncertainties when varying the shower scale, though the resulting band is not wide enough to reach the NLO-matched results. There, corrections from the hard matrix element increase the cross section and stabilize the prediction. The uncertainty from varying the shower scale now becomes small and no longer shows an increase in the central region, but is rather flat over the whole range. No relevant difference between the results using the dipole shower and those with the angular-ordered shower can be observed.

In Fig. 20 we compare the effects of the two matching schemes on  $y_3^*$ . The cyan curve shows results using multiplicative, POWHEG-type matching, The blue curve using subtractive, MC@NLO-type matching and the black fixed-order NLO curve are the same as in Fig. 19. As parton shower we use in both cases the dipole shower. The upper panel shows the differential cross section, and the lower one the ratio over the fixed-order NLO result. The scale variation bands there are obtained by varying the factorization, renormalization and, in case of the matched cross sections, the shower scale jointly by a factor  $2^{\pm 1}$ . We observe that there is in general a good agreement between the results of the two matching schemes. For the integrated cross section, the POWHEG result is closer to the NLO result, which originated mostly from the region where the rapidity of the third jet is close to one of the two tagging jets, i.e. the peak region of the distribution. For the phenomenologically

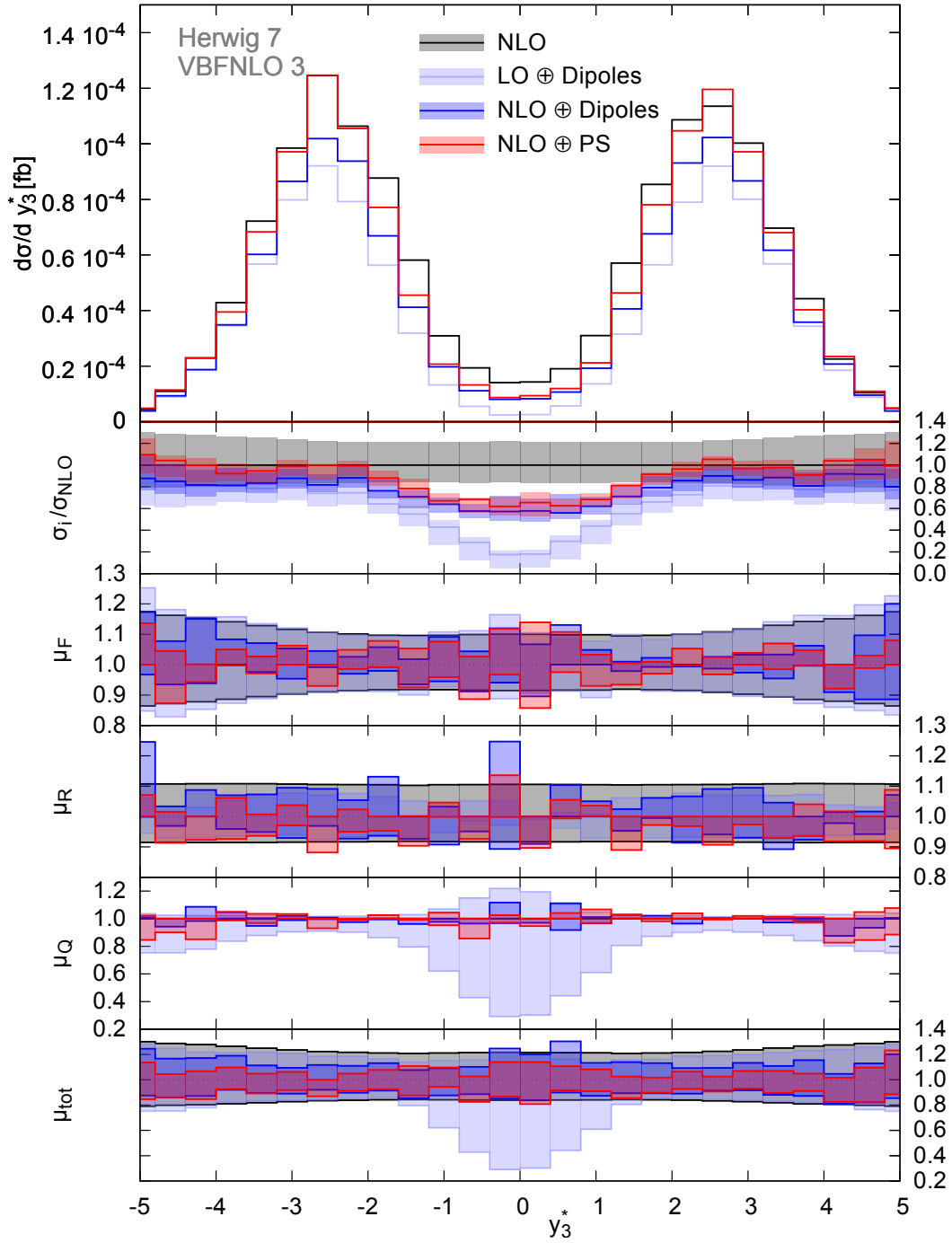


FIG. 19. Rapidity distribution of the third jet relative to the two tagging jets in  $e^+\nu_e\mu^-\bar{\nu}_\mu jj$  production via VBF. Curves and quantities plotted are as in Fig. 18. Figure taken from Ref. [140].

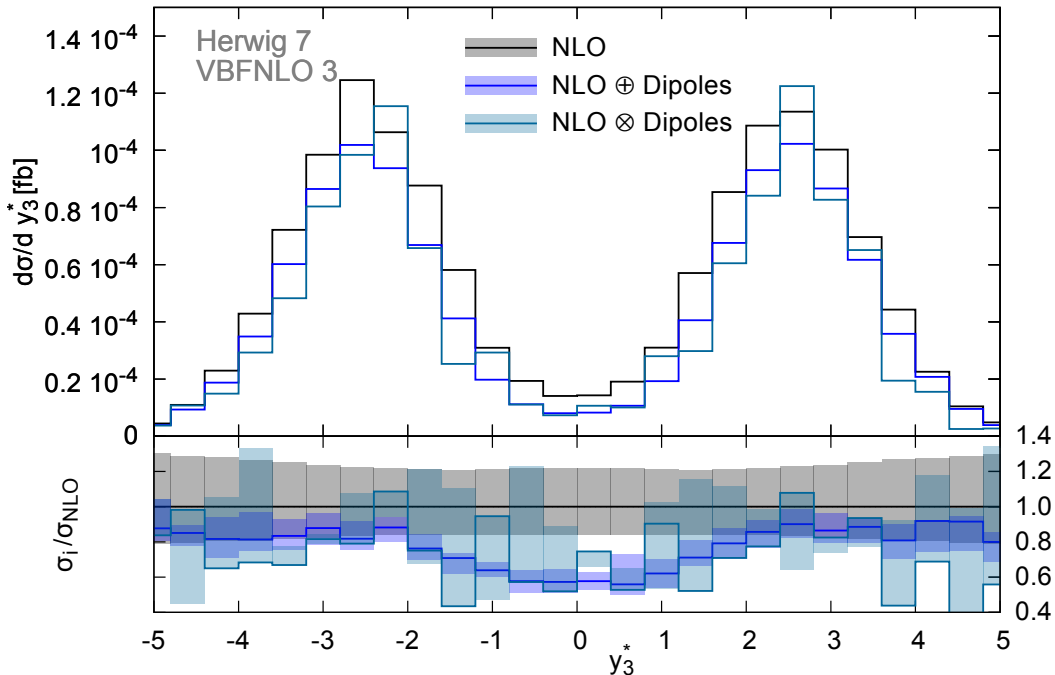


FIG. 20. Rapidity distribution of the third jet relative to the two tagging jets in  $e^+\nu_e\mu^-\bar{\nu}_\mu jj$  production via VBF. The upper panel shows the differential cross section for the fixed-order NLO calculation and combined with the dipole shower using subtractive MC@NLO-type (“ $\oplus$ ”), and multiplicative POWHEG-type (“ $\otimes$ ”) matching. The lower panel depicts the ratio of the differential cross sections over the NLO one. The bands denote the scale uncertainty band of the respective cross section, obtained by varying the factorization, renormalization and shower-scale uncertainty by a factor  $2^{\pm 1}$  around the central scale  $\mu_0$ . Figure taken from Ref. [140].

interesting central region, where the third jet has  $y_3^* = 0$ , the suppression of the cross section seen for MC@NLO-type matching is equally present for POWHEG-type matching. Barring statistical fluctuations from finite Monte-Carlo statistics, the two results are almost on top of each other. The uncertainty band of the POWHEG result is thereby a bit larger. In total, the parton-shower prediction for this observable is insensitive to the details of the matching procedure or the exact shower algorithm. Therefore, it can serve as a useful tool to reduce the contribution of background processes.

## V. ANOMALOUS COUPLING EFFECTS

Having discussed the SM predictions for VBF in the previous chapters, we now turn to new-physics effects appearing in this process class which preserve the underlying symmetries of the SM. VBF processes contain triple (TGCs) and quartic gauge couplings (QGCs). So they are an ideal tool to study these couplings and look for possible deviations from the SM prediction.



## A. Effective Field Theories

A convenient tool to study new-physics effects at high energies in a model-independent way are effective field theories (EFTs). They are based on the following expansion of the EFT Lagrangian

$$\mathcal{L}_{\text{EFT}} = \mathcal{L}_{\text{SM}} + \sum_{d>4} \sum_i \frac{f_i^{(d)}}{\Lambda^{d-4}} \mathcal{O}_i^{(d)}, \quad (64)$$

where  $\Lambda$  is the typical scale of new physics.  $f_i^{(d)}$  are the dimensionless coupling-strength coefficients which are typically of  $\mathcal{O}(1)$ . If the underlying theory is known or presumed to be loop-induced, it can be convenient to pull out an additional explicit loop factor like  $\frac{1}{16\pi^2}$  in the expansion. The operators  $\mathcal{O}_i^{(d)}$  are invariant under the symmetries of the SM. Additionally, different combinations of operators can be related and lead to the same effects on physical observables. To find a minimal set, one uses the equations of motions for the fields and the fact that adding a total derivative to the Lagrangian does not change the theoretical predictions..

When  $\Lambda$  is larger than the energy scales  $E$  of our process, higher orders in the expansion are suppressed by additional powers of  $\frac{E}{\Lambda}$  and it is sufficient to take the leading, lowest-order term of the expansion. Once this truncation has been performed, only a finite number of operators contributes and the theory becomes predictive. It is however important to keep in mind that after truncation the expansion is valid only below the scale of new physics.

The operators are constructed out of the following building blocks:

- Higgs doublet field  $\Phi$ ,
- covariant derivative  $D^\mu$ , which reduces to  $\partial^\mu$  for singlet fields,
- field strength tensors  $G^{a,\mu\nu}$ ,  $W^{i,\mu\nu}$ ,  $B^{\mu\nu}$ ,
- fermion fields  $\psi$ .

In lowest dimension,  $d = 5$ , only one operator exists [141], which generates a Majorana mass term for neutrinos and violates lepton-number conservation. In general, all operators with an odd number of dimensions involve fermion fields and lead to lepton or baryon number violation. Therefore, for the electroweak gauge-boson interactions discussed here, we need to consider even dimensions only, starting with  $d = 6$  [142–145].

Before turning to the operators, we first introduce the notation and definitions which will be used in the following. The Higgs doublet field  $\Phi$  in the unitary gauge is given by

$$\Phi = \begin{pmatrix} 0 \\ \frac{1}{\sqrt{2}}(v + H) \end{pmatrix}. \quad (65)$$

The covariant derivative acting on it is defined as

$$D_\mu = \partial_\mu + ig \frac{\sigma^j}{2} W_\mu^j + ig' \frac{Y}{2} B_\mu, \quad (66)$$

where  $\frac{\sigma^j}{2}$  are the  $SU(2)$  generators with the Pauli matrices  $\sigma^j$  and  $Y$  is the hypercharge of the field on which the derivative acts. For the operators discussed here, this will always be

the Higgs field with  $Y = 1$ .  $g$  and  $g'$  denote the  $SU(2)$  and  $U(1)$  gauge couplings, which are related to the electromagnetic coupling  $e = g s_w = g' c_w$  via sine  $s_w$  and cosine  $c_w$  of the weak mixing angle, respectively.

The modified field strength tensors

$$\begin{aligned}\widehat{W}^{\mu\nu} &= ig \frac{\sigma^j}{2} W^{j,\mu\nu} = ig \frac{\sigma^j}{2} (\partial^\mu W^{j,\nu} - \partial^\nu W^{j,\mu} - g \epsilon^{jkl} W^{k,\mu} W^{l,\nu}) , \\ \widehat{B}^{\mu\nu} &= ig' \frac{1}{2} B^{\mu\nu} = ig' \frac{1}{2} (\partial^\mu B^\nu - \partial^\nu B^\mu)\end{aligned}\quad (67)$$

contain an additional prefactor such that [143]

$$[D^\mu, D^\nu] = \widehat{W}^{\mu\nu} + \widehat{B}^{\mu\nu} \quad (68)$$

and they are treated on a more equal footing with the covariant derivative.

The modified dual field-strength tensors are given by

$$\widetilde{W}^{\mu\nu} = \frac{1}{2} \epsilon^{\mu\nu\rho\sigma} \widehat{W}_{\rho\sigma} , \quad \widetilde{B}^{\mu\nu} = \frac{1}{2} \epsilon^{\mu\nu\rho\sigma} \widehat{B}_{\rho\sigma} . \quad (69)$$

Using these definitions, one can construct the following independent CP-conserving  $d = 6$  operators according to Refs. [29, 143, 144, 146],

$$\begin{aligned}\mathcal{O}_{WWW} &= \text{Tr} \left[ \widehat{W}^\mu{}_\nu \widehat{W}^\nu{}_\rho \widehat{W}^\rho{}_\mu \right] , \\ \mathcal{O}_W &= (D_\mu \Phi)^\dagger \widehat{W}^{\mu\nu} (D_\nu \Phi) , \\ \mathcal{O}_B &= (D_\mu \Phi)^\dagger \widehat{B}^{\mu\nu} (D_\nu \Phi) , \\ \mathcal{O}_{WW} &= \Phi^\dagger \widehat{W}_{\mu\nu} \widehat{W}^{\mu\nu} \Phi , \\ \mathcal{O}_{BB} &= \Phi^\dagger \widehat{B}_{\mu\nu} \widehat{B}^{\mu\nu} \Phi , \\ \mathcal{O}_{\phi,2} &= \partial_\mu (\Phi^\dagger \Phi) \partial^\mu (\Phi^\dagger \Phi) .\end{aligned}\quad (70)$$

The last operator  $\mathcal{O}_{\phi,2}$  contains only terms involving Higgs bosons. This includes a term  $v^2 (\partial_\mu H) (\partial^\mu H)$ , which gives a contribution to the kinetic term of the Higgs field. This must be absorbed by a redefinition of the Higgs boson field, thus changing all couplings involving Higgs bosons.

CP-violating operators can be defined analogously by replacing one field-strength tensor by its dual

$$\begin{aligned}\mathcal{O}_{\widetilde{WWW}} &= \text{Tr} \left[ \widetilde{W}^\mu{}_\nu \widetilde{W}^\nu{}_\rho \widetilde{W}^\rho{}_\mu \right] , \\ \mathcal{O}_{\widetilde{W}} &= (D_\mu \Phi)^\dagger \widetilde{W}^{\mu\nu} (D_\nu \Phi) , \\ \mathcal{O}_{\widetilde{B}} &= (D_\mu \Phi)^\dagger \widetilde{B}^{\mu\nu} (D_\nu \Phi) , \\ \mathcal{O}_{\widetilde{WW}} &= \Phi^\dagger \widetilde{W}_{\mu\nu} \widetilde{W}^{\mu\nu} \Phi , \\ \mathcal{O}_{\widetilde{BB}} &= \Phi^\dagger \widetilde{B}_{\mu\nu} \widetilde{B}^{\mu\nu} \Phi ,\end{aligned}\quad (71)$$

which contribute to the triple and quartic vertices of electroweak bosons. Actually, only four of these five operators are linearly independent, as the relation [75, 146]

$$\mathcal{O}_{\widetilde{W}} + \frac{1}{2} \mathcal{O}_{\widetilde{WW}} = \mathcal{O}_{\widetilde{B}} + \frac{1}{2} \mathcal{O}_{\widetilde{BB}} \quad (72)$$

	$\mathcal{O}_{WWW}$	$\mathcal{O}_W$	$\mathcal{O}_B$	$\mathcal{O}_{WW}$	$\mathcal{O}_{BB}$	$\mathcal{O}_{\phi,2}$	$\mathcal{O}_{\widetilde{W}WW}$	$\mathcal{O}_{\widetilde{W}}$	$\mathcal{O}_{\widetilde{B}}$	$\mathcal{O}_{\widetilde{W}W}$	$\mathcal{O}_{\widetilde{B}B}$
$WWZ$	X	X	X				X	X	X		
$WW\gamma$	X	X	X				X	X	X		
$HWW$		X		X		X		X		X	
$HZZ$		X	X	X	X	X		X	X	X	X
$HZ\gamma$		X	X	X	X	(X)		X	X	X	X
$H\gamma\gamma$				X	X	(X)				X	X
$WWWW$	X	X					X				
$WWZZ$	X	X					X				
$WWZ\gamma$	X	X					X				
$WW\gamma\gamma$	X						X				

TABLE III. Vertices induced by each operator are marked with X in the corresponding column. Vertices which are not relevant for three and four gauge boson amplitudes have been omitted. Table adopted from Ref. [146].

allows to eliminate one of them.

As mentioned before, the choice of independent operators is not unique. Additional operators can be constructed, which are also of dimension 6 and invariant under the SM gauge groups. An example for this is the operator

$$\mathcal{O}_{\phi W} = \Phi^\dagger \Phi \text{Tr} \left[ \widehat{W}_{\mu\nu} \widehat{W}^{\mu\nu} \right] \quad (73)$$

of Ref. [146], which is related to  $\mathcal{O}_{WW} = \frac{1}{2} \mathcal{O}_{\phi W}$ .

An overview how the different operators affect the vertices relevant for VBF production processes is given in Table III. For the operator  $\mathcal{O}_{\phi,2}$  the two entries for  $HZ\gamma$  and  $H\gamma\gamma$  are marked in brackets, as this operator does not induce an additional tree-level contribution as in all other cases, but modifies the loop-induced SM contribution through an additional factor on the  $HWW$  and  $Hf\bar{f}$  couplings. One can see that all operators modify three-boson vertices. Therefore, these will also contribute to diboson production processes, which in general show a higher sensitivity due to their larger cross sections, and limits from there need to be taken into account.

As one can see from Table III, all dimension-6 operators which introduce modifications to the QGCs also change the TGCs, and one would expect to see deviations from the SM predictions there first. If we want to consider models where only the quartic couplings are changed, we need to increase the dimension by two and study EFT operators of dimension 8. Such a scenario could be realized with new-physics bosons coupling to the SM gauge bosons. Then contributions to the effective low-energy QGCs contain tree-level diagrams with an exchange of the new particles [147], while for the TGCs only loop-induced diagrams are possible, which are suppressed by an additional loop factor.

One can also see that dimension-8 operators are required for pure modifications of the QGCs from the following argument [146]. The gauge bosons can either originate from a field-strength tensor or from the covariant derivative acting on the Higgs field. Both expression are dimension-2 terms, and the gauge field is accompanied by a partial derivative  $\partial_\mu$  or the

vacuum expectation value  $v$ , respectively. Thus we need four of them for the full operator, ending up with dimension 8.

This also yields a convenient classification mechanism for the dimension-8 operators modifying QGCs by sorting them by the number of covariant derivatives and field-strength tensors. As the number of open Lorentz indices is one and two, respectively, three different possibilities exist [148, 149]. Operators can either contain only covariant derivatives, called scalar,

$$\begin{aligned}
\mathcal{O}_{S,0} &= [(D_\mu \Phi)^\dagger D_\nu \Phi] \times [(D^\mu \Phi)^\dagger D^\nu \Phi] , \\
\mathcal{O}_{S,1} &= [(D_\mu \Phi)^\dagger D^\mu \Phi] \times [(D_\nu \Phi)^\dagger D^\nu \Phi] , \\
\mathcal{O}_{S,2} &= [(D_\mu \Phi)^\dagger D_\nu \Phi] \times [(D^\nu \Phi)^\dagger D^\mu \Phi] ,
\end{aligned} \tag{74}$$

only field-strength tensors, called tensor,

$$\begin{aligned}
\mathcal{O}_{T,0} &= \text{Tr} [\widehat{W}_{\mu\nu} \widehat{W}^{\mu\nu}] \times \text{Tr} [\widehat{W}_{\alpha\beta} \widehat{W}^{\alpha\beta}] , \\
\mathcal{O}_{T,1} &= \text{Tr} [\widehat{W}_{\alpha\nu} \widehat{W}^{\mu\beta}] \times \text{Tr} [\widehat{W}_{\mu\beta} \widehat{W}^{\alpha\nu}] , \\
\mathcal{O}_{T,2} &= \text{Tr} [\widehat{W}_{\alpha\mu} \widehat{W}^{\mu\beta}] \times \text{Tr} [\widehat{W}_{\beta\nu} \widehat{W}^{\nu\alpha}] , \\
\mathcal{O}_{T,5} &= \text{Tr} [\widehat{W}_{\mu\nu} \widehat{W}^{\mu\nu}] \times \widehat{B}_{\alpha\beta} \widehat{B}^{\alpha\beta} , \\
\mathcal{O}_{T,6} &= \text{Tr} [\widehat{W}_{\alpha\nu} \widehat{W}^{\mu\beta}] \times \widehat{B}_{\mu\beta} \widehat{B}^{\alpha\nu} , \\
\mathcal{O}_{T,7} &= \text{Tr} [\widehat{W}_{\alpha\mu} \widehat{W}^{\mu\beta}] \times \widehat{B}_{\beta\nu} \widehat{B}^{\nu\alpha} , \\
\mathcal{O}_{T,8} &= \widehat{B}_{\mu\nu} \widehat{B}^{\mu\nu} \widehat{B}_{\alpha\beta} \widehat{B}^{\alpha\beta} , \\
\mathcal{O}_{T,9} &= \widehat{B}_{\alpha\mu} \widehat{B}^{\mu\beta} \widehat{B}_{\beta\nu} \widehat{B}^{\nu\alpha} ,
\end{aligned} \tag{75}$$

or two of them each, called mixed,

$$\begin{aligned}
\mathcal{O}_{M,0} &= \text{Tr} [\widehat{W}_{\mu\nu} \widehat{W}^{\mu\nu}] \times [(D_\beta \Phi)^\dagger D^\beta \Phi] , \\
\mathcal{O}_{M,1} &= \text{Tr} [\widehat{W}_{\mu\nu} \widehat{W}^{\nu\beta}] \times [(D_\beta \Phi)^\dagger D^\mu \Phi] , \\
\mathcal{O}_{M,2} &= [\widehat{B}_{\mu\nu} \widehat{B}^{\mu\nu}] \times [(D_\beta \Phi)^\dagger D^\beta \Phi] , \\
\mathcal{O}_{M,3} &= [\widehat{B}_{\mu\nu} \widehat{B}^{\nu\beta}] \times [(D_\beta \Phi)^\dagger D^\mu \Phi] , \\
\mathcal{O}_{M,4} &= [(D_\mu \Phi)^\dagger \widehat{W}_{\beta\nu} D^\mu \Phi] \times \widehat{B}^{\beta\nu} , \\
\mathcal{O}_{M,5} &= [(D_\mu \Phi)^\dagger \widehat{W}_{\beta\nu} D^\nu \Phi] \times \widehat{B}^{\beta\mu} , \\
\mathcal{O}_{M,7} &= [(D_\mu \Phi)^\dagger \widehat{W}_{\beta\nu} \widehat{W}^{\beta\mu} D^\nu \Phi] .
\end{aligned} \tag{76}$$

In Ref. [148], two additional operators,

$$\begin{aligned}
\mathcal{O}_{T,3} &= \text{Tr} [\widehat{W}_{\alpha\mu} \widehat{W}^{\mu\beta} \widehat{W}^{\nu\alpha}] \times \widehat{B}_{\beta\nu} , \\
\mathcal{O}_{T,4} &= \text{Tr} [\widehat{W}_{\alpha\mu} \widehat{W}^{\alpha\mu} \widehat{W}^{\beta\nu}] \times \widehat{B}_{\beta\nu} ,
\end{aligned} \tag{77}$$

	$\mathcal{O}_{S,0}, \mathcal{O}_{M,0}, \mathcal{O}_{S,1}, \mathcal{O}_{M,1}, \mathcal{O}_{S,2}, \mathcal{O}_{M,7}$	$\mathcal{O}_{M,2}, \mathcal{O}_{M,3}, \mathcal{O}_{M,4}, \mathcal{O}_{M,5}$	$\mathcal{O}_{T,0}, \mathcal{O}_{T,1}, \mathcal{O}_{T,2}$	$\mathcal{O}_{T,5}, \mathcal{O}_{T,6}, \mathcal{O}_{T,7}$	$\mathcal{O}_{T,8}, \mathcal{O}_{T,9}$	
WWWW	X	X		X		
WWZZ	X	X	X	X	X	
ZZZZ	X	X	X	X	X	X
WWZ $\gamma$		X	X	X	X	
WW $\gamma\gamma$		X	X	X	X	
ZZZ $\gamma$		X	X	X	X	X
ZZ $\gamma\gamma$		X	X	X	X	X
Z $\gamma\gamma\gamma$				X	X	X
$\gamma\gamma\gamma\gamma$				X	X	X

TABLE IV. Quartic vertices modified by each dimension-8 operator are marked with X. Table adopted from Ref. [146].

have been defined, which however vanish identically. For  $\mathcal{O}_{T,3}$ , the trace is symmetric under permutations of indices  $\beta$  and  $\nu$ , while the field-strength tensor  $\widehat{B}_{\beta\nu}$  is anti-symmetric, and for  $\mathcal{O}_{T,4}$  the trace itself vanishes. The operator

$$\mathcal{O}_{M,6} = \left[ (D_\mu \Phi)^\dagger \widehat{W}_{\beta\nu} \widehat{W}^{\beta\nu} D^\mu \Phi \right], \quad (78)$$

which has also been introduced in Ref. [148], is equivalent to  $\mathcal{O}_{M,0}$  and the relation  $\mathcal{O}_{M,6} = \frac{1}{2} \mathcal{O}_{M,0}$  holds [150].

The scalar case contains an additional operator  $\mathcal{O}_{S,2}$  [149, 151, 152] compared to Ref. [148]. This operator cannot be constructed out of the other ones, but is a new, distinct possibility. This can be easily seen if we first consider the following building block appearing in the scalar dimension-8 operators

$$\begin{aligned} [(D_\mu \Phi)^\dagger D_\nu \Phi] &= \frac{1}{2} (\partial_\mu H) (\partial_\nu H) + M_W^2 W_\mu^- W_\nu^+ \left( 1 + \frac{H}{v} \right)^2 + \frac{M_Z^2}{2} Z_\mu Z_\nu \left( 1 + \frac{H}{v} \right)^2 \\ &+ \frac{iM_Z}{2} (Z_\mu (\partial_\nu H) - Z_\nu (\partial_\mu H)) \left( 1 + \frac{H}{v} \right). \end{aligned} \quad (79)$$

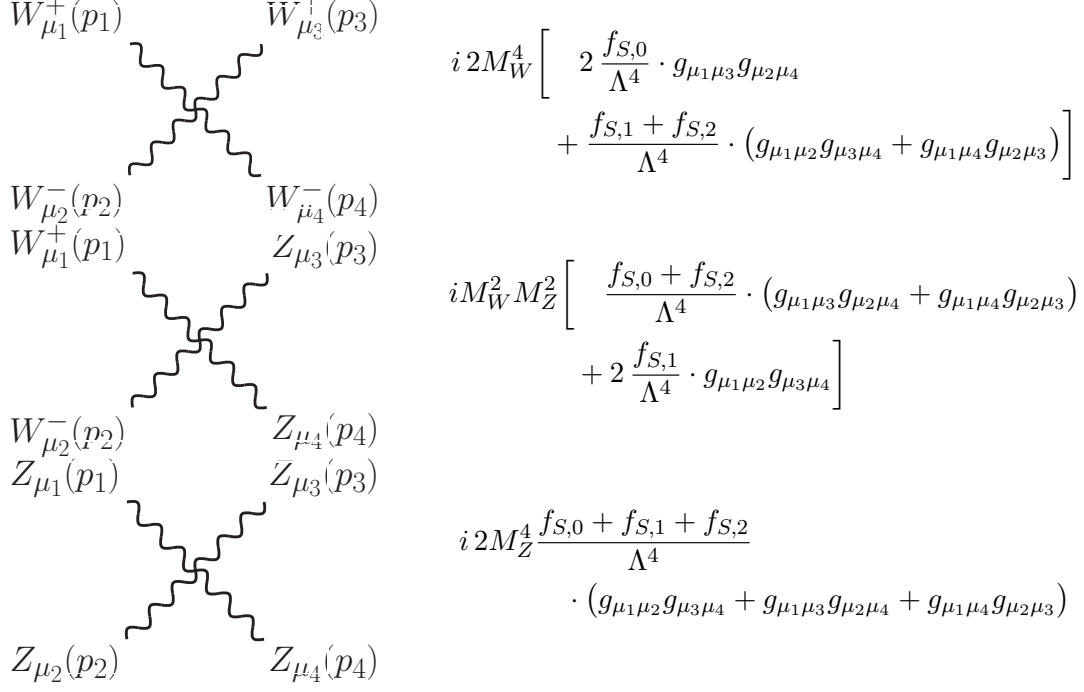


FIG. 21. Feynman rules for quartic gauge boson vertices originating from the operators  $\mathcal{O}_{S,0}$ ,  $\mathcal{O}_{S,1}$  and  $\mathcal{O}_{S,2}$ .

Therefore, for the operators one obtains

$$\begin{aligned}
\mathcal{O}_{S,0} \Big|_{4 \text{ gauge bosons}} &= M_W^4 W^- \cdot W^- W^+ \cdot W^+ \\
&+ M_W^2 M_Z^2 W^- \cdot Z W^+ \cdot Z \\
&+ \frac{1}{4} M_Z^4 Z \cdot Z Z \cdot Z, \\
\mathcal{O}_{S,1} \Big|_{4 \text{ gauge bosons}} &= M_W^4 W^- \cdot W^+ W^- \cdot W^+ \\
&+ M_W^2 M_Z^2 W^- \cdot W^+ Z \cdot Z \\
&+ \frac{1}{4} M_Z^4 Z \cdot Z Z \cdot Z, \\
\mathcal{O}_{S,2} \Big|_{4 \text{ gauge bosons}} &= M_W^4 W^- \cdot W^+ W^- \cdot W^+ \\
&+ M_W^2 M_Z^2 W^- \cdot Z W^+ \cdot Z \\
&+ \frac{1}{4} M_Z^4 Z \cdot Z Z \cdot Z,
\end{aligned} \tag{80}$$

where we have restricted ourselves now to only those terms which lead to an interaction of four gauge bosons, as only these are relevant for the discussion on VBF processes later. The corresponding Feynman rules are depicted in Fig. 21. From these expressions one sees immediately that there is no linear combination of  $\mathcal{O}_{S,0}$  and  $\mathcal{O}_{S,1}$  which would yield the correct form for  $\mathcal{O}_{S,2}$  for all three vertices. We will come back to this issue when discussing relations between different parametrizations below.

In Table IV, taken from Ref. [146], we show again which QGCs get modified by the different operators. One can see in particular that the operators  $\mathcal{O}_{T,8}$  and  $\mathcal{O}_{T,9}$  change the couplings between neutral gauge bosons only.

### 1. Non-linear Realization

The approach described above is based on a power counting in terms of the canonical dimension of the operators. An alternative possibility is given by the electroweak chiral Lagrangian, modeled in analogy to the chiral Lagrangian of QCD [153]. Here the expansion parameter is the chiral dimension of the operator [154–158], which is 0 for bosons and 1 for derivatives, couplings and fermion bilinears, and is equivalent to a loop expansion [159]. This approach has been originally formulated for scenarios without Higgs bosons [160–170] and later extended to include the possibility of a light Higgs boson [171–179]. The chiral Lagrangian is often also called non-linear EFT, as the Higgs and Goldstone fields appear in the operators in a non-linear way, while for the operators with higher canonical dimension discussed first the appearance through the fields  $\Phi$  is linear.

For quartic gauge boson interactions, two operators are relevant [180]:

$$\begin{aligned}\mathcal{L}_4 &= \alpha_4 (\text{Tr} [V_\mu V_\nu])^2, \\ \mathcal{L}_5 &= \alpha_5 (\text{Tr} [V_\mu V^\mu])^2,\end{aligned}\tag{81}$$

where  $\alpha_4$  and  $\alpha_5$  denote the dimensionless coefficients of the two operators, respectively. Additionally, the following definitions are used

$$\begin{aligned}V_\mu &= \Sigma (D_\mu \Sigma)^\dagger = - (D_\mu \Sigma) \Sigma^\dagger, \\ D_\mu \Sigma &= \partial_\mu \Sigma + ig \frac{\sigma^a}{2} W_\mu^a \Sigma - ig' \Sigma B_\mu \frac{\sigma^3}{2}, \\ \Sigma &= \exp \left( -\frac{i}{v} \sigma^a w^a \right) \stackrel{\text{unitary gauge}}{=} 1.\end{aligned}\tag{82}$$

The fields  $w^a$  denote the triplet of Goldstone bosons, which vanish in the unitary gauge we are going to employ, and  $\sigma^a$  are the Pauli matrices as before.

Inserting all definitions one obtains

$$\text{Tr}[V_\mu V_\nu] = -\frac{g^2}{2} (W_\mu^+ W_\nu^- + W_\mu^- W_\nu^+) - \frac{g^2}{2c_w^2} Z_\mu Z_\nu\tag{83}$$

and hence

$$\begin{aligned}
\mathcal{L}_4 &= \alpha_4 \left( 8 \frac{M_W^4}{v^4} (W^- \cdot W^- W^+ \cdot W^+ + W^- \cdot W^+ W^- \cdot W^+) \right. \\
&\quad \left. + 16 \frac{M_W^2 M_Z^2}{v^4} W^- \cdot Z W^+ \cdot Z \right. \\
&\quad \left. + 4 \frac{M_Z^4}{v^4} Z \cdot Z Z \cdot Z \right), \\
\mathcal{L}_5 &= \alpha_5 \left( 16 \frac{M_W^4}{v^4} W^- \cdot W^+ W^- \cdot W^+ \right. \\
&\quad \left. + 16 \frac{M_W^2 M_Z^2}{v^4} W^- \cdot W^+ Z \cdot Z \right. \\
&\quad \left. + 4 \frac{M_Z^4}{v^4} Z \cdot Z Z \cdot Z \right). \tag{84}
\end{aligned}$$

With the discovery of a light Higgs-like state at the LHC [1, 2, 181], this should also be reflected in the operators of the electroweak chiral Lagrangian. Therefore, in Ref. [182], a new set has been defined in analogy to the dimension-8 operators given in eq. (74)

$$\begin{aligned}
\mathcal{L}_{S,0} &= F_{S,0} \text{Tr} \left[ (D_\mu \hat{H})^\dagger D_\nu \hat{H} \right] \times \text{Tr} \left[ (D^\mu \hat{H})^\dagger D^\nu \hat{H} \right], \\
\mathcal{L}_{S,1} &= F_{S,1} \text{Tr} \left[ (D_\mu \hat{H})^\dagger D^\mu \hat{H} \right] \times \text{Tr} \left[ (D_\nu \hat{H})^\dagger D^\nu \hat{H} \right]. \tag{85}
\end{aligned}$$

Thereby,  $\hat{H}$  is a  $2 \times 2$  Hermitian matrix defined as

$$\hat{H} = \frac{1}{2} \begin{pmatrix} v + H - iw^3 & -i(w^1 - iw^2) \\ -i(w^1 + iw^2) & v + H + iw^3 \end{pmatrix} \stackrel{\text{unitary gauge}}{=} \frac{v + H}{2} \begin{pmatrix} 1 & 0 \\ 0 & 1 \end{pmatrix}, \tag{86}$$

where  $H$  is the physical Higgs boson and  $w^i$  are again the Goldstone bosons. The covariant derivative acting on  $\hat{H}$  is given by

$$D_\mu \hat{H} = \partial_\mu \hat{H} - ig \frac{\sigma^a}{2} W_\mu^a \hat{H} + ig' B_\mu \frac{\sigma^3}{2} \hat{H}. \tag{87}$$

The coefficients  $F_{S,0}$  and  $F_{S,1}$  are dimensionful with a mass dimension of  $-4$ .

Inserting the definitions yields

$$\begin{aligned}
\text{Tr}[(D_\mu \hat{H})^\dagger D_\nu \hat{H}] &= \frac{1}{2} (\partial_\mu H) (\partial_\nu H) + \frac{g^2 v^2}{8} (W_\mu^+ W_\nu^- + W_\mu^- W_\nu^+) \left(1 + \frac{H}{v}\right)^2 \\
&\quad + \frac{g^2 v^2}{8c_w^2} Z_\mu Z_\nu \left(1 + \frac{H}{v}\right)^2 \\
&= \frac{1}{2} (\partial_\mu H) (\partial_\nu H) + \frac{M_W^2}{2} (W_\mu^+ W_\nu^- + W_\mu^- W_\nu^+) \left(1 + \frac{H}{v}\right)^2 \\
&\quad + \frac{M_Z^2}{2} Z_\mu Z_\nu \left(1 + \frac{H}{v}\right)^2, \tag{88}
\end{aligned}$$

which is similar to the one obtained in eq. (79), but contains an extra symmetrization of the Lorentz indices. This becomes visible when looking at the  $W$  term and also the mixed  $Z(\partial H)$  terms vanish for this reason.



For the quartic gauge boson vertices, we get

$$\begin{aligned}
\mathcal{L}_{S,0} \Big|_{4 \text{ gauge bosons}} &= F_{S,0} \left( \frac{M_W^4}{2} (W^- \cdot W^- W^+ \cdot W^+ + W^- \cdot W^+ W^- \cdot W^+) \right. \\
&\quad \left. + M_W^2 M_Z^2 W^- \cdot Z W^+ \cdot Z \right. \\
&\quad \left. + \frac{M_Z^4}{4} Z \cdot Z Z \cdot Z \right), \\
\mathcal{L}_{S,1} \Big|_{4 \text{ gauge bosons}} &= F_{S,1} \left( M_W^4 W^- \cdot W^+ W^- \cdot W^+ \right. \\
&\quad \left. + M_W^2 M_Z^2 W^- \cdot W^+ Z \cdot Z \right. \\
&\quad \left. + \frac{M_Z^4}{4} Z \cdot Z Z \cdot Z \right). \tag{89}
\end{aligned}$$

A comparison of eq. (84) and eq. (89) shows that the functional form of the two sets is the same when considering quartic gauge-boson vertices only. This allows to define relations between the operator coefficients which lead to the same theoretical predictions. These connections are discussed in the following subsection.

## 2. Relations between Definitions

As mentioned above, two representations exist to define the operators of an EFT expansion, and within these approaches again different choices of equivalent operators are possible. The question is then what the relations between the different sets are, and which of them are equivalent. Equivalence hereby means that when setting the operator coefficients according to the relation, all physics observables produce the same results at LO for each set. This is true for example if the sets lead to the same Feynman rules for all vertices deviating from their SM values.

For practical applications often a weaker condition is sufficient, namely that the two operator sets agree for a certain subset of Feynman rules. An example would be experimental studies of a specific process. To compare the experimental measurements with theory predictions, Monte Carlo events with anomalous couplings switched on need to be generated. This can be a rather time-consuming processes, depending on the detail level of the event simulation. If one wants to quote the results not only for the operator set with which the study has performed, but also other parametrizations, it is helpful if the event simulation does not have to be repeated for the new set. Instead one can use relations, which allow to simply re-interpret the already derived results. For such a task it is sufficient if the relations only hold for those vertices which appear in the Feynman diagrams of the considered process. Other vertices are allowed to have different conversion rules without spoiling the results.

In the following, if no specific vertices or vertex classes are indicated, the relations hold for all and the corresponding operator sets are equivalent, otherwise this is only true for the quoted subset.

For the dimension-6 operators in eqs. (70, 71), an alternative parametrization commonly

used for LEP results exists [183]. The modified terms in the Lagrangian take the form

$$\begin{aligned}
\mathcal{L}_{\text{LEP}} = & \sum_{V=\gamma,Z} -ig_{WWV} (g_1^V (W_{\mu\nu}^+ W^{-\mu} - W^{+\mu} W_{\mu\nu}^-) V^\nu + \kappa_V W_\mu^+ W_\nu^- V^{\mu\nu} \\
& + \frac{\lambda_V}{M_W^2} W_\mu^{\nu+} W_\nu^{-\rho} V_\rho^\mu + ig_4^V W_\mu^+ W_\nu^- (\partial^\mu V^\nu + \partial^\nu V^\mu) \\
& - ig_5^V \epsilon^{\mu\nu\rho\sigma} (W_\mu^+ \partial_\rho W_\nu^- - \partial_\rho W_\mu^+ W_\nu^-) V_\sigma + \tilde{\kappa}_V W_\mu^+ W_\nu^- \tilde{V}^{\mu\nu} \\
& + \frac{\tilde{\lambda}_V}{M_W^2} W_\mu^{\nu+} W_\nu^{-\rho} \tilde{V}_\rho^\mu \Big), \tag{90}
\end{aligned}$$

where  $V_{\mu\nu} = \partial_\mu V_\nu - \partial_\nu V_\mu$  for  $V \in W^\pm, Z, \gamma$  and the coupling constants are  $g_{WW\gamma} = -e$  and  $g_{WWZ} = -e \frac{c_w}{s_w}$ . This parametrization is expressed in terms of the fields after electroweak symmetry breaking and in general does not conserve  $SU(2)_L$  symmetry. This choice is motivated by the fact that the maximal LEP energy of about 200 GeV is still below the electroweak symmetry breaking scale, while at the LHC, energies beyond this scale are probed. Electromagnetic gauge invariance imposes  $g_1^\gamma = 1$  and  $g_4^\gamma = g_5^\gamma = 0$ , so there are five independent operators which conserve both  $C$  and  $P$ ,  $g_1^Z, \kappa_\gamma, \kappa_Z, \lambda_\gamma, \lambda_Z$ , and six which violate  $C$  and/or  $P$ ,  $g_4^Z, g_5^Z, \tilde{\kappa}_\gamma, \tilde{\kappa}_Z, \tilde{\lambda}_\gamma, \tilde{\lambda}_Z$ .

These parameters can be related to the dimension-6 operators for the anomalous triple gauge couplings, obtaining [144, 146, 184]

$$\begin{aligned}
g_1^Z &= 1 + f_W \frac{M_Z^2}{2\Lambda^2}, \\
\kappa_\gamma &= 1 + (f_W + f_B) \frac{M_W^2}{2\Lambda^2}, \\
\kappa_Z &= 1 + (f_W - f_B \frac{s_w^2}{c_w^2}) \frac{M_W^2}{2\Lambda^2}, \\
\lambda_\gamma &= \lambda_Z = f_{WWW} \frac{3g^2 M_W^2}{2\Lambda^2}, \\
g_4^Z &= g_5^Z = 0, \\
\tilde{\lambda}_\gamma &= \tilde{\lambda}_Z = f_{\tilde{W}WW} \frac{3g^2 M_W^2}{2\Lambda^2}, \\
\tilde{\kappa}_\gamma &= f_{\tilde{W}} \frac{M_W^2}{2\Lambda^2}, \\
\tilde{\kappa}_Z &= -f_{\tilde{W}} \frac{s_w^2}{c_w^2} \frac{M_W^2}{2\Lambda^2}. \tag{91}
\end{aligned}$$

From the first three lines, one can directly deduce the relation [144]

$$\Delta g_1^Z = \Delta \kappa_Z + \frac{s_w^2}{c_w^2} \Delta \kappa_\gamma \tag{92}$$

with  $\Delta g_1^Z = g_1^Z - 1$ ,  $\Delta \kappa_{\gamma,Z} = \kappa_{\gamma,Z} - 1$ , and from the last two lines

$$\tilde{\kappa}_Z = -\frac{s_w^2}{c_w^2} \tilde{\kappa}_\gamma. \tag{93}$$

The Lagrangian of eq. (90) does not contain any quartic gauge boson vertices in contrast to the dimension-6 operators, so the relations above do not extend beyond triple gauge couplings. Also this Lagrangian is therefore not invariant under  $SU(2)_L$  gauge transformations.

For anomalous couplings of the two quartic vertices  $W^+W^-\gamma\gamma$  and  $ZZ\gamma\gamma$  two further operators have been defined for LEP [185, 186]

$$\begin{aligned}\mathcal{L}_0 &= -\frac{e^2}{16\Lambda^2}a_0F_{\mu\nu}F^{\mu\nu}W^{a,\alpha}W_\alpha^a, \\ \mathcal{L}_c &= -\frac{e^2}{16\Lambda^2}a_cF_{\mu\alpha}F^{\mu\beta}W^{a,\alpha}W_\beta^a,\end{aligned}\tag{94}$$

with

$$\begin{aligned}F^{\mu\nu} &= \partial^\mu A^\nu - \partial^\nu A^\mu, \\ W_\mu^a &= \left(\frac{1}{\sqrt{2}}(W_\mu^+ + W_\mu^-), \frac{i}{\sqrt{2}}(W_\mu^+ - W_\mu^-), \frac{Z_\mu}{c_w}\right),\end{aligned}\tag{95}$$

where  $A_\mu$  denotes the photon field. Vertex-specific relations only can be derived relating them to the mixed dimension-8 operators [146]

$$\begin{aligned}\frac{a_0}{\Lambda^2} &= g^2v^2 \left(\frac{f_{M,0}}{\Lambda^4} + \frac{1}{2}\frac{f_{M,2}}{\Lambda^4} \pm \frac{f_{M,4}}{\Lambda^4}\right), \\ \frac{a_c}{\Lambda^2} &= g^2v^2 \left(-\frac{f_{M,1}}{\Lambda^4} - \frac{1}{2}\frac{f_{M,3}}{\Lambda^4} \pm \frac{1}{2}\frac{f_{M,5}}{\Lambda^4} + \frac{1}{2}\frac{f_{M,7}}{\Lambda^4}\right),\end{aligned}\tag{96}$$

where the upper sign holds for the  $W^+W^-\gamma\gamma$  and the lower sign for the  $ZZ\gamma\gamma$  vertex. As in total eight dimension-8 operators contribute to the two vertices, only certain linear combinations are related to  $a_0$  or  $a_c$  and can possibly be determined from a measurement of those.

As last item we will compare the anomalous contributions to the quartic gauge-boson vertices, which due to historical reasons has lead to some confusion. The situation is complicated by the fact that there are two different conventions regarding the exact definition of the modified field-strength tensors  $\widehat{W}^{\mu\nu}$  and  $\widehat{B}^{\mu\nu}$  for the dimension-8 operators. In this article, we follow the same definition, eq. (67), which is commonly used for the dimension-6 operators, namely that they are multiplied with the respective coupling strength  $g$  and  $g'$ . This convention has also been used in Ref. [146] and the VBFNLO implementation. Refs. [148, 149], where the dimension-8 operators have first been defined, instead uses

$$\begin{aligned}\widehat{W}^{\text{EGM},\mu\nu} &= \frac{\sigma^j}{2}W^{j,\mu\nu} = \frac{\sigma^j}{2}(\partial^\mu W^{j,\nu} - \partial^\nu W^{j,\mu} - g\epsilon^{jkl}W^{k,\mu}W^{l,\nu}), \\ \widehat{B}^{\text{EGM},\mu\nu} &= B^{\mu\nu} = (\partial^\mu B^\nu - \partial^\nu B^\mu),\end{aligned}\tag{97}$$

such that

$$\widehat{W}^{\text{EGM},\mu\nu} = \frac{1}{ig}\widehat{W}^{\mu\nu}, \quad \widehat{B}^{\text{EGM},\mu\nu} = \frac{2}{ig'}\widehat{B}^{\mu\nu},\tag{98}$$

where here and in the following all variables following this definition are marked with the superscript EGM. This convention is employed in the FeynRules [187, 188] model file [189], which in turn is the common implementation for use in MadGraph5\_aMC@NLO [43].

This change in the modified field-strength tensors then leads to similar changes for the coefficients of the tensor and mixed operators, eqs. (75, 76), leading to the relations [146],

$$\begin{aligned}
f_{M,0,1} &= -\frac{1}{g^2} \cdot f_{M,0,1}^{\text{EGM}}, \\
f_{M,2,3} &= -\frac{4}{g'^2} \cdot f_{M,2,3}^{\text{EGM}}, \\
f_{M,4,5} &= -\frac{2}{gg'} \cdot f_{M,4,5}^{\text{EGM}}, \\
f_{M,7} &= -\frac{1}{g^2} \cdot f_{M,7}^{\text{EGM}}, \\
f_{T,0,1,2} &= \frac{1}{g^4} \cdot f_{T,0,1,2}^{\text{EGM}}, \\
f_{T,5,6,7} &= \frac{4}{g^2 g'^2} \cdot f_{T,5,6,7}^{\text{EGM}}, \\
f_{T,8,9} &= \frac{16}{g'^4} \cdot f_{T,8,9}^{\text{EGM}}, \tag{99}
\end{aligned}$$

while the scalar operators, eq. (74), stay identical.

As can be directly seen from comparing eq. (80) with eqs. (84, 89), there are also relations between the scalar dimension-8 operators and the operators from the electroweak chiral Lagrangian, the latter both without and with a Higgs boson.

For the chiral Lagrangian with Higgs boson, there is actually a full equivalence to the scalar dimension-8 operators. This can be seen most easily by comparing eqs. (79, 88), from which follows

$$\text{Tr}[(D_\mu \hat{H})^\dagger D_\nu \hat{H}] = \frac{1}{2} \left( [(D_\mu \Phi)^\dagger D_\nu \Phi] + [(D_\nu \Phi)^\dagger D_\mu \Phi] \right). \tag{100}$$

Hence for the operator coefficients we obtain

$$\begin{aligned}
F_{S,0} &= \frac{f_{S,0} + f_{S,2}}{\Lambda^4}, & f_{S,0} &= f_{S,2}, \\
F_{S,1} &= \frac{f_{S,1}}{\Lambda^4}. \tag{101}
\end{aligned}$$

For the non-linear formulation without Higgs boson, a relation can obviously be valid only for the quartic gauge-boson couplings, as no vertices with Higgs bosons are modified by  $\mathcal{L}_4$  and  $\mathcal{L}_5$ , which are however present in the dimension-8 operators. In this case we find

$$\begin{aligned}
\alpha_4 &= \frac{v^4}{16} F_{S,0} = \frac{v^4}{16} \frac{f_{S,0} + f_{S,2}}{\Lambda^4}, & f_{S,0} &= f_{S,2}, \\
\alpha_5 &= \frac{v^4}{16} F_{S,1} = \frac{v^4}{16} \frac{f_{S,1}}{\Lambda^4}, \tag{102}
\end{aligned}$$

where simultaneously also the correspondence to the with-Higgs case is shown. Parameter scenarios with  $f_{S,0} \neq f_{S,2}$  cannot be modeled in either chiral Lagrangian with the set of operators given so far. For this the inclusion of an additional operator [162]

$$\mathcal{L}_6 = \alpha_6 \text{Tr} [V_\mu V_\nu] \text{Tr} [TV^\mu] \text{Tr} [TV^\nu] \tag{103}$$

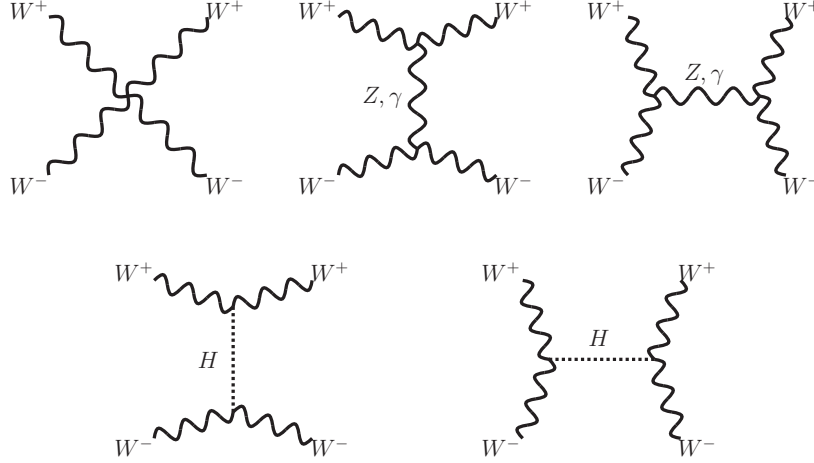


FIG. 22. Feynman diagrams contributing to  $WW$  scattering.

with  $T = \Sigma\sigma_3\Sigma^\dagger$  is necessary.

From these relations we see the importance of the new operator  $\mathcal{O}_{S,2}$ , which allows us to write the relations in the same way for all three quartic vertices with massive gauge bosons. If, as in the original set, this operator is not present, only vertex-specific conversion rules exist. This possibility arises only due to the fact that each of the three vertices contains at least two identical particles. The resulting symmetrization when generating Feynman rules from the Lagrangian means that for each of the  $WWWW$  and  $WWZZ$  vertices only two different Lorentz structures exist instead of the naively expected three. Therefore, two operators with different Lorentz structures are sufficient to generate all possibilities when considering a single vertex only. For the  $ZZZZ$  vertex only one Lorentz structure exists for the scalar operators as all particles are identical. The vertex-specific relations without  $\mathcal{O}_{S,2}$  read [146]

$$\begin{aligned}
\text{WWWW-vertex:} & \quad \alpha_4 = \frac{v^4 f_{S,0}}{8 \Lambda^4}, & \quad \alpha_4 + 2\alpha_5 = \frac{v^4 f_{S,1}}{8 \Lambda^4}, \\
\text{WWZZ-vertex:} & \quad \alpha_4 = \frac{v^4 f_{S,0}}{16 \Lambda^4}, & \quad \alpha_5 = \frac{v^4 f_{S,1}}{16 \Lambda^4}, \\
\text{ZZZZ-vertex:} & \quad \alpha_4 + \alpha_5 = \frac{v^4 f_{S,0} + f_{S,1}}{16 \Lambda^4}. & \quad (104)
\end{aligned}$$

These relations should however be considered a kludge only, and if possible the non-vertex-specific ones in eq. (102) including the operator  $\mathcal{O}_{S,2}$  used instead. For some processes this is even mandatory. An example is the VBF-production process of  $pp \rightarrow W^+W^-jj$ . For certain parton combinations like  $ud \rightarrow udW^+W^-$  both  $WWWW$ - and  $WWZZ$ -vertices appear in the same subprocess. In that case, the two operator sets can be related only according to eq. (102).

## B. Unitarity

The high-energy behavior of differential cross sections in vector-boson scattering is the result of a delicate cancellation between the different diagrams. For simplicity, let us consider only  $2 \rightarrow 2$  scattering of two on-shell longitudinal  $W$  bosons,  $W_L^+ W_L^- \rightarrow W_L^+ W_L^-$ . The contributing Feynman diagrams are depicted in Fig. 22. In the high-energy region, where  $E \gg M_W$ , the longitudinal polarization vector of each  $W$  can be approximated by

$$\epsilon_L^\mu = \frac{p^\mu}{M_W} + \mathcal{O}\left(\frac{M_W}{E}\right). \quad (105)$$

Considering the diagram with the quartic gauge-boson vertex only, its matrix element rises with  $\frac{s^2}{M_W^4}$ . The same behavior happens also for the two diagrams with a  $Z/\gamma$   $s$ - and  $t$ -channel exchange, with the same factor with an opposite sign such that the two terms cancel and the remaining dependence is  $\frac{s}{M_W^2}$ . This in turn is canceled by the two Higgs exchange diagrams depicted in the lower row of Fig. 22. Thus the leading energy behavior of the full matrix element is constant in energy [190].

Switching on anomalous couplings, this cancellation is in general violated. For example, the dimension-8 operators discussed before can modify the quartic vertex only, while leaving all others at their respective SM values. The corresponding rise in the amplitude at high energies means that at large enough values, unitarity of the scattering matrix gets violated. Then the probability interpretation does not hold any longer, as scattering must happen more often than the actual flux of incoming particles allows. This is of course an unphysical situation and needs to be avoided. The underlying reason is the breakdown of the expansion in eq. (64), where neglected higher-order terms are not sufficiently suppressed any longer and need to be taken into account as well.

### 1. Unitarity Bounds

First, we need to determine where unitarity becomes violated. A convenient tool for this task is partial wave analysis [191]. The starting point is unitarity of the  $S$  matrix

$$\begin{aligned} \mathbb{1} &= S^\dagger S = (\mathbb{1} + iT)^\dagger (\mathbb{1} + iT) \\ &= \mathbb{1} + T^\dagger T + i(T - T^\dagger) \\ \Rightarrow -i(T - T^\dagger) &= T^\dagger T \end{aligned} \quad (106)$$

with the matrix  $T = \frac{1}{i}(S - \mathbb{1})$ . This expression is now placed between two two-body states with momenta  $p_1, p_2$  and helicities  $\lambda_1, \lambda_2$ , and  $k_1, k_2, \kappa_1, \kappa_2$ , respectively,

$$\begin{aligned} -i(\langle k_1 k_2 \kappa_1 \kappa_2 | (T - T^\dagger) | p_1 p_2 \lambda_1 \lambda_2 \rangle) \\ = \sum_n \langle k_1 k_2 \kappa_1 \kappa_2 | T^\dagger | n \rangle \langle n | T | p_1 p_2 \lambda_1 \lambda_2 \rangle, \end{aligned} \quad (107)$$

where on the right-hand side we have inserted a full set of states  $\mathbb{1} = \sum_n |n\rangle \langle n|$ .

For simplicity, we choose a specific Lorentz frame and take the two incoming momenta aligned along the  $z$  axis in their center-of-mass frame,  $\vec{p}_1 = -\vec{p}_2$ , so  $T$  depends only on the

center-of-mass energy  $E$ . Then for a  $2 \rightarrow 2$  scattering process  $AB \rightarrow CD$ , one obtains [191]

$$\begin{aligned}
\langle p_3 p_4 \lambda_3 \lambda_4 | T | p_1 p_2 \lambda_1 \lambda_2 \rangle &= (2\pi)^4 \delta^{(4)}(p_1 + p_2 - p_3 - p_4) \langle \theta \phi \lambda_3 \lambda_4 | T(E) | 00 \lambda_1 \lambda_2 \rangle \\
&= (2\pi)^4 \delta^{(4)}(p_1 + p_2 - p_3 - p_4) \\
&\quad \cdot \mathcal{M}(A(p_1, \lambda_1), B(p_2, \lambda_2) \rightarrow C(p_3, \lambda_3), D(p_4, \lambda_4)),
\end{aligned} \tag{108}$$

where the momenta have been replaced by the scattering angles  $\theta$  and  $\phi$ , with the normalization

$$\langle p'_1 p'_2 \lambda'_1 \lambda'_2 | p_1 p_2 \lambda_1 \lambda_2 \rangle = 2E_1 2E_2 (2\pi)^6 \delta^{(3)}(\vec{p}'_1 - \vec{p}_1) \delta^{(3)}(\vec{p}'_2 - \vec{p}_2) \delta_{\lambda'_1 \lambda_1} \delta_{\lambda'_2 \lambda_2}. \tag{109}$$

$\mathcal{M}$  denotes the usual matrix element of the  $2 \rightarrow 2$  scattering process derived from Feynman rules.

The matrix element can now be decomposed into partial waves

$$\begin{aligned}
\langle \theta \phi \lambda_3 \lambda_4 | T(E) | 00 \lambda_1 \lambda_2 \rangle &= 16\pi \sum_J (2J+1) e^{i(\lambda_{12} - \lambda_{34})\phi} d_{\lambda_{12}\lambda_{34}}^J(\theta) \langle \lambda_3 \lambda_4 | T^J(E) | \lambda_1 \lambda_2 \rangle
\end{aligned} \tag{110}$$

with  $\lambda_{12} = \lambda_1 - \lambda_2$ ,  $\lambda_{34} = \lambda_3 - \lambda_4$  and the Wigner  $d$ -functions  $d_{\lambda\kappa}^J(\theta)$  (see e.g. Ref. [77] for tabulated values). For any initial or final state with identical particles an additional factor of  $\sqrt{2}$  must be inserted on the right-hand side of eq. (110) to account for the correct normalization of the wave function.

The Wigner  $d$ -functions obey a completeness relation

$$\int_{-1}^1 d \cos \theta d_{\lambda\kappa}^J(\theta) d_{\lambda'\kappa'}^J(\theta) = \frac{2}{2J+1} \delta_{JJ'} \tag{111}$$

which will be exploited in the next step.

Multiplying eq. (110) with  $\frac{1}{32\pi} \int_{-1}^1 d \cos \theta d_{\lambda_{12}\lambda_{34}}^J(\theta)$ , we can project out a specific partial wave

$$\begin{aligned}
a_{\lambda_{12}\lambda_{34}}^J &\equiv e^{i(\lambda_{12} - \lambda_{34})\phi} \langle \lambda_3 \lambda_4 | T^J(E) | \lambda_1 \lambda_2 \rangle \\
&= \frac{1}{32\pi} \int_{-1}^1 d \cos \theta d_{\lambda_{12}\lambda_{34}}^J(\theta) \langle \theta \phi \lambda_3 \lambda_4 | T(E) | 00 \lambda_1 \lambda_2 \rangle \\
&= \frac{1}{32\pi} \int_{-1}^1 d \cos \theta d_{\lambda_{12}\lambda_{34}}^J(\theta) \mathcal{M}(A(p_1, \lambda_1), B(p_2, \lambda_2) \rightarrow C(p_3, \lambda_3), D(p_4, \lambda_4)).
\end{aligned} \tag{112}$$

The factor for identical particles in the initial or final state becomes  $\frac{1}{\sqrt{2}}$  on the right-hand side for each pair.

Going back to eq. (107), we now apply this to the special case of identical initial and final states, which yields

$$\begin{aligned}
-i(\langle p_1 p_2 \lambda_1 \lambda_2 | (T - T^\dagger) | p_1 p_2 \lambda_1 \lambda_2 \rangle) &= \sum_n \langle p_1 p_2 \lambda_1 \lambda_2 | T^\dagger | n \rangle \langle n | T | p_1 p_2 \lambda_1 \lambda_2 \rangle \\
&= \sum_n \left| \langle n | T | p_1 p_2 \lambda_1 \lambda_2 \rangle \right|^2.
\end{aligned} \tag{113}$$

Furthermore, we restrict ourselves to two-particle states  $|n_2\rangle$  in the sum over states, and write down the helicity sum and the momentum integration explicitly. As non-negative terms on the right-hand side are dropped, the equation becomes an inequality. Leaving out the global factor for energy-momentum conservation on both sides, one gets

$$\begin{aligned}
& 2\Im\left(\mathcal{M}(A(p_1, \lambda_1), B(p_2, \lambda_2) \rightarrow A(p_1, \lambda_1), B(p_2, \lambda_2))\right) \\
& \geq \sum_{CD} \sum_{\lambda_3, \lambda_4} \int \frac{d^3 p_3}{(2\pi)^3 2E_3} \frac{d^3 p_4}{(2\pi)^3 2E_4} (2\pi)^4 \delta^{(4)}(p_1 + p_2 - p_3 - p_4) \\
& \quad \cdot \mathcal{M}^*(A(p_1, \lambda_1), B(p_2, \lambda_2) \rightarrow C(p_3, \lambda_3), D(p_4, \lambda_4)) \\
& \quad \cdot \mathcal{M}(A(p_1, \lambda_1), B(p_2, \lambda_2) \rightarrow C(p_3, \lambda_3), D(p_4, \lambda_4)) .
\end{aligned} \tag{114}$$

We then obtain after inserting the partial-wave expansion

$$\begin{aligned}
& 16\pi \sum_J (2J+1) d_{\lambda_{12}\lambda_{12}}^J(0) 2\Im(a_{\lambda_{12}\lambda_{12}}^J(AB \rightarrow AB)) \\
& \geq \sum_{CD} \sum_{\lambda_3, \lambda_4} \int d\Omega \frac{1}{16\pi^2} \frac{|\vec{p}_3|}{E} (16\pi)^2 \sum_{J', J} (2J'+1)(2J+1) \\
& \quad \cdot (d_{\lambda_{12}\lambda_{34}}^{J'} a_{\lambda_{12}\lambda_{34}}^{J'}(AB \rightarrow CD))^* d_{\lambda_{12}\lambda_{34}}^J a_{\lambda_{12}\lambda_{34}}^J(AB \rightarrow CD) \\
& \geq 16\pi \sum_J (2J+1) \sum_{CD} \sum_{\lambda_3, \lambda_4} \sum_{J'} (2J'+1) \\
& \quad \cdot a_{\lambda_{12}\lambda_{34}}^{J'*}(AB \rightarrow CD) a_{\lambda_{12}\lambda_{34}}^J(AB \rightarrow CD) \int_{-1}^1 d\cos\theta d_{\lambda_{12}\lambda_{34}}^{J'} d_{\lambda_{12}\lambda_{34}}^J \\
& \geq 16\pi \sum_J (2J+1) 2 \sum_{CD} \sum_{\lambda_3, \lambda_4} |a_{\lambda_{12}\lambda_{34}}^J(AB \rightarrow CD)|^2 .
\end{aligned} \tag{115}$$

Thereby, we have simplified the phase-space integral by applying  $\frac{|\vec{p}_3|}{E} \leq \frac{1}{2}$ , used that the Wigner  $d$ -functions are real, and exploited the orthogonality condition given in eq. (111). As angular momentum is conserved, the above equation must hold for each  $J$  separately. The sum on the right-hand side can be split into a part with same initial and final state and same helicity difference,  $AB = CD$  and  $\lambda_3 - \lambda_4 = \lambda_{12} \equiv \lambda$ , a sum over same states but different helicities, and a sum over different states. The first part might be associated with a multiplicity factor, depending on how often such a combination appears in the sum. This factor can simply be dropped without affecting the inequality. Noting that  $d_{\lambda\lambda}^J(0) = 1$ , one then obtains for the partial-wave coefficients

$$\begin{aligned}
& \left(\Re a_{\lambda\lambda}^J(AB \rightarrow AB)\right)^2 + \left(\Im a_{\lambda\lambda}^J(AB \rightarrow AB)\right)^2 - \Im a_{\lambda\lambda}^J(AB \rightarrow AB) \\
& \quad + \sum_{\kappa \neq \lambda} |a_{\lambda\kappa}^J(AB \rightarrow AB)|^2 + \sum_{CD \neq AB} \sum_{\kappa} |a_{\lambda\kappa}^J(AB \rightarrow CD)|^2 \leq 0 , \\
& \quad \left(\Re a_{\lambda\lambda}^J(AB \rightarrow AB)\right)^2 + \left(\Im a_{\lambda\lambda}^J(AB \rightarrow AB) - \frac{1}{2}\right)^2 \\
& \quad + \sum_{\kappa \neq \lambda} |a_{\lambda\kappa}^J(AB \rightarrow AB)|^2 + \sum_{CD \neq AB} \sum_{\kappa} |a_{\lambda\kappa}^J(AB \rightarrow CD)|^2 \leq \left(\frac{1}{2}\right)^2 .
\end{aligned} \tag{116}$$



From the last line it becomes clear that for  $a_{\lambda\lambda}^J(AB \rightarrow AB)$ , with all others set to zero, this inequality describes a circle around  $(0, \frac{1}{2})$  with radius  $\frac{1}{2}$ , the so-called Argand circle. For unitarity considerations based on tree-level matrix elements, which will be used in the following, this condition is slightly too restrictive. Here we assume that small imaginary parts will be generated by higher-order corrections, and the inequality above is applied to the real part of the partial-wave coefficient only. For all other partial waves the inequality restricts them to be inside a circle with radius  $\frac{1}{2}$  around the origin. Therefore, the unitarity condition for each partial wave of a  $2 \rightarrow 2$  matrix element reads

$$|\Re a_{\lambda\kappa}^J| \leq \frac{1}{2}. \quad (117)$$

For simplicity, we have restricted ourselves to a specific initial and final state with e.g. fixed helicities. Instead, we could have used normalized linear combinations of states, for which the derivation is valid as well, and eq. (117) also holds for those.

Studies of unitarity-violation bounds from anomalous couplings have been performed in Refs. [192–197]. A tool to calculate this tree-level unitarity bound for anomalous quartic gauge couplings in  $2 \rightarrow 2$  vector-boson scattering processes is available in Ref. [198].

For all processes with higher final-state multiplicities than 2, which includes all VBF processes, one would in principle need an extension of the above method. Up to now no such calculation is known in the literature. As the unitarity violation happens only in the vector boson scattering part, one extrapolates from the known results. Thereby, the virtual  $t$ -channel vector bosons together with the attached quark lines are replaced by corresponding on-shell counterparts. Also the two final-state bosons are placed on-shell. Their invariant mass is kept fixed and determines the relevant energy scale. The resulting  $2 \rightarrow 2$  vector-boson scattering process can now be analyzed according to eq. (117), and determines whether unitarity is preserved or not.

## 2. Unitarity Restoration

Having determined the condition for conservation of unitarity, the next question is what to do in case unitarity is violated. Here, one needs not to worry about arbitrarily high energies. Only energy scales smaller than the center-of-mass of the respective collider are an issue. For higher energies, one can always postulate that some unitarity-restoring mechanism kicks in between the largest reachable energy and the energy scale where unitarity violation starts.

One of the simplest approaches is to ignore the parameter space above which unitarity becomes violated. For variables which are directly related to the center-of-mass energy this can be easily achieved by not analyzing any data from this region. Difficulties may arise for observables where the unitarity-violation effect is spread over the whole range. Extracting information from those then becomes problematic. Another drawback is that one still expects some deviation from the SM prediction even in the unitarity-violating phase-space regions, but with a smaller contribution. Not using this at all potentially throws away information.

*a. Form Factor* Therefore, a possible refinement consists of damping the effect of anomalous couplings such that the unitarity bound is always respected. This damping can be achieved by multiplying the amplitude with an ad-hoc energy-dependent factor, a so-called form factor. In fact, the method described before can be seen as a special case

of this, with a step function switching off anomalous couplings at the violation threshold. The shape of the form factor is in principle arbitrary, but the required properties give some guidance. The magnitude of the partial wave depends only on the center-of-mass energy  $E$  of the  $2 \rightarrow 2$  scattering process, so this should hold for the form factor as well. Where unitarity is not an issue, at small energies, the original amplitude should be mostly unaltered, i.e. the factor close to 1. At very large energies, the form factor should counterbalance the growth of the amplitude with energy, i.e. if the amplitude shows a leading  $E^N$  behavior, the form factor should be proportional to  $E^{-n}$  with  $n \geq N$ .

A common choice is a dipole form factor [199], defined as [27–29]

$$F(E) = \left(1 + \frac{E^2}{\Lambda_{\text{FF}}^2}\right)^{-p}, \quad (118)$$

where  $\Lambda_{\text{FF}}$  parametrizes the characteristic scale where form-factor effects become relevant and  $p$  is the damping exponent. The latter must be chosen large enough that the amplitude growth is balanced, i.e. the minimal allowed value is  $p = 2$  for anomalous QGCs. Larger values are possible as well, then the anomalous couplings will be further damped at large energies.

For anomalous Higgs couplings in VBF- $H$  production, also the following form factors have been used commonly [200, 201]

$$\begin{aligned} F_1 &= \left(1 - \frac{q_1^2}{\Lambda_{\text{FF}}^2}\right)^{-1} \cdot \left(1 - \frac{q_2^2}{\Lambda_{\text{FF}}^2}\right)^{-1}, \\ F_2 &= -2 \Lambda_{\text{FF}}^2 C_0 (q_1^2, q_2^2, (q_1 + q_2)^2, \Lambda_{\text{FF}}^2, \Lambda_{\text{FF}}^2, \Lambda_{\text{FF}}^2), \end{aligned} \quad (119)$$

where  $q_1$  and  $q_2$  denote the  $t$ -channel momentum transfer on each side of the VBF process, and  $C_0$  is the usual scalar three-point function [65]. Note that  $q_1^2$  and  $q_2^2$  become large negative numbers when the momentum transfer increases. The use of  $C_0$  is inspired by the fact that the origin of such an anomalous coupling could be a loop of heavy particles which leads to an effective vertex when integrated out.

The form factor tool [198] already mentioned above can also calculate the necessary scale  $\Lambda_{\text{FF}}^2$  of a dipole form factor eq. (118) for anomalous QGCs. The input is the maximum energy of the collider  $\sqrt{s}$ , the exponent  $p$ , and of course the anomalous couplings themselves. From this, the largest value of  $\Lambda_{\text{FF}}^2$  is determined which still fulfills the unitarity condition eq. (117) up to a center-of-mass energy of  $\sqrt{s}$ .

*b. K-Matrix* Depending on the exact shape of the form factor, the damping at larger energies can exceed the amount required by the unitarity condition. The effect of anomalous couplings is maximized if we can find a form factor such that it exactly fulfills the unitarity bound. There are several methods which aim to construct such a factor, like the inverse amplitude method [202–209], N/D unitarization [203, 210], Padé unitarization [211–214], the  $K$ -matrix [12, 13, 180, 182, 215–218] or the closely related  $T$ -matrix [182, 219]. For anomalous QGCs, the  $K$ -matrix approach has been used most, so we will shortly summarize it, following the original presentation in Ref. [180]. It has been worked out for the chiral Lagrangian approach without Higgs, using the Lagrangian terms  $\mathcal{L}_4$  and  $\mathcal{L}_5$  defined in eq. (81). The translation to dimension-8 operators is easily done by applying the relations of eq. (102). Isospin conservation thereby requires us to set  $f_{S,0} = f_{S,2}$ .

The amplitude for the process  $W^+W^- \rightarrow ZZ$  is dominated by scattering of longitudinal bosons at high center-of-mass energies. There the polarization vectors can be approximated

by  $\epsilon_L^\mu(p) = \frac{p^\mu}{M}$ . This yields for the leading energy dependence of the amplitude, using the Feynman rule shown in Fig. 21,

$$A(W^+W^- \rightarrow ZZ) = A(s, t, u) = C_{02}(t^2 + u^2) + C_1s^2 \quad (120)$$

with

$$\begin{aligned} C_{02} &= \frac{1}{4} \frac{f_{S,0} + f_{S,2}}{\Lambda^4}, & f_{S,0} &= f_{S,2} \\ C_1 &= \frac{1}{2} \frac{f_{S,1}}{\Lambda^4}, \end{aligned} \quad (121)$$

and the momenta replaced by the Mandelstam variables  $s$ ,  $t$  and  $u$ . The SM part of the amplitude has been left out, as its leading term is constant in energy and does not need any unitarization on its own.

All other combinations of gauge bosons can be expressed by this master amplitude using the relations

$$\begin{aligned} A(W^+Z \rightarrow W^+Z) &= A(t, s, u), \\ A(W^+W^- \rightarrow W^+W^-) &= A(s, t, u) + A(t, s, u), \\ A(W^+W^+ \rightarrow W^+W^+) &= A(t, s, u) + A(u, s, t), \\ A(ZZ \rightarrow ZZ) &= A(s, t, u) + A(t, s, u) + A(u, s, t). \end{aligned} \quad (122)$$

To study unitarity, we need the eigenamplitudes both in spin and isospin. The gauge bosons are isospin eigenstates with [151, 220]

$$|W^\pm\rangle = \mp |1; \pm 1\rangle, \quad |Z\rangle = |1; 0\rangle, \quad (123)$$

which can be combined into two-gauge-boson product states, using the Condon-Shortley sign convention,

$$\begin{aligned} |W^\pm W^\pm\rangle &= |2; \pm 2\rangle, \\ |W^\pm Z\rangle &= \mp \frac{1}{\sqrt{2}} |2; \pm 1\rangle - \frac{1}{\sqrt{2}} |1; \pm 1\rangle, \\ |W^\pm W^\mp\rangle &= -\frac{1}{\sqrt{6}} |2; 0\rangle \mp \frac{1}{\sqrt{2}} |1; 0\rangle - \frac{1}{\sqrt{3}} |0; 0\rangle, \\ |ZZ\rangle &= \frac{2}{\sqrt{6}} |2; 0\rangle - \frac{1}{\sqrt{3}} |0; 0\rangle. \end{aligned} \quad (124)$$

Inserting these relations into eq. (122) and solving for the isospin eigenamplitudes yields

$$\begin{aligned} A_0(s, t, u) &= 3A(s, t, u) + A(t, s, u) + A(u, s, t) \\ &= C_{02}(2s^2 + 4t^2 + 4u^2) + C_1(3s^2 + t^2 + u^2), \\ A_1(s, t, u) &= A(t, s, u) - A(u, s, t) \\ &= C_{02}(u^2 - t^2) + C_1(t^2 - u^2), \\ A_2(s, t, u) &= A(t, s, u) + A(u, s, t) \\ &= C_{02}(2s^2 + t^2 + u^2) + C_1(t^2 + u^2). \end{aligned} \quad (125)$$

These are then decomposed into partial waves using eq. (112)

$$\begin{aligned}
a^{IJ}(s) &= \frac{1}{2} \frac{1}{32\pi} \int_{-1}^1 d \cos \theta A_I(s, t, u) d_{00}^J(\theta) \\
&= \frac{1}{32\pi} \int_{-s}^0 \frac{dt}{s} A_I(s, t, u) P_J(s, t, u),
\end{aligned} \tag{126}$$

where we have replaced the integration over the angle with the integration over the Mandelstam variable. When neglecting the gauge-boson masses, their relation is  $t = -\frac{s}{2}(1 - \cos \theta)$  and from  $u = -s - t$ . The Wigner  $d$ -functions with two zero indices are the ordinary Legendre polynomials  $P_J$ . The extra factor  $\frac{1}{2}$  is due to the wave-function normalization, as the eigenamplitudes have identical states for both initial and final state. The non-vanishing coefficients are

$$\begin{aligned}
32\pi a^{00}(s) &= \frac{14}{3} C_{02} s^2 + \frac{11}{3} C_1 s^2, \\
32\pi a^{02}(s) &= \frac{4}{15} C_{02} s^2 + \frac{1}{15} C_1 s^2, \\
32\pi a^{11}(s) &= \frac{1}{3} C_{02} s^2 - \frac{1}{3} C_1 s^2, \\
32\pi a^{20}(s) &= \frac{8}{3} C_{02} s^2 + \frac{2}{3} C_1 s^2, \\
32\pi a^{22}(s) &= \frac{1}{15} C_{02} s^2 + \frac{1}{15} C_1 s^2
\end{aligned} \tag{127}$$

using

$$\begin{aligned}
P_0(s, t, u) &= 1, & P_2(s, t, u) &= -2 + 3 \frac{t^2 + u^2}{s^2}, \\
P_1(s, t, u) &= \frac{t - u}{s} = \frac{u^2 - t^2}{s^2}, & P_3(s, t, u) &= 9 \frac{t^2 - u^2}{s^2} + 10 \frac{t^3 - u^3}{s^3},
\end{aligned} \tag{128}$$

i.e. all coefficients with  $J = 3$  and higher vanish. As  $s, t$  and  $u$  are not independent of each other, there is no unique way to write the Legendre polynomials as functions of them. The expressions shown here are the form we will need later when back-substituting.

The partial waves computed at tree-level are real. To project this onto the Argand circle, we draw a straight line from  $a^{IJ}$  to the top of the circle and determine the intersection between the line and the circle. This yields for the unitarized partial wave

$$\hat{a}^{IJ} = \frac{a^{IJ}}{1 - ia^{IJ}}. \tag{129}$$

A graphical representation of this procedure is drawn in Fig. 23. When  $a^{IJ}$  goes to infinity, the unitarized partial wave reaches the top of the circle,  $\hat{a}^{IJ} = i$ . As this position is associated with the crossing of a resonance (compare with a Breit-Wigner propagator, which becomes purely imaginary at the resonance peak), the  $K$ -matrix scheme formally corresponds to placing a resonance at infinity, which also has infinite width [180]. For later it is useful to split the unitarized partial wave into the original expression and a counter-term containing the correction,

$$\Delta a^{IJ} = \hat{a}^{IJ} - a^{IJ} = \frac{i (a^{IJ})^2}{1 - ia^{IJ}}, \tag{130}$$

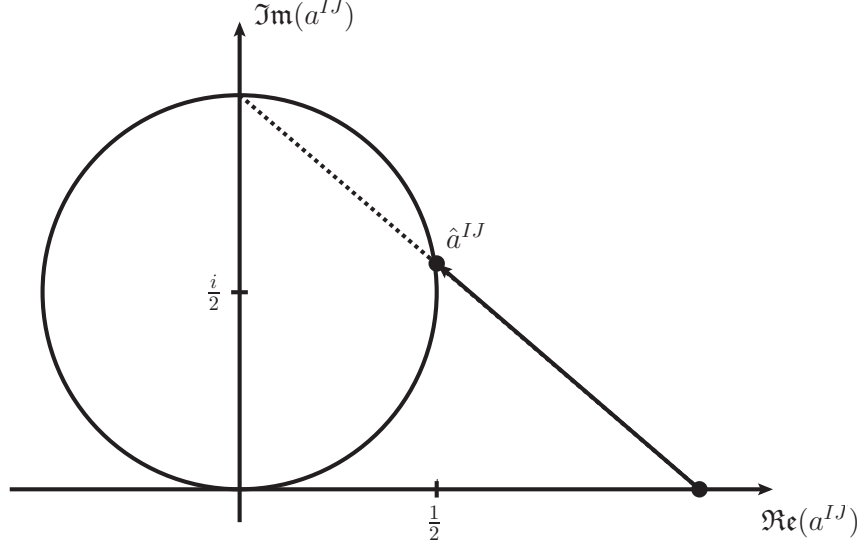


FIG. 23. Graphical representation of the Argand circle and the  $K$ -matrix unitarization method, an inverse stereographic projection, for the partial wave  $a^{IJ}$  leading to the unitarized partial wave  $\hat{a}^{IJ}$ .

yielding explicitly

$$\begin{aligned}
\Delta A^{00} &\equiv 32\pi \Delta a^{00} = -\frac{(14C_{02} + 11C_1)^2}{3((14C_{02} + 11C_1)s^2 + 96\pi i)} s^4, \\
\Delta A^{02} &\equiv 32\pi \Delta a^{02} = -\frac{(4C_{02} + C_1)^2}{15((4C_{02} + C_1)s^2 + 480\pi i)} s^4, \\
\Delta A^{11} &\equiv 32\pi \Delta a^{11} = -\frac{(C_{02} - C_1)^2}{3((C_{02} - C_1)s^2 + 96\pi i)} s^4, \\
\Delta A^{20} &\equiv 32\pi \Delta a^{20} = -\frac{(8C_{02} + 2C_1)^2}{3((8C_{02} + 2C_1)s^2 + 96\pi i)} s^4, \\
\Delta A^{22} &\equiv 32\pi \Delta a^{22} = -\frac{(C_{02} + C_1)^2}{15((C_{02} + C_1)s^2 + 480\pi i)} s^4.
\end{aligned} \tag{131}$$

This needs to be translated back to the physical amplitudes by inverting the relations eq. (126), i.e. using eq. (110),

$$\Delta A_I(s, t, u) = \sum_J (2J + 1) P_J(s, t, u) 32\pi \Delta a^{IJ}(s), \tag{132}$$

yielding explicitly

$$\begin{aligned}
\Delta A_0(s, t, u) &= \frac{\Delta A^{00} - 10\Delta A^{02}}{s^2} s^2 + \frac{15\Delta A^{02}}{s^2} (t^2 + u^2), \\
\Delta A_1(s, t, u) &= \frac{3\Delta A^{11}}{s^2} (u^2 - t^2), \\
\Delta A_2(s, t, u) &= \frac{\Delta A^{20} - 10\Delta A^{22}}{s^2} s^2 + \frac{15\Delta A^{22}}{s^2} (t^2 + u^2).
\end{aligned} \tag{133}$$

This is then put into relations derived from inverting eq. (125) and inserted into eq. (122) to yield for the unitarized on-shell scattering amplitudes [151, 180]

$$\begin{aligned}
& \widehat{A}(W^+W^- \rightarrow ZZ) \\
&= A(W^+W^- \rightarrow ZZ) + \frac{1}{3}\Delta A_0(s, t, u) - \frac{1}{3}\Delta A_2(s, t, u) \\
&= (t^2 + u^2) \cdot \left( C_{02} + \frac{5(\Delta A^{02} - \Delta A^{22})}{s^2} \right) \\
&\quad + s^2 \cdot \left( C_1 + \frac{(\Delta A^{00} - \Delta A^{20}) - 10(\Delta A^{02} - \Delta A^{22})}{3s^2} \right), \tag{134}
\end{aligned}$$

$$\begin{aligned}
& \widehat{A}(W^+Z \rightarrow W^+Z) \\
&= A(W^+Z \rightarrow W^+Z) + \frac{1}{2}\Delta A_1(s, t, u) + \frac{1}{2}\Delta A_2(s, t, u) \\
&= s^2 \cdot \left( C_{02} + \frac{\Delta A^{20} - 10\Delta A^{22}}{2s^2} \right) \\
&\quad + u^2 \cdot \left( C_{02} + \frac{15\Delta A^{22} + 3\Delta A^{11}}{2s^2} \right) \\
&\quad + t^2 \cdot \left( C_1 + \frac{15\Delta A^{22} - 3\Delta A^{11}}{2s^2} \right), \tag{135}
\end{aligned}$$

$$\begin{aligned}
& \widehat{A}(W^+W^- \rightarrow W^+W^-) \\
&= A(W^+W^- \rightarrow W^+W^-) + \frac{1}{3}\Delta A_0(s, t, u) + \frac{1}{2}\Delta A_1(s, t, u) + \frac{1}{6}\Delta A_2(s, t, u) \\
&= s^2 \cdot \left( C_{02} + C_1 \right. \\
&\quad \left. + \frac{(2\Delta A^{00} + \Delta A^{20}) - 10(2\Delta A^{02} + \Delta A^{22})}{6s^2} \right) \\
&\quad + t^2 \cdot \left( C_{02} + C_1 + \frac{10\Delta A^{02} - 3\Delta A^{11} + 5\Delta A^{22}}{2s^2} \right) \\
&\quad + u^2 \cdot \left( 2 \cdot C_{02} + \frac{10\Delta A^{02} + 3\Delta A^{11} + 5\Delta A^{22}}{2s^2} \right), \tag{136}
\end{aligned}$$

$$\begin{aligned}
& \widehat{A}(W^+W^+ \rightarrow W^+W^+) \\
&= A(W^+W^+ \rightarrow W^+W^+) + \Delta A_2(s, t, u) \\
&= s^2 \cdot \left( 2 \cdot C_{02} + \frac{\Delta A^{20} - 10\Delta A^{22}}{s^2} \right) \\
&\quad + (t^2 + u^2) \cdot \left( C_{02} + C_1 + \frac{15\Delta A^{22}}{s^2} \right), \tag{137}
\end{aligned}$$

$$\begin{aligned}
& \widehat{A}(ZZ \rightarrow ZZ) \\
&= A(ZZ \rightarrow ZZ) + \frac{1}{3}\Delta A_0(s, t, u) + \frac{2}{3}\Delta A_2(s, t, u) \\
&= s^2 \cdot \left( 2 \cdot C_{02} + C_1 \right. \\
&\quad \left. + \frac{(\Delta A^{00} + 2\Delta A^{20}) - 10(\Delta A^{02} + 2\Delta A^{22})}{3s^2} \right) \\
&\quad + (t^2 + u^2) \cdot \left( 2 \cdot C_{02} + C_1 + \frac{5(\Delta A^{02} + 2\Delta A^{22})}{s^2} \right). \tag{138}
\end{aligned}$$

As unitarization of the partial wave and hence of the  $K$ -matrix depends on the center-of-mass energy  $\sqrt{s}$  only, crossing symmetry between the different amplitudes becomes broken, as is obvious from the explicit form of the amplitudes.

Figs. 24 and 25 show the effect of unitarization on partial waves. Both plots have been generated using code from the VBFNLO form factor tool [198]. In Fig. 24 we apply  $K$ -matrix unitarization to the process  $W^+W^+ \rightarrow W^+W^+$ . As anomalous coupling,  $\frac{f_{S,1}}{\Lambda^4} = 400 \text{ TeV}^{-4}$  is used and the SM contribution to the amplitude switched off. This value is compatible with the current experimental bounds from run-I of the LHC [221] and testable with additional data from run-II. We compare the  $J = 0$  partial wave before and after applying  $K$ -matrix unitarization. This requires us to set  $\lambda_1 = \lambda_2$  and  $\lambda_3 = \lambda_4$ , but leaves the individual values of the initial and final-state polarizations still open. As the anomalous coupling operator  $\mathcal{O}_{S,1}$  generates interactions between longitudinal bosons, it is the  $\lambda_i = 0$  combination which we need to consider here. We see that the unmodified partial wave  $a_{00}^0$ , which is real, quickly rises with the center-of-mass energy  $\sqrt{s}$  and exceeds the unitarity bound eq. (117) at  $\sqrt{s} = 795 \text{ GeV}$ . Applying  $K$ -matrix unitarization, the unitarized partial wave  $\widehat{a}_{00}^0$  becomes complex. The figure shows its real and imaginary part as well as its distance from the center of the Argand circle. These three curves exhibit exactly the behavior one expects from the discussion beforehand. When the partial wave approaches the unitarity limit, the projection onto the circle induces an imaginary part and cuts off the real part at 0.5. For large values the projected partial wave approaches imaginary unity. Due to the projection onto the circle, the distance should be constant and have a value of 0.5. The small deviation one observes is due to the fact that in the derivation of the  $K$ -matrix we have taken the longitudinal polarization vectors in the high-energy limit and neglected terms proportional to the gauge-boson mass, whose contribution we see here. Fig. 25 shows a comparison of SM, pure anomalous couplings, and different unitarization methods for the zeroth partial

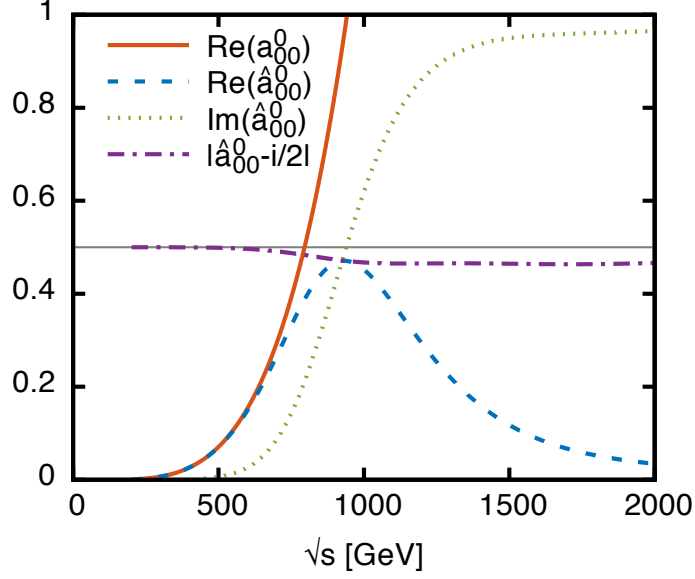


FIG. 24. Comparison of the  $J = 0$  partial wave  $a_{00}^0$  induced by the anomalous coupling  $\frac{f_{S,1}}{\Lambda^4} = 400 \text{ TeV}^{-4}$  with its  $K$ -matrix-unitarized version  $\hat{a}_{00}^0$  for the process  $W^+W^+ \rightarrow W^+W^+$ . The SM contribution to the amplitude has been turned off.

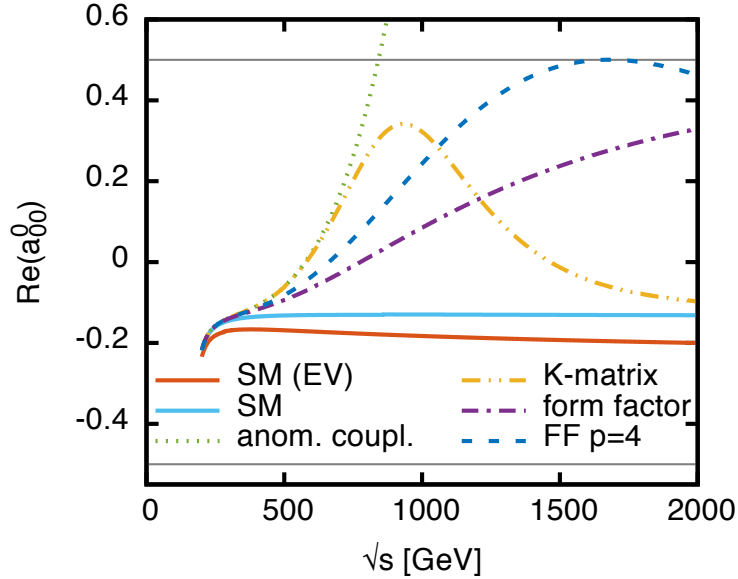


FIG. 25. Zeroth partial wave of the  $W^+W^+ \rightarrow W^+W^+$  amplitude for the SM and with anomalous coupling  $\frac{f_{S,1}}{\Lambda^4} = 400 \text{ TeV}^{-4}$ , either unmodified or including different unitarization prescriptions. All curves show longitudinal boson scattering except the one labeled “SM (EV)”, which is the most restrictive linear combination and dominated by scattering of transverse bosons. Additionally the unitarity bound at  $\pm 0.5$  is plotted.



wave. As in the previous plot, we study the process  $W^+W^+ \rightarrow W^+W^+$  with anomalous coupling  $\frac{f_{S,1}}{\Lambda^4} = 400 \text{ TeV}^{-4}$ . To obtain the most restrictive bound in the SM, we compute all possible polarization combinations and then diagonalize the resulting  $3 \times 3$  matrix, which yields the curve labeled "SM (EV)", where EV stands for "largest eigenvalue". Its largest contribution comes from the scattering of transverse gauge bosons, where all bosons have the same polarization. All other curves show the scattering of longitudinal gauge bosons, which is the dominant source for interactions induced by the anomalous coupling. For the SM part, there is actually an additional complication due to virtual photon exchange in the  $t$ -channel. As photons are massless, they mediate long-range interactions, which lead to a Coulomb singularity when the scattering angle  $\theta$  approaches zero. In the full VBF process, the initial-state gauge bosons are virtual themselves and no singularity appears. For the partial-wave analysis, which includes an integral over the scattering angle, we exclude this region by introducing a lower cutoff for the angle. This comes at the cost of making the partial-wave coefficient dependent on its value. Thereby, the full process can give us some guidance at which momentum transfer the contribution to the cross section becomes negligible. Converted into a scattering angle for the  $2 \rightarrow 2$  process of  $W$ -boson scattering, this corresponds to about one degree, which we use as the minimal angle. We have also studied the effects of varying this cutoff. Lowering it to 0.01 degrees enlarges the absolute value of the SM partial-wave coefficients by approximately 0.01. Thus there is only a mild dependence on the actual value.

Switching the anomalous coupling on, the corresponding partial wave, which now includes the SM contribution, crosses the unitarity bound at  $\sqrt{s} = 834 \text{ GeV}$ . All unitarization methods restrict the real part of the partial wave to be inside the unitarity limits. The  $K$ -matrix method does not even reach it completely due to the effect of the added SM contribution. For the dipole form factor, eq. (118), the minimal exponent to counterbalance the rise induced by the anomalous coupling is  $p = 2$ . In this case one needs to set  $\Lambda_{\text{FF}} = 832 \text{ GeV}$  to exactly touch the unitarity bound at high energies. In the figure only the rise is visible, the limit would be fulfilled only at the highest checked energy, which is the collider center-of-mass energy taken as  $13 \text{ TeV}$ . Taking higher exponents is possible as well. Therefore the figure also shows a second form factor curve with  $p = 4$ , for which the maximal scale is  $\Lambda_{\text{FF},p=4} = 1667 \text{ GeV}$ . This setting yields a larger contribution at smaller energies, and the unitarity bound is touched at the same value. For higher energies, the larger damping lets the partial wave decrease again and eventually it approaches the SM-only curve for very high energies.

To make use of the unitarization in vector-boson scattering, the expressions in eqs. 134 to 138 need to be generalized to the off-shell case as the final step. Taking the amplitude for  $W^+Z \rightarrow W^+Z$ ,

$$A(W^+Z \rightarrow W^+Z) = C_{02}(s^2 + u^2) + C_1t^2 \quad (139)$$

as an example, the procedure is as follows. First, one compares the corresponding coefficients in front of the original and the unitarized amplitude, i.e.

$$\begin{aligned} s^2 : \quad C_{02} &\rightarrow C_{02} + \frac{\Delta A^{20} - 10\Delta A^{22}}{2s^2}, \\ t^2 : \quad C_1 &\rightarrow C_1 + \frac{15\Delta A^{22} - 3\Delta A^{11}}{2s^2}, \\ u^2 : \quad C_{02} &\rightarrow C_{02} + \frac{15\Delta A^{22} + 3\Delta A^{11}}{2s^2}. \end{aligned}$$

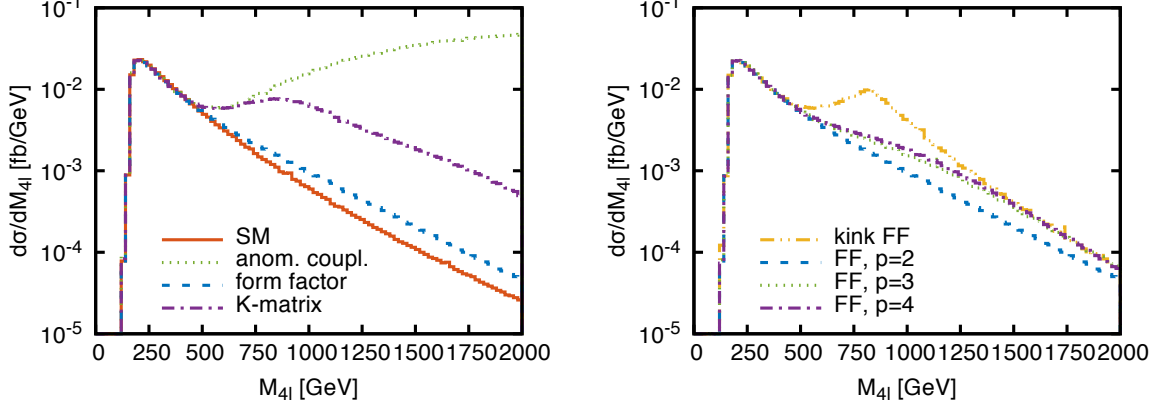


FIG. 26. Invariant mass distribution of the four final-state leptons for the VBF production process  $pp \rightarrow e^+\nu_e\mu^+\nu_\mu jj$  at NLO QCD for the LHC with a center-of-mass energy of 13 TeV. *Left:* Comparison of the SM contribution, with switching on the anomalous QGC  $\frac{f_{S,1}}{\Lambda^4} = 400 \text{ TeV}^{-4}$ , and including unitarization either via form factor, eq. (118), or using the  $K$ -matrix method. *Right:* Different choices of the exponent of the dipole form factor with corresponding scales and a kink function form factor clipping the amplitude at the unitarity boundary.

Then we identify the squares of the Mandelstam variables with the corresponding factors of  $g_{\mu\nu}g_{\rho\sigma}$  in the Feynman rules in Fig. 21. Then we obtain

$$\begin{array}{c}
 W_{\mu_1}^+(p_1) \quad W_{\mu_3}^-(p_3) \\
 \diagdown \quad \diagup \\
 \text{---} \quad \text{---} \\
 \diagup \quad \diagdown \\
 Z_{\mu_2}(p_2) \quad Z_{\mu_4}(p_4) \\
 \xrightarrow{t}
 \end{array}
 \quad
 iM_W^2 M_Z^2
 \left[
 \begin{array}{l}
 \left( \frac{f_{S,0} + f_{S,2}}{\Lambda^4} + 2 \frac{\Delta A^{20} - 10\Delta A^{22}}{s^2} \right) g_{\mu_1\mu_2} g_{\mu_3\mu_4} \\
 + \left( 2 \frac{f_{S,1}}{\Lambda^4} + 2 \frac{15\Delta A^{22} - 3\Delta A^{11}}{s^2} \right) g_{\mu_1\mu_3} g_{\mu_2\mu_4} \\
 + \left( \frac{f_{S,0} + f_{S,2}}{\Lambda^4} + 2 \frac{15\Delta A^{22} + 3\Delta A^{11}}{s^2} \right) g_{\mu_1\mu_4} g_{\mu_2\mu_3}
 \end{array}
 \right],$$

and analogously for all other vertices. As for the amplitudes, the resulting Feynman rules are no longer invariant under crossing initial and final state. Therefore, the flow of time has been indicated by a small arrow. This and the corresponding Feynman rules for the other vertices can now be used for our calculation of VBF processes to give  $K$ -matrix unitarized cross sections.

### C. Cross Section Results

As last part of the discussion on anomalous couplings, we apply the previously obtained results to VBF processes and show distributions of differential cross sections.

The distribution of vector-boson scattering processes most directly connected to anomalous QGCs is of course the invariant mass of the four final-state leptons. Fig. 26 shows this

distribution at NLO QCD accuracy for VBF- $W^+W^+jj$  production with leptonic decays for the LHC at a center-of-mass energy of 13 TeV. The electroweak parameters are set as defined in eq. (43) and the cuts chosen according to eqs. (44, 46). As anomalous QGC we take again  $\frac{f_{S,1}}{\Lambda^4} = 400 \text{ TeV}^{-4}$ . The curves have been generated with VBFNLO [27–29]. The left panel compares the differential cross sections of the SM, with the anomalous coupling switched on, and with two unitarization methods, namely  $K$ -matrix and a dipole form factor, eq. (118), with exponent  $p = 2$  and scale  $\Lambda_{\text{FF}} = 832 \text{ GeV}$ . Visible deviations from the SM result induced by anomalous couplings set in at an invariant mass of about 400 GeV. After this, the curve with the unmodified anomalous coupling quickly rises and shows a clear unitarity-violating behavior. At the upper end of the plot at 2 TeV, the differential cross section is larger than the SM result by three orders of magnitude. Its leading  $s^4$  behavior still leads to a rise, as it compensates the  $\frac{1}{s}$  factor in the flux factor and the PDF suppression. The  $K$ -matrix curve also shows a strong rise where the anomalous-coupling effect sets in, but then the rise is damped by the projection onto the Argand circle. Eventually the contribution falls in parallel with the SM contribution, with an approximately constant factor between them. Unitarizing the amplitude with a dipole form factor, the difference rises gradually with growing invariant mass. The whole picture is actually similar to what we have seen already in Fig. 25 for the partial wave analysis. Both anomalous couplings and  $K$ -matrix show a rise, then the  $K$ -matrix gets cut off at the unitarity bound, while the form factor part grows slowly but steadily. The right panel shows different choices for the form factor settings. Besides the curve with  $p = 2$  that was already part of the left panel, also the ones with  $p = 3$  and  $\Lambda_{\text{FF},p=3} = 1342 \text{ GeV}$  as well as  $p = 4$  and  $\Lambda_{\text{FF},p=4} = 1667 \text{ GeV}$  are plotted. Higher exponents combined with the maximally allowed value for  $\Lambda_{\text{FF}}$  yield a larger contribution at smaller invariant masses. When going to higher values, the additional damping starts to set in and reduces the differential cross section again towards the SM curve, thus crossing the lines with lower exponents. Additionally we define a kink-function like form factor as

$$F_{\text{kink}}(E) = \begin{cases} 1 & \text{for } E \leq \Lambda_{\text{FF,kink}} , \\ \left(\frac{\Lambda_{\text{FF,kink}}}{E}\right)^4 & \text{for } E > \Lambda_{\text{FF,kink}} , \end{cases} \quad (140)$$

with  $\Lambda_{\text{FF,kink}} = 834 \text{ GeV}$  chosen as the scale where unitarity violation happens. A partial wave analysis of the on-shell scattering process shows that this leads to an unmodified rise up to the form factor scale and then leaves the partial wave constant up to tiny effects of  $\mathcal{O}\left(\frac{M}{E}\right)$ . Thus, it stays at the unitarity bound and maximizes the contribution, similar to the  $K$ -matrix projection. This is also visible in the differential cross section plot in Fig. 26. Up to the form factor scale, the curve follows exactly the one for the unmodified anomalous coupling. There, a kink is visible and the distribution falls again. The dropoff is steeper than for the  $K$ -matrix, as there the decomposition into eigenstates and moving into the complex plane allows for a larger contribution. The various curves also illustrate that depending on the unitarization method chosen, the largest deviation from the SM happens in different phase-space regions, and all need to be considered when comparing with experimental data.

The left panel of Fig. 27 shows the distribution of the transverse momentum of the leading lepton, i.e. the one with the larger transverse momentum. The behavior of the different curves is similar to the previous plot. With anomalous couplings switched on, the curve exceeds the one obtained from applying the  $K$ -matrix or a kink form factor basically everywhere. This means that the unitarity-violating contributions get spread out over the whole range of the distribution. On the right-hand side of Fig. 27 we finally present the transverse

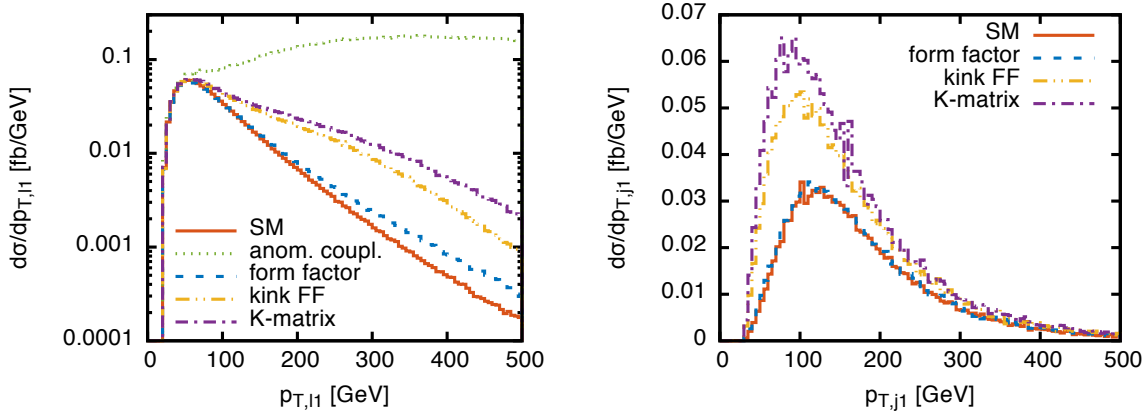


FIG. 27. Transverse momentum distribution of the leading lepton (*left*) and the leading jet (*right*) for the VBF production process  $pp \rightarrow e^+ \nu_e \mu^+ \nu_\mu jj$  at NLO QCD for the LHC with a center-of-mass energy of 13 TeV.

momentum distribution of the leading jet. This observable is not directly connected to the four-lepton invariant mass, and so the main effect is a global rise of the cross section when compared to the SM case. Small shape changes do occur however. This is best visible when looking at the respective positions of the cross-section peak. The larger the contribution from anomalous couplings, the more it shifts towards slightly smaller values. This effect originates from the chosen anomalous coupling operator  $\mathcal{O}_{S,1}$ , which enhances the fraction of longitudinally polarized gauge bosons. These lead to smaller transverse momenta of the jets than transverse polarized ones. If for example the operator  $\mathcal{O}_{T,0}$  is used instead, the position of the peak remains almost unchanged.

## VI. EXPERIMENTAL STATUS

Having discussed the theoretical backgrounds of vector-boson fusion and vector-boson scattering so far, we finally turn to an overview of the current experimental results and future prospects. For a recent overview on the experimental status and prospects see also Refs. [222, 223].

### A. LHC Run-I Results

The VBF production process studied most so far is production of a Higgs boson plus two jets. The presence of this mode is well established with a significance of 5.4 standard deviations (4.7 expected) in the combination of ATLAS and CMS results [181]. The Higgs decay modes which enter this result are  $\gamma\gamma$ ,  $\tau\tau$ ,  $WW$  and  $ZZ$ . The ratio of the measured cross section over the SM prediction is determined as  $\mu_{\text{VBF}} = 1.18^{+0.25}_{-0.23}$ . Hence, there is good agreement between theory and experiment. Additionally, the VBF- $H$  production process is an ideal place to study Higgs decays into invisible particles, which lead to a signature of missing transverse momentum in the detector [224]. Current data places an upper limit of

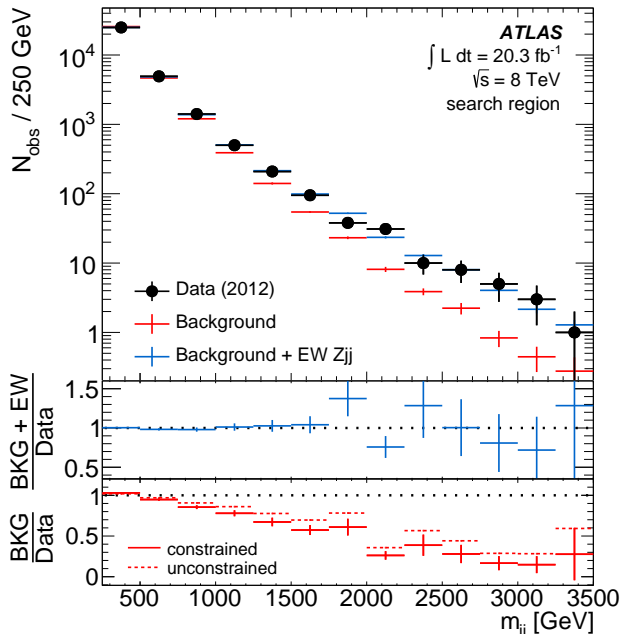


FIG. 28. Invariant-mass distribution of the two leading jets in  $Zjj$  production. The label “EW” denotes the VBF production mechanism, and “BKG” all other ones. Figure taken from Ref. [226].

58% (44% expected) on the invisible branching fraction at 95% CL [225].

In the following we will focus on the production of electroweak gauge bosons. VBF-production of a single  $Z$  boson in association with two jets has been studied by ATLAS [226] and CMS [227, 228]. The final-state signature of two opposite-sign, same-flavor leptons plus two jets is dominated by the QCD-induced process. As VBF-specific cut, a lower bound on the invariant mass of the two leading jets of 250 GeV has been imposed. With this, the predicted fraction of VBF-induced events is still only 4.0%, while 94.7% are QCD-induced, and the rest originates from semi-leptonic diboson production. Raising this bound to 1 TeV increases the VBF fraction to 12% only. Therefore, a shape analysis has been employed in Ref. [226]. The obtained invariant-mass distribution of the two leading jets is depicted in Fig. 28, where the label “EW” refers to the prediction of the VBF production process and “BKG” to the rest, which is dominated by QCD-induced production. One clearly sees the typical VBF behavior, which predicts comparably more cross section in the very high-mass region and becomes the dominant source of events. The two lower panels of the figure show the ratio of the theory prediction to the data<sup>2</sup>. One already sees by eye that the background-only hypothesis does not reproduce the measured data, while there is good agreement when including the electroweak production process. A statistical analysis shows that the significance exceeds the observation level of five standard deviations, thus marking the first observation of a vector-boson fusion process. More recently, also VBF- $W$  production has been studied by CMS [229] and a first measurement of the cross section performed, which agrees well with the SM expectation.

Moving on to vector-boson scattering, production of two leptonically decaying same-sign  $W$  bosons plus two jets has been studied both by ATLAS [221] and CMS [230]. This final

<sup>2</sup> The two labels in the lower panel refer to the background template fit.

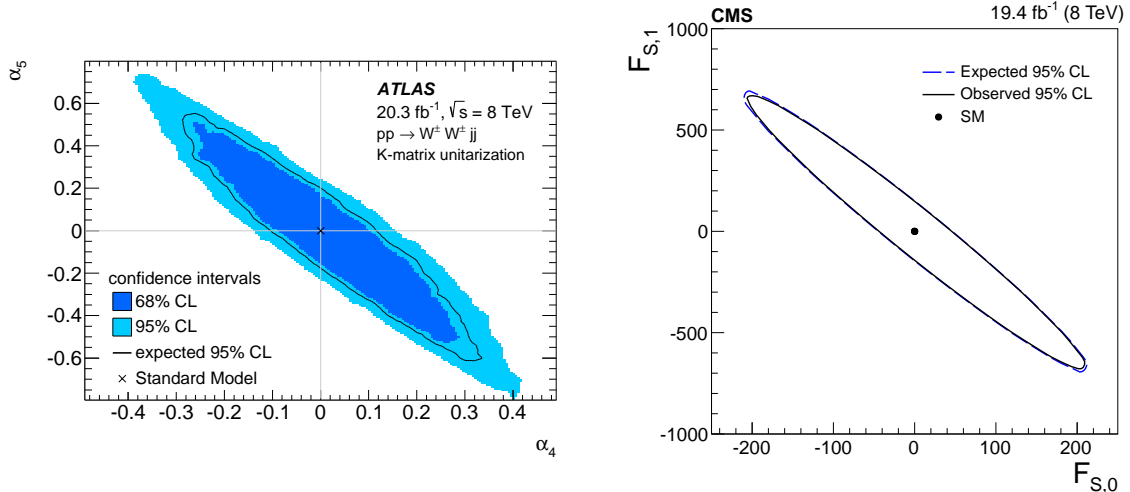


FIG. 29. Limits on anomalous quartic gauge-boson vertices determined from same-sign  $WW$  production plus two jets. *Left*: ATLAS result using the operator set of the chiral Lagrangian, eq. (81), and  $K$ -matrix unitarization. Figure taken from Ref. [221]. *Right*: CMS result for the dimension-8 operators of eq. (74), using capital letters for the coefficients, setting  $\Lambda = 1$  TeV and not applying any unitarization procedure. Figure taken from Ref. [230]. The relation between the two operator sets is given by eq. (104).

state is advantageous, as the corresponding QCD-induced process cannot be produced from initial-state gluons at leading order. Thus the fraction of electroweak events is larger than for other boson combinations. Positive evidence (3.6 standard deviations) for electroweak  $W^+W^+jj$  production is reported by ATLAS, while CMS observes a 1.9  $\sigma$  excess. Both results are then used to obtain limits on anomalous QGCs, shown in Fig. 29. ATLAS thereby uses the operator set of the chiral Lagrangian, eq. (81), and applies  $K$ -matrix unitarization, whereas CMS extracts limits on the operators  $\mathcal{O}_{S,0}$  and  $\mathcal{O}_{S,1}$ , eq. (74), and does not apply any unitarization procedure. The relation between the two sets of operators is given by the  $WWWW$ -vertex entry of eq. (104). As an example, the parameter point  $F_{S,0} = 200$  TeV<sup>-4</sup>,  $F_{S,1} = -600$  TeV<sup>-4</sup>, located towards the lower right end of the CMS 95% CL region, translates into  $\alpha_4 \simeq 0.092$ ,  $\alpha_5 \simeq -0.184$ . This is well inside the 68% CL region of the ATLAS plot, despite observing the process with greater significance. The difference is due to the lack of unitarization method in the CMS result, so large event counts are predicted at high invariant masses, which are not present in the data and therefore lead to stronger limits. The limits, up to which the results respect the unitarity bound without the need for a specific unitarization method, are given as  $F_{S,0} = 0.016$  TeV<sup>-4</sup> and  $F_{S,1} = 0.050$  TeV<sup>-4</sup>, when the other coefficient is set to zero [230].

Other vector-boson scattering processes studied so far are  $WZjj$  production [231] and semi-leptonic  $WVjj$  production [232] in ATLAS, and  $W\gamma jj$  production [233] and  $Z\gamma jj$  production [234] in CMS. Evidence for electroweak production has been found in the last process.

## B. Future Prospects

Both experiments have also studied expectations on vector-boson scattering and limits on anomalous QGCs from future running of the LHC [235–237]. These have been performed for a center-of-mass energy of 14 TeV and integrated luminosities of up to  $3000 \text{ fb}^{-1}$ . The actual LHC run-II center-of-mass energy of 13 TeV is slightly lower, but these are not expected to change the general picture.

All VBF processes greatly benefit from the higher center-of-mass energy. As we have seen in Tables (I, II), the cross section increases by about a factor 3 to 4 when going from 8 to 13 TeV. Then not only the same-sign  $W$  channel can be observed, but also the other combinations of massive bosons,  $W^+W^-$ ,  $WZ$  and  $ZZ$  [235–237]. Given no relevant deviation from the SM prediction is observed, the various dimension-8 operators are expected to be constrained to values below 0.2 to 1  $\text{TeV}^{-4}$  at 95% CL. Deviations from operators with a size of several  $\text{TeV}^{-4}$  can even lead to a discovery when  $3000 \text{ fb}^{-1}$  of luminosity have been collected [235–237].

## VII. SUMMARY

Vector-boson fusion and vector-boson scattering are important production processes at the LHC. From the theoretical side, they are characterized by quark–(anti-)quark scattering through  $t$ -channel exchange of an electroweak gauge boson. As there is no color connection between the two quark lines, a very characteristic feature emerges. The two final-state quarks appear as so-called tagging jets in the forward region of the detectors. Additional jet radiation in the region between the two tagging jets is strongly suppressed. This distinguishes them from the QCD-induced production mode of the same final state, which shows enhanced jet activity in the central region. We have also discussed the impact of interference effects between the two. These become negligible when imposing VBF cuts, which require a large invariant mass and rapidity separation of the two tagging jets.

Higher-order corrections play an important role to provide accurate predictions. The size of the NLO QCD corrections for VBF processes is moderate, but they help to stabilize the predictions under variations of the renormalization and factorization scales. For these, taking the momentum transfer of the exchanged bosons proves to be an advantageous choice. We have derived explicit expressions for the vertex corrections. These are both UV-divergent, which is cured by renormalization, and IR-divergent, which is solved by adding diagrams with real emission of a gluon. Corrections beyond NLO QCD are available for VBF-Higgs production only. Both NLO EW and NNLO QCD contributions lead to a reduction of the cross section. In the latter case the change is outside the uncertainty bands given by a scale variation of the NLO QCD cross section.

Recent theoretical progress has been the matching of NLO QCD calculations with parton showers. We have first given an overview of the general properties, before discussing issues specific to VBF processes. The distribution of jets in the central region has been an open question from the combination of LO cross sections and parton showers, as predictions of various programs have differed significantly. Using NLO QCD results, this has now stabilized and a rather low jet activity is expected, making this observable a good tool to distinguish VBF from background processes. We have also discussed the impact of using different matching schemes and showers, which agree well with each other.

The appearance of triple and quartic gauge couplings makes VBF processes an important

tool to measure these couplings and probe possible deviations from the SM prediction. They are conveniently parametrized using effective field theories. We have given an overview of the most common operator schemes used and presented the relations among them. When their coefficients become large, unitarity of the  $S$  matrix can be violated. Through partial-wave expansion we have derived the relevant bound on scattering amplitudes. Unitarity can be restored for example through the use of form factors or an inverse stereographic projection back onto the unitarity circle, the  $K$ -matrix method. For the latter we have presented explicit expressions using the scalar dimension-8 operators.

First evidence for some VBF production processes has already been gathered during the run-I phase of the LHC. As no relevant deviations from the SM prediction have been observed, this also allows to place constraints on the anomalous coupling contributions. The higher center-of-mass energy of subsequent LHC runs will strongly benefit the VBF processes. All combinations of electroweak gauge boson pairs will be observable with the final expected luminosity. Stringent constraints can be placed on new-physics contributions to the quartic gauge couplings. A further enhancement of the precision could be reached when increasing the center-of-mass energy. Current proposals with energies up to 100 TeV allow for an ultimate test of the SM.

## ACKNOWLEDGMENTS

It is a pleasure to thank Dieter Zeppenfeld for many valuable discussions, helpful comments on the manuscript as well as his encouragement to write this report. I am grateful to Johannes Bellm, Paco Campanario, Bastian Feigl, Stefan Gieseke, Simon Plätzer and Franziska Schissler for helpful discussions on the topics presented here. I would also like to thank Graeme Nail, Robin Roth and Marco Sekulla for a careful reading of the manuscript.

- 
- [1] G. Aad *et al.* (ATLAS), Phys. Lett. **B716**, 1 (2012), arXiv:1207.7214 [hep-ex].
  - [2] S. Chatrchyan *et al.* (CMS), Phys. Lett. **B716**, 30 (2012), arXiv:1207.7235 [hep-ex].
  - [3] S. Dittmaier *et al.* (LHC Higgs Cross Section Working Group), (2011), 10.5170/CERN-2011-002, arXiv:1101.0593 [hep-ph].
  - [4] S. Dittmaier *et al.*, (2012), 10.5170/CERN-2012-002, arXiv:1201.3084 [hep-ph].
  - [5] J. R. Andersen *et al.* (LHC Higgs Cross Section Working Group), (2013), 10.5170/CERN-2013-004, arXiv:1307.1347 [hep-ph].
  - [6] D. de Florian *et al.* (The LHC Higgs Cross Section Working Group), (2016), arXiv:1610.07922 [hep-ph].
  - [7] S. Catani and M. H. Seymour, Nucl. Phys. **B485**, 291 (1997), [Erratum: Nucl. Phys. **B510**, 503(1998)], arXiv:hep-ph/9605323 [hep-ph].
  - [8] P. Nason, JHEP **11**, 040 (2004), arXiv:hep-ph/0409146 [hep-ph].
  - [9] S. Frixione, P. Nason, and C. Oleari, JHEP **11**, 070 (2007), arXiv:0709.2092 [hep-ph].
  - [10] S. Alioli, P. Nason, C. Oleari, and E. Re, JHEP **06**, 043 (2010), arXiv:1002.2581 [hep-ph].
  - [11] S. Frixione and B. R. Webber, JHEP **06**, 029 (2002), arXiv:hep-ph/0204244 [hep-ph].
  - [12] W. Heitler and H. W. Peng, Mathematical Proceedings of the Cambridge Philosophical Society **38**, 296 (1942).



- [13] W. Heitler, in *Proceedings, International Conference on Fundamental Particles and Low Temperatures, vol.1, Cambridge, UK, 22-27 Jul 1946* (1947) pp. 189–194.
- [14] R. N. Cahn and S. Dawson, *Phys. Lett.* **B136**, 196 (1984), [Erratum: *Phys. Lett.*B138,464(1984)].
- [15] S. Dawson, *Nucl. Phys.* **B249**, 42 (1985).
- [16] M. J. Duncan, G. L. Kane, and W. W. Repko, *Nucl. Phys.* **B272**, 517 (1986).
- [17] J. M. Butterworth, B. E. Cox, and J. R. Forshaw, *Phys. Rev.* **D65**, 096014 (2002), arXiv:hep-ph/0201098 [hep-ph].
- [18] R. N. Cahn, S. D. Ellis, R. Kleiss, and W. J. Stirling, *Phys. Rev.* **D35**, 1626 (1987).
- [19] R. Kleiss and W. J. Stirling, *Phys. Lett.* **B200**, 193 (1988).
- [20] V. D. Barger, T. Han, and R. J. N. Phillips, *Phys. Rev.* **D37**, 2005 (1988).
- [21] D. Zeppenfeld, in *Neutrinos in physics and astrophysics from 10<sup>\*\*(-33)</sup> to 10<sup>\*\*28</sup> CM. Proceedings, Conference, TASI'98, Boulder, USA, June 1-26, 1998* (1999) pp. 303–350, arXiv:hep-ph/9902307 [hep-ph].
- [22] T. Plehn, *Lect. Notes Phys.* **844**, 1 (2012), arXiv:0910.4182 [hep-ph].
- [23] D. A. Dicus and S. S. D. Willenbrock, *Phys. Rev.* **D32**, 1642 (1985).
- [24] G. Altarelli, B. Mele, and F. Pitolli, *Nucl. Phys.* **B287**, 205 (1987).
- [25] W. Kilian, M. Kramer, and P. M. Zerwas, *Phys. Lett.* **B373**, 135 (1996), arXiv:hep-ph/9512355 [hep-ph].
- [26] A. Djouadi, *Phys. Rept.* **457**, 1 (2008), arXiv:hep-ph/0503172 [hep-ph].
- [27] K. Arnold *et al.*, *Comput. Phys. Commun.* **180**, 1661 (2009), arXiv:0811.4559 [hep-ph].
- [28] J. Baglio *et al.*, (2014), arXiv:1404.3940 [hep-ph].
- [29] J. Baglio, J. Bellm, G. Bozzi, M. Brieg, F. Campanario, C. Englert, B. Feigl, J. Frank, T. Figy, F. Geyer, C. Hackstein, V. Hankele, B. Jäger, M. Kerner, M. Kubocz, M. Löschner, L. D. Ninh, C. Oleari, S. Palmer, S. Plätzer, M. Rauch, R. Roth, H. Rzehak, F. Schissler, O. Schlimpert, M. Spannowsky, M. Worek, and D. Zeppenfeld, “VBFNLO - a parton level Monte Carlo for processes with electroweak bosons,” <https://www.itp.kit.edu/vbfnlo> (2016).
- [30] D. L. Rainwater, R. Szalapski, and D. Zeppenfeld, *Phys. Rev.* **D54**, 6680 (1996), arXiv:hep-ph/9605444 [hep-ph].
- [31] F. Schissler, *Parton Shower Corrections to Vector-Boson Fusion Processes at the Large Hadron Collider in Next-to-Leading Order QCD Precision*, Ph.D. thesis, KIT, Karlsruhe (2014).
- [32] T. Melia, K. Melnikov, R. Rontsch, and G. Zanderighi, *JHEP* **12**, 053 (2010), arXiv:1007.5313 [hep-ph].
- [33] T. Melia, K. Melnikov, R. Rontsch, and G. Zanderighi, *Phys. Rev.* **D83**, 114043 (2011), arXiv:1104.2327 [hep-ph].
- [34] T. Melia, P. Nason, R. Rontsch, and G. Zanderighi, *Eur. Phys. J.* **C71**, 1670 (2011), arXiv:1102.4846 [hep-ph].
- [35] B. Jager and G. Zanderighi, *JHEP* **11**, 055 (2011), arXiv:1108.0864 [hep-ph].
- [36] N. Greiner, G. Heinrich, P. Mastrolia, G. Ossola, T. Reiter, and F. Tramontano, *Phys. Lett.* **B713**, 277 (2012), arXiv:1202.6004 [hep-ph].
- [37] F. Campanario, M. Kerner, L. D. Ninh, and D. Zeppenfeld, *Phys. Rev. Lett.* **111**, 052003 (2013), arXiv:1305.1623 [hep-ph].
- [38] T. Gehrmann, N. Greiner, and G. Heinrich, *Phys. Rev. Lett.* **111**, 222002 (2013), arXiv:1308.3660 [hep-ph].

- [39] F. Campanario, M. Kerner, L. D. Ninh, and D. Zeppenfeld, Phys. Rev. **D89**, 054009 (2014), arXiv:1311.6738 [hep-ph].
- [40] S. Badger, A. Guffanti, and V. Yundin, JHEP **03**, 122 (2014), arXiv:1312.5927 [hep-ph].
- [41] F. Campanario, M. Kerner, L. D. Ninh, and D. Zeppenfeld, Eur. Phys. J. **C74**, 2882 (2014), arXiv:1402.0505 [hep-ph].
- [42] Z. Bern, L. J. Dixon, F. Febres Cordero, S. Hoeche, H. Ita, D. A. Kosower, N. A. Lo Presti, and D. Maitre, Phys. Rev. **D90**, 054004 (2014), arXiv:1402.4127 [hep-ph].
- [43] J. Alwall, R. Frederix, S. Frixione, V. Hirschi, F. Maltoni, O. Mattelaer, H. S. Shao, T. Stelzer, P. Torrielli, and M. Zaro, JHEP **07**, 079 (2014), arXiv:1405.0301 [hep-ph].
- [44] F. Campanario, M. Kerner, L. D. Ninh, and D. Zeppenfeld, JHEP **07**, 148 (2014), arXiv:1405.3972 [hep-ph].
- [45] F. Campanario, M. Kerner, L. D. Ninh, and D. Zeppenfeld, Eur. Phys. J. **C74**, 3085 (2014), arXiv:1407.7857 [hep-ph].
- [46] F. Campanario, M. Kerner, L. D. Ninh, M. Rauch, R. Roth, and D. Zeppenfeld, *Proceedings, Advances in Computational Particle Physics: Final Meeting (SFB-TR-9): Durbach, Germany, September 15-19, 2014*, Nucl. Part. Phys. Proc. **261-262**, 268 (2015).
- [47] A. Denner, L. Hosekova, and S. Kallweit, Phys. Rev. **D86**, 114014 (2012), arXiv:1209.2389 [hep-ph].
- [48] T. Han, G. Valencia, and S. Willenbrock, Phys. Rev. Lett. **69**, 3274 (1992), arXiv:hep-ph/9206246 [hep-ph].
- [49] T. Figy, C. Oleari, and D. Zeppenfeld, Phys. Rev. **D68**, 073005 (2003), arXiv:hep-ph/0306109 [hep-ph].
- [50] C. Oleari and D. Zeppenfeld, Phys. Rev. **D69**, 093004 (2004), arXiv:hep-ph/0310156 [hep-ph].
- [51] B. Jager, C. Oleari, and D. Zeppenfeld, JHEP **07**, 015 (2006), arXiv:hep-ph/0603177 [hep-ph].
- [52] B. Jager, C. Oleari, and D. Zeppenfeld, Phys. Rev. **D73**, 113006 (2006), arXiv:hep-ph/0604200 [hep-ph].
- [53] G. Bozzi, B. Jager, C. Oleari, and D. Zeppenfeld, Phys. Rev. **D75**, 073004 (2007), arXiv:hep-ph/0701105 [hep-ph].
- [54] B. Jager, C. Oleari, and D. Zeppenfeld, Phys. Rev. **D80**, 034022 (2009), arXiv:0907.0580 [hep-ph].
- [55] F. Campanario, N. Kaiser, and D. Zeppenfeld, Phys. Rev. **D89**, 014009 (2014), arXiv:1309.7259 [hep-ph].
- [56] T. Hahn, Comput. Phys. Commun. **140**, 418 (2001), arXiv:hep-ph/0012260 [hep-ph].
- [57] T. Hahn and M. Perez-Victoria, Comput. Phys. Commun. **118**, 153 (1999), arXiv:hep-ph/9807565 [hep-ph].
- [58] T. Hahn, *Application of quantum field theory to phenomenology. Loops and legs in quantum field theory. Proceedings, 6th International Symposium, RADCOR 2002, and 6th Zeuthen Workshop, Staffelsee, Germany, September 8-13, 2002*, Nucl. Phys. Proc. Suppl. **116**, 363 (2003), [,363(2002)], arXiv:hep-ph/0210220 [hep-ph].
- [59] T. Hahn, *Loops and legs in quantum field theory. Proceedings, 7th Workshop on Elementary Particle Theory, Zinnowitz, Germany, April 25-30, 2004*, Nucl. Phys. Proc. Suppl. **135**, 333 (2004), [,333(2004)], arXiv:hep-ph/0406288 [hep-ph].
- [60] T. Hahn, *2005 International Linear Collider Workshop : LCWS 2005 : Stanford, California, USA, 18-22 March, 2005*, eConf **C050318**, 0604 (2005), arXiv:hep-ph/0506201 [hep-ph].

- [61] T. Hahn and M. Rauch, *Application of quantum field theory to phenomenology – Radcor 2005, proceedings of the 7th International Symposium on Radiative Corrections, Sokendai, Shonan-Village, Kanagawa, Japan, 2-7 October 2005*, Nucl. Phys. Proc. Suppl. **157**, 236 (2006), [,236(2006)], arXiv:hep-ph/0601248 [hep-ph].
- [62] T. Hahn and J. I. Illana, *Proceedings, 8th DESY Workshop on Elementary Particle Theory: Loops and Legs in Quantum Field Theory: Eisenach, Germany, 23-28 April 2006*, Nucl. Phys. Proc. Suppl. **160**, 101 (2006), [,101(2006)], arXiv:hep-ph/0607049 [hep-ph].
- [63] T. Hahn, Comput. Phys. Commun. **178**, 217 (2008), arXiv:hep-ph/0611273 [hep-ph].
- [64] G. J. van Oldenborgh and J. A. M. Vermaseren, Z. Phys. **C46**, 425 (1990).
- [65] G. Passarino and M. J. G. Veltman, Nucl. Phys. **B160**, 151 (1979).
- [66] A. Denner, Fortsch. Phys. **41**, 307 (1993), arXiv:0709.1075 [hep-ph].
- [67] T. Binoth *et al.*, *Physics at TeV colliders. Proceedings, 6th Workshop, dedicated to Thomas Binoth, Les Houches, France, June 8-26, 2009*, Comput. Phys. Commun. **181**, 1612 (2010), [,1(2010)], arXiv:1001.1307 [hep-ph].
- [68] S. Alioli *et al.*, Comput. Phys. Commun. **185**, 560 (2014), arXiv:1308.3462 [hep-ph].
- [69] T. Kinoshita, J. Math. Phys. **3**, 650 (1962).
- [70] T. D. Lee and M. Nauenberg, Phys. Rev. **133**, B1549 (1964), [,25(1964)].
- [71] S. Frixione, Z. Kunszt, and A. Signer, Nucl. Phys. **B467**, 399 (1996), arXiv:hep-ph/9512328 [hep-ph].
- [72] Y. L. Dokshitzer, Sov. Phys. JETP **46**, 641 (1977), [Zh. Eksp. Teor. Fiz.73,1216(1977)].
- [73] V. N. Gribov and L. N. Lipatov, Sov. J. Nucl. Phys. **15**, 438 (1972), [Yad. Fiz.15,781(1972)].
- [74] G. Altarelli and G. Parisi, Nucl. Phys. **B126**, 298 (1977).
- [75] K. Arnold *et al.*, (2011), arXiv:1107.4038 [hep-ph].
- [76] K. Arnold *et al.*, (2012), arXiv:1207.4975 [hep-ph].
- [77] K. A. Olive *et al.* (Particle Data Group), Chin. Phys. **C38**, 090001 (2014).
- [78] S. Catani, Y. L. Dokshitzer, M. H. Seymour, and B. R. Webber, Nucl. Phys. **B406**, 187 (1993).
- [79] S. D. Ellis and D. E. Soper, Phys. Rev. **D48**, 3160 (1993), arXiv:hep-ph/9305266 [hep-ph].
- [80] S. Frixione, Phys. Lett. **B429**, 369 (1998), arXiv:hep-ph/9801442 [hep-ph].
- [81] A. D. Martin, R. G. Roberts, W. J. Stirling, and R. S. Thorne, Eur. Phys. J. **C39**, 155 (2005), arXiv:hep-ph/0411040 [hep-ph].
- [82] R. D. Ball, V. Bertone, S. Carrazza, L. Del Debbio, S. Forte, A. Guffanti, N. P. Hartland, and J. Rojo (NNPDF), Nucl. Phys. **B877**, 290 (2013), arXiv:1308.0598 [hep-ph].
- [83] C. Schmidt, J. Pumplin, D. Stump, and C. P. Yuan, Phys. Rev. **D93**, 114015 (2016), arXiv:1509.02905 [hep-ph].
- [84] S. Dulat, T.-J. Hou, J. Gao, M. Guzzi, J. Huston, P. Nadolsky, J. Pumplin, C. Schmidt, D. Stump, and C. P. Yuan, Phys. Rev. **D93**, 033006 (2016), arXiv:1506.07443 [hep-ph].
- [85] A. Buckley, J. Ferrando, S. Lloyd, K. Nordström, B. Page, M. Rüfenacht, M. Schönherr, and G. Watt, Eur. Phys. J. **C75**, 132 (2015), arXiv:1412.7420 [hep-ph].
- [86] J. Butterworth *et al.*, J. Phys. **G43**, 023001 (2016), arXiv:1510.03865 [hep-ph].
- [87] G. Watt and R. S. Thorne, JHEP **08**, 052 (2012), arXiv:1205.4024 [hep-ph].
- [88] J. Gao and P. Nadolsky, JHEP **07**, 035 (2014), arXiv:1401.0013 [hep-ph].
- [89] S. Carrazza, S. Forte, Z. Kassabov, J. I. Latorre, and J. Rojo, Eur. Phys. J. **C75**, 369 (2015), arXiv:1505.06736 [hep-ph].
- [90] L. A. Harland-Lang, A. D. Martin, P. Motylinski, and R. S. Thorne, Eur. Phys. J. **C75**, 204 (2015), arXiv:1412.3989 [hep-ph].

- [91] R. D. Ball *et al.* (NNPDF), JHEP **04**, 040 (2015), arXiv:1410.8849 [hep-ph].
- [92] M. Ciccolini, A. Denner, and S. Dittmaier, Phys. Rev. Lett. **99**, 161803 (2007), arXiv:0707.0381 [hep-ph].
- [93] M. Ciccolini, A. Denner, and S. Dittmaier, Phys. Rev. **D77**, 013002 (2008), arXiv:0710.4749 [hep-ph].
- [94] T. Figy, S. Palmer, and G. Weiglein, JHEP **02**, 105 (2012), arXiv:1012.4789 [hep-ph].
- [95] A. Denner, S. Dittmaier, S. Kallweit, and A. Muck, “HAWK: Higgs Attached to Weak bosons,” <http://omnibus.uni-freiburg.de/~sd565/programs/hawk/hawk.html> (2010–2016).
- [96] P. Bolzoni, F. Maltoni, S.-O. Moch, and M. Zaro, Phys. Rev. Lett. **105**, 011801 (2010), arXiv:1003.4451 [hep-ph].
- [97] P. Bolzoni, F. Maltoni, S.-O. Moch, and M. Zaro, Phys. Rev. **D85**, 035002 (2012), arXiv:1109.3717 [hep-ph].
- [98] F. A. Dreyer and A. Karlberg, Phys. Rev. Lett. **117**, 072001 (2016), arXiv:1606.00840 [hep-ph].
- [99] A. Karlberg, *At the Frontier of Precision QCD in the LHC Era*, Ph.D. thesis (2016), arXiv:1610.06226 [hep-ph].
- [100] M. Cacciari, F. A. Dreyer, A. Karlberg, G. P. Salam, and G. Zanderighi, Phys. Rev. Lett. **115**, 082002 (2015), arXiv:1506.02660 [hep-ph].
- [101] T. Figy, V. Hankele, and D. Zeppenfeld, JHEP **02**, 076 (2008), arXiv:0710.5621 [hep-ph].
- [102] B. Jäger, F. Schissler, and D. Zeppenfeld, JHEP **07**, 125 (2014), arXiv:1405.6950 [hep-ph].
- [103] F. Campanario, T. M. Figy, S. Plätzer, and M. Sjödal, Phys. Rev. Lett. **111**, 211802 (2013), arXiv:1308.2932 [hep-ph].
- [104] P. Nason and C. Oleari, JHEP **02**, 037 (2010), arXiv:0911.5299 [hep-ph].
- [105] P. Z. Skands, Phys. Rev. **D82**, 074018 (2010), arXiv:1005.3457 [hep-ph].
- [106] M. Bahr *et al.*, Eur. Phys. J. **C58**, 639 (2008), arXiv:0803.0883 [hep-ph].
- [107] J. Bellm *et al.*, Eur. Phys. J. **C76**, 196 (2016), arXiv:1512.01178 [hep-ph].
- [108] G. Corcella, I. G. Knowles, G. Marchesini, S. Moretti, K. Odagiri, P. Richardson, M. H. Seymour, and B. R. Webber, JHEP **01**, 010 (2001), arXiv:hep-ph/0011363 [hep-ph].
- [109] G. Corcella, I. G. Knowles, G. Marchesini, S. Moretti, K. Odagiri, P. Richardson, M. H. Seymour, and B. R. Webber, (2002), arXiv:hep-ph/0210213 [hep-ph].
- [110] J. Bellm *et al.*, (2013), arXiv:1310.6877 [hep-ph].
- [111] T. Sjostrand, S. Mrenna, and P. Z. Skands, Comput. Phys. Commun. **178**, 852 (2008), arXiv:0710.3820 [hep-ph].
- [112] T. Sjostrand, S. Mrenna, and P. Z. Skands, JHEP **05**, 026 (2006), arXiv:hep-ph/0603175 [hep-ph].
- [113] T. Gleisberg, S. Hoeche, F. Krauss, M. Schonherr, S. Schumann, F. Siegert, and J. Winter, JHEP **02**, 007 (2009), arXiv:0811.4622 [hep-ph].
- [114] R. K. Ellis, W. J. Stirling, and B. R. Webber, Camb. Monogr. Part. Phys. Nucl. Phys. Cosmol. **8**, 1 (1996).
- [115] G. P. Salam, *2008 CTEQ-MCnet Summer School on QCD Phenomenology and Monte Carlo Event Generators (MCnet 08) (CTEQ 08) Debrecen, Hungary, August 8-16, 2008*, Eur. Phys. J. **C67**, 637 (2010), arXiv:0906.1833 [hep-ph].
- [116] A. Buckley *et al.*, Phys. Rept. **504**, 145 (2011), arXiv:1101.2599 [hep-ph].
- [117] S. Gieseke, Prog. Part. Nucl. Phys. **72**, 155 (2013).
- [118] R. Frederix, S. Frixione, V. Hirschi, F. Maltoni, R. Pittau, and P. Torrielli, JHEP **02**, 099

- (2012), arXiv:1110.4738 [hep-ph].
- [119] W. T. Giele, D. A. Kosower, and P. Z. Skands, *Phys. Rev.* **D78**, 014026 (2008), arXiv:0707.3652 [hep-ph].
  - [120] S. Hoche, F. Krauss, M. Schonherr, and F. Siegert, *JHEP* **04**, 024 (2011), arXiv:1008.5399 [hep-ph].
  - [121] S. Hoche, F. Krauss, M. Schonherr, and F. Siegert, *JHEP* **08**, 123 (2011), arXiv:1009.1127 [hep-ph].
  - [122] S. Platzer and S. Gieseke, *Eur. Phys. J.* **C72**, 2187 (2012), arXiv:1109.6256 [hep-ph].
  - [123] S. Höche, F. Krauss, M. Schönerr, and F. Siegert, *Phys. Rev. Lett.* **110**, 052001 (2013), arXiv:1201.5882 [hep-ph].
  - [124] M. Ritzmann, D. A. Kosower, and P. Skands, *Phys. Lett.* **B718**, 1345 (2013), arXiv:1210.6345 [hep-ph].
  - [125] Y. L. Dokshitzer, V. A. Khoze, and S. I. Troian, in *6th Physics in Collision Chicago, Illinois, September 3-5, 1986* (1986) pp. 417–448.
  - [126] J. D. Bjorken, *Phys. Rev.* **D47**, 101 (1993).
  - [127] V. D. Barger, R. J. N. Phillips, and D. Zeppenfeld, *Phys. Lett.* **B346**, 106 (1995), arXiv:hep-ph/9412276 [hep-ph].
  - [128] V. A. Khoze, M. G. Ryskin, W. J. Stirling, and P. H. Williams, *Eur. Phys. J.* **C26**, 429 (2003), arXiv:hep-ph/0207365 [hep-ph].
  - [129] G. Cullen, N. Greiner, G. Heinrich, G. Luisoni, P. Mastrolia, G. Ossola, T. Reiter, and F. Tramontano, *Eur. Phys. J.* **C72**, 1889 (2012), arXiv:1111.2034 [hep-ph].
  - [130] G. Cullen *et al.*, *Eur. Phys. J.* **C74**, 3001 (2014), arXiv:1404.7096 [hep-ph].
  - [131] E. Boos *et al.*, in *Physics at TeV colliders. Proceedings, Euro Summer School, Les Houches, France, May 21-June 1, 2001* (2001) arXiv:hep-ph/0109068 [hep-ph].
  - [132] J. Alwall *et al.*, *Monte Carlos for the LHC: A Workshop on the Tools for LHC Event Simulation (MC4LHC) Geneva, Switzerland, July 17-16, 2006*, *Comput. Phys. Commun.* **176**, 300 (2007), arXiv:hep-ph/0609017 [hep-ph].
  - [133] F. Schissler and D. Zeppenfeld, *JHEP* **04**, 057 (2013), arXiv:1302.2884.
  - [134] B. Jager, S. Schneider, and G. Zanderighi, *JHEP* **09**, 083 (2012), arXiv:1207.2626 [hep-ph].
  - [135] B. Jager and G. Zanderighi, *JHEP* **04**, 024 (2013), arXiv:1301.1695 [hep-ph].
  - [136] B. Jäger, A. Karlberg, and G. Zanderighi, *JHEP* **03**, 141 (2014), arXiv:1312.3252 [hep-ph].
  - [137] S. D. Ellis, Z. Kunszt, and D. E. Soper, *Phys. Rev. Lett.* **69**, 3615 (1992), arXiv:hep-ph/9208249 [hep-ph].
  - [138] G. Aad *et al.* (ATLAS), *Phys. Rev.* **D83**, 052003 (2011), arXiv:1101.0070 [hep-ex].
  - [139] S. Frixione, P. Torrielli, and M. Zaro, *Phys. Lett.* **B726**, 273 (2013), arXiv:1304.7927 [hep-ph].
  - [140] M. Rauch and S. Plätzer, (2016), arXiv:1605.07851 [hep-ph].
  - [141] S. Weinberg, *Phys. Rev. Lett.* **43**, 1566 (1979).
  - [142] W. Buchmuller and D. Wyler, *Nucl. Phys.* **B268**, 621 (1986).
  - [143] K. Hagiwara, R. Szalapski, and D. Zeppenfeld, *Phys. Lett.* **B318**, 155 (1993), arXiv:hep-ph/9308347 [hep-ph].
  - [144] K. Hagiwara, S. Ishihara, R. Szalapski, and D. Zeppenfeld, *Phys. Rev.* **D48**, 2182 (1993).
  - [145] B. Grzadkowski, M. Iskrzynski, M. Misiak, and J. Rosiek, *JHEP* **10**, 085 (2010), arXiv:1008.4884 [hep-ph].
  - [146] C. Degrande, O. Eboli, B. Feigl, B. Jäger, W. Kilian, O. Mattelaer, M. Rauch, J. Reuter, M. Sekulla, and D. Wackerroth, in *Proceedings, Community Summer Study 2013: Snow-*

- mass on the Mississippi (CSS2013): Minneapolis, MN, USA, July 29-August 6, 2013* (2013) arXiv:1309.7890 [hep-ph].
- [147] C. Arzt, M. B. Einhorn, and J. Wudka, Nucl. Phys. **B433**, 41 (1995), arXiv:hep-ph/9405214 [hep-ph].
- [148] O. J. P. Eboli, M. C. Gonzalez-Garcia, and J. K. Mizukoshi, Phys. Rev. **D74**, 073005 (2006), arXiv:hep-ph/0606118 [hep-ph].
- [149] O. J. P. Éboli and M. C. Gonzalez–Garcia, Phys. Rev. **D93**, 093013 (2016), arXiv:1604.03555 [hep-ph].
- [150] M. Sekulla, *Anomalous couplings, resonances and unitarity in vector boson scattering*, Ph.D. thesis, Univ. Siegen (2015).
- [151] M. Löschner, *Unitarisation of Anomalous Couplings in Vector Boson Scattering*, Master’s thesis, KIT, Karlsruhe (2014).
- [152] D. Zeppenfeld, “private communication.”
- [153] S. Weinberg, Physica **A96**, 327 (1979).
- [154] R. Urech, Nucl. Phys. **B433**, 234 (1995), arXiv:hep-ph/9405341 [hep-ph].
- [155] M. Knecht, H. Neufeld, H. Rupertsberger, and P. Talavera, Eur. Phys. J. **C12**, 469 (2000), arXiv:hep-ph/9909284 [hep-ph].
- [156] A. Nyffeler and A. Schenk, Phys. Rev. **D62**, 113006 (2000), arXiv:hep-ph/9907294 [hep-ph].
- [157] J. Hirn and J. Stern, Eur. Phys. J. **C34**, 447 (2004), arXiv:hep-ph/0401032 [hep-ph].
- [158] J. Hirn and J. Stern, Phys. Rev. **D73**, 056001 (2006), arXiv:hep-ph/0504277 [hep-ph].
- [159] G. Buchalla, O. Catá, and C. Krause, Phys. Lett. **B731**, 80 (2014), arXiv:1312.5624 [hep-ph].
- [160] T. Appelquist and C. W. Bernard, Phys. Rev. **D22**, 200 (1980).
- [161] A. C. Longhitano, Phys. Rev. **D22**, 1166 (1980).
- [162] A. C. Longhitano, Nucl. Phys. **B188**, 118 (1981).
- [163] S. Dawson and G. Valencia, Nucl. Phys. **B352**, 27 (1991).
- [164] T. Appelquist and G.-H. Wu, Phys. Rev. **D48**, 3235 (1993), arXiv:hep-ph/9304240 [hep-ph].
- [165] A. Dobado, M. J. Herrero, J. R. Pelaez, E. Ruiz Morales, and M. T. Urdiales, Phys. Lett. **B352**, 400 (1995), arXiv:hep-ph/9502309 [hep-ph].
- [166] A. Dobado and M. T. Urdiales, Z. Phys. **C71**, 659 (1996), arXiv:hep-ph/9502255 [hep-ph].
- [167] A. Dobado, A. Gomez-Nicola, A. L. Maroto, and J. R. Pelaez, *Effective lagrangians for the standard model* (1997).
- [168] W. Kilian, *New York, USA: Springer (2003) 113 p, (Springer tracts in modern physics. 198)*, Springer Tracts Mod. Phys. **198**, 1 (2003).
- [169] A. S. Belyaev, O. J. P. Eboli, M. C. Gonzalez-Garcia, J. K. Mizukoshi, S. F. Novaes, and I. Zacharov, Phys. Rev. **D59**, 015022 (1999), arXiv:hep-ph/9805229 [hep-ph].
- [170] G. Buchalla and O. Cata, JHEP **07**, 101 (2012), arXiv:1203.6510 [hep-ph].
- [171] F. Feruglio, *International Conference on Mossbauer Effect Vancouver, British Columbia, Canada, September 1-3, 1993*, Int. J. Mod. Phys. **A8**, 4937 (1993), arXiv:hep-ph/9301281 [hep-ph].
- [172] J. Bagger, V. D. Barger, K.-m. Cheung, J. F. Gunion, T. Han, G. A. Ladinsky, R. Rosenfeld, and C. P. Yuan, Phys. Rev. **D49**, 1246 (1994), arXiv:hep-ph/9306256 [hep-ph].
- [173] V. Koulovassilopoulos and R. S. Chivukula, Phys. Rev. **D50**, 3218 (1994), arXiv:hep-ph/9312317 [hep-ph].
- [174] C. P. Burgess, J. Matias, and M. Pospelov, Int. J. Mod. Phys. **A17**, 1841 (2002), arXiv:hep-ph/9912459 [hep-ph].
- [175] L.-M. Wang and Q. Wang, Chin. Phys. Lett. **25**, 1984 (2008), arXiv:hep-ph/0605104 [hep-ph].

- [176] B. Grinstein and M. Trott, Phys. Rev. **D76**, 073002 (2007), arXiv:0704.1505 [hep-ph].
- [177] R. Alonso, M. B. Gavela, L. Merlo, S. Rigolin, and J. Yepes, Phys. Lett. **B722**, 330 (2013), [Erratum: Phys. Lett.B726,926(2013)], arXiv:1212.3305 [hep-ph].
- [178] G. Buchalla, O. Catà, and C. Krause, Nucl. Phys. **B880**, 552 (2014), [Erratum: Nucl. Phys.B913,475(2016)], arXiv:1307.5017 [hep-ph].
- [179] I. Brivio, T. Corbett, O. J. P. Éboli, M. B. Gavela, J. Gonzalez-Fraile, M. C. Gonzalez-Garcia, L. Merlo, and S. Rigolin, JHEP **03**, 024 (2014), arXiv:1311.1823 [hep-ph].
- [180] A. Alboteanu, W. Kilian, and J. Reuter, JHEP **11**, 010 (2008), arXiv:0806.4145 [hep-ph].
- [181] T. ATLAS and C. Collaborations, (2015).
- [182] W. Kilian, T. Ohl, J. Reuter, and M. Sekulla, Phys. Rev. **D91**, 096007 (2015), arXiv:1408.6207 [hep-ph].
- [183] K. Hagiwara, R. D. Peccei, D. Zeppenfeld, and K. Hikasa, Nucl. Phys. **B282**, 253 (1987).
- [184] J. Wudka, Int. J. Mod. Phys. **A9**, 2301 (1994), arXiv:hep-ph/9406205 [hep-ph].
- [185] C. Amsler *et al.* (Particle Data Group), Phys. Lett. **B667**, 1 (2008).
- [186] W. J. Stirling and A. Werthenbach, Eur. Phys. J. **C14**, 103 (2000), arXiv:hep-ph/9903315 [hep-ph].
- [187] N. D. Christensen and C. Duhr, Comput. Phys. Commun. **180**, 1614 (2009), arXiv:0806.4194 [hep-ph].
- [188] A. Alloul, N. D. Christensen, C. Degrande, C. Duhr, and B. Fuks, Comput. Phys. Commun. **185**, 2250 (2014), arXiv:1310.1921 [hep-ph].
- [189] O. Eboli and M. Gonzalez-Garcia, “Anomalous quartic electroweak gauge-boson interactions,” <https://feynrules.irmp.ucl.ac.be/wiki/AnomalousGaugeCoupling> (2012–2013).
- [190] B. W. Lee, C. Quigg, and H. B. Thacker, Phys. Rev. **D16**, 1519 (1977).
- [191] M. Jacob and G. C. Wick, Annals Phys. **7**, 404 (1959), [Annals Phys.281,774(2000)].
- [192] U. Baur and D. Zeppenfeld, Phys. Lett. **B201**, 383 (1988).
- [193] G. J. Gounaris, J. Layssac, and F. M. Renard, Phys. Lett. **B332**, 146 (1994), arXiv:hep-ph/9311370 [hep-ph].
- [194] G. J. Gounaris, J. Layssac, J. E. Paschalis, and F. M. Renard, Z. Phys. **C66**, 619 (1995), arXiv:hep-ph/9409260 [hep-ph].
- [195] G. J. Gounaris, F. M. Renard, and G. Tsirigoti, Phys. Lett. **B350**, 212 (1995), arXiv:hep-ph/9502376 [hep-ph].
- [196] C. Degrande, N. Greiner, W. Kilian, O. Mattelaer, H. Mebane, T. Stelzer, S. Willenbrock, and C. Zhang, Annals Phys. **335**, 21 (2013), arXiv:1205.4231 [hep-ph].
- [197] T. Corbett, O. J. P. Éboli, and M. C. Gonzalez-Garcia, Phys. Rev. **D91**, 035014 (2015), arXiv:1411.5026 [hep-ph].
- [198] “VBFNLO utility to calculate form factors,” <https://www.itp.kit.edu/vbfnlo/wiki/doku.php?id=download:formfactor> (2013–2016).
- [199] U. Baur and D. Zeppenfeld, Nucl. Phys. **B308**, 127 (1988).
- [200] T. Figy and D. Zeppenfeld, Phys. Lett. **B591**, 297 (2004), arXiv:hep-ph/0403297 [hep-ph].
- [201] V. Hankele, G. Klamke, D. Zeppenfeld, and T. Figy, Phys. Rev. **D74**, 095001 (2006), arXiv:hep-ph/0609075 [hep-ph].
- [202] T. N. Truong, Phys. Rev. Lett. **61**, 2526 (1988).
- [203] T. N. Truong, Phys. Rev. Lett. **67**, 2260 (1991).
- [204] A. Dobado, M. J. Herrero, and T. N. Truong, Phys. Lett. **B235**, 134 (1990).
- [205] A. Dobado and J. R. Pelaez, Phys. Rev. **D56**, 3057 (1997), arXiv:hep-ph/9604416 [hep-ph].

- [206] J. A. Oller, E. Oset, and J. R. Pelaez, Phys. Rev. Lett. **80**, 3452 (1998), arXiv:hep-ph/9803242 [hep-ph].
- [207] A. Dobado, M. J. Herrero, J. R. Pelaez, and E. Ruiz Morales, Phys. Rev. **D62**, 055011 (2000), arXiv:hep-ph/9912224 [hep-ph].
- [208] A. Gomez Nicola and J. R. Pelaez, Phys. Rev. **D65**, 054009 (2002), arXiv:hep-ph/0109056 [hep-ph].
- [209] D. Espriu and F. Mescia, Phys. Rev. **D90**, 015035 (2014), arXiv:1403.7386 [hep-ph].
- [210] T. N. Truong, Phys. Lett. **B258**, 402 (1991).
- [211] H. Padé, Annales scientifiques de l'École Normale Supérieure **9**, 3 (1892).
- [212] J. L. Basdevant, D. Bessis, and J. Zinn-Justin, Nuovo Cim. **A60**, 185 (1969).
- [213] J. L. Basdevant and B. W. Lee, Phys. Lett. **B29**, 437 (1969).
- [214] D. A. Dicus and W. W. Repko, Phys. Rev. **D42**, 3660 (1990).
- [215] J. S. Schwinger, Phys. Rev. **74**, 1439 (1948).
- [216] M. S. Berger and M. S. Chanowitz, Phys. Lett. **B263**, 509 (1991).
- [217] S. N. Gupta, J. M. Johnson, and W. W. Repko, Phys. Rev. **D48**, 2083 (1993), arXiv:hep-ph/9307239 [hep-ph].
- [218] M. S. Chanowitz, Phys. Rept. **320**, 139 (1999), arXiv:hep-ph/9903522 [hep-ph].
- [219] W. Kilian, T. Ohl, J. Reuter, and M. Sekulla, Phys. Rev. **D93**, 036004 (2016), arXiv:1511.00022 [hep-ph].
- [220] A. Ballestrero, D. Buarque Franzosi, L. Oggero, and E. Maina, JHEP **03**, 031 (2012), arXiv:1112.1171 [hep-ph].
- [221] G. Aad *et al.* (ATLAS), Phys. Rev. Lett. **113**, 141803 (2014), arXiv:1405.6241 [hep-ex].
- [222] M. Szleper, (2014), arXiv:1412.8367 [hep-ph].
- [223] D. R. Green, P. Meade, and M.-A. Pleier, (2016), arXiv:1610.07572 [hep-ex].
- [224] O. J. P. Eboli and D. Zeppenfeld, Phys. Lett. **B495**, 147 (2000), arXiv:hep-ph/0009158 [hep-ph].
- [225] S. Chatrchyan *et al.* (CMS), Eur. Phys. J. **C74**, 2980 (2014), arXiv:1404.1344 [hep-ex].
- [226] G. Aad *et al.* (ATLAS), JHEP **04**, 031 (2014), arXiv:1401.7610 [hep-ex].
- [227] S. Chatrchyan *et al.* (CMS), JHEP **10**, 062 (2013), arXiv:1305.7389 [hep-ex].
- [228] V. Khachatryan *et al.* (CMS), Eur. Phys. J. **C75**, 66 (2015), arXiv:1410.3153 [hep-ex].
- [229] V. Khachatryan *et al.* (CMS), Submitted to: JHEP (2016), arXiv:1607.06975 [hep-ex].
- [230] V. Khachatryan *et al.* (CMS), Phys. Rev. Lett. **114**, 051801 (2015), arXiv:1410.6315 [hep-ex].
- [231] G. Aad *et al.* (ATLAS), Phys. Rev. **D93**, 092004 (2016), arXiv:1603.02151 [hep-ex].
- [232] M. Aaboud *et al.* (ATLAS), (2016), arXiv:1609.05122 [hep-ex].
- [233] CMS Collaboration, *A search for electroweak-induced production of  $W\gamma$  with two jets and constraints on anomalous quartic gauge couplings in  $pp$  collisions at  $\sqrt{s} = 8$  TeV*, Tech. Rep. CMS-PAS-SMP-14-011 (CERN, Geneva, 1900).
- [234] CMS Collaboration, *Evidence for the electroweak  $Z$  gamma production in association with two jets and a search for anomalous quartic gauge couplings in  $pp$  collisions at  $\sqrt{s} = 8$  TeV*, Tech. Rep. CMS-PAS-SMP-14-018 (CERN, Geneva, 2015).
- [235] ATLAS Collaboration, *Studies of Vector Boson Scattering with an Upgraded ATLAS Detector at a High-Luminosity LHC*, Tech. Rep. ATL-PHYS-PUB-2012-005 (CERN, Geneva, 2012).
- [236] ATLAS Collaboration, *Studies of Vector Boson Scattering And Triboson Production with an Upgraded ATLAS Detector at a High-Luminosity LHC*, Tech. Rep. ATL-PHYS-PUB-2013-006 (CERN, Geneva, 2013).
- [237] CMS Collaboration, *Vector Boson Scattering and Quartic Gauge Coupling Studies in  $WZ$*



*Production at 14 TeV*, Tech. Rep. CMS-PAS-FTR-13-006 (CERN, Geneva, 2013).